NTNU – Trondheim
Norwegian University of
Science and Technology

The Influence of Constituent Particles on Compression Properties and Fracture Initiation in Al Alloys

Frank Oliver Bakken

Materials Technology
Submission date: June 2013
Supervisor: Knut Marthinsen, IMTE
Co-supervisor: Ida Westermann, SINTEF

Norwegian University of Science and Technology
Department of Materials Science and Engineering

Preface

This is a Master thesis written at Norwegian University of Science and Technology (NTNU) for the Department of Materials Science and Engineering in the spring of 2013. The aim for this work was to get a better understanding of the constituent particles influence on compression properties and fracture initiation in aluminium alloys.

This project is a small part of a much larger project at the CRI (Center for Research-based Innovation) SIMLab (Structural Impact Laboratory) at the Department of Structural Engineering (NTNU), and SINTEF Materials and Chemistry.

I would like to thank my supervisor Prof. Knut Marthinsen and co. supervisor Ida Westermann for constructive feedbacks and helpful guidance through the whole process. I would also like to thank Knut Auestad and Bjørn Holmedal for help with the experimental work, Erlend Nordstrand for help in the metallurgy lab, Julian Tolchard for help with the sample preparations, and Yingda Yu and Wilhelm Dall for the scanning electron microscopy (SEM) training.

This Master thesis has been performed independently, honest, and in accordance with the examination regulations at NTNU.

Trondheim, June 2013

Frank Oliver Bakken

Abstract

In the present work an AlMgSi alloy, with a small amount of Fe has been investigated. The objective was to study how the thermomechanical processing influences the mechanical properties in compression, dependent on grain structure, texture and artificial aging. The materials were subsequent to compression investigated to determine the tendency to pore formation and ductile fracture initiation.

The initial microstructure of the AlMgSi alloy was characterized with respect to grain structure, texture and constituent patricles for three different conditions; i) as-cast condition, ii) extruded condition, and iii) extruded, cold-rolled, and recrystallized condition (including an extruded and cold-rolled condition, which was used only for the characterization of the initial microstructures). The conditions were analyzed with both OM (optical microscopy) and SEM (scanning electron microscopy) before they were artificially aged at 175°C to three different tempers; under-aged temper (2 hours), peak-aged temper (8 hours), and over-aged temper (11 days). Then mechanical properties for the different conditions/tempers were tested in an upsetting test. Finally, the microstructure of compressed conditions in the over-aged temper was characterized with both OM and SEM to look at the microstructural changes due to the deformation introduced during compression.

The characterization of the initial microstructure of the alloy in different conditions proved that the microstructure is strongly dependent on the thermomechanical processing. The upsetting test showed that the ageing time is very influential on the stress-strain behavior. The alloy shows a characteristic stress-strain behavior for each of the three different tempers. The different stress-strain response like the flow stress and work-hardening rate can be explained by the precipitates obtained from artificial ageing. The precipitate size, density and type and whether they are shearable or non-shearable are largely dependent on the ageing time. The alloy has highest strength at high strain in the peak-aged temper and the lowest in the over-aged temper. The condition of the alloy also affects the stress-strain behavior, but not to the same extent as the temper. The influence of the condition on the stress-strain behavior can be explained by the fact that the precipitation kinetics may be different dependent on the history of the material, or because the precipitate structure is different (different type, density, and size), but it may also be because of different textures.

The characterization of the compressed microstructures (only the over-aged samples) revealed that shear bands have been formed during the upsetting test.

The shear band formation is much more pronounced in the extruded condition compared to the other conditions in the same temper, which has lead to a much more non-uniform deformation in the grain structure. However, the over-aged extruded condition also showed the most symmetric macroscopic deformation during the compression compared to the other conditions in the same temper. This may be explained by the recrystallization texture present in the extruded condition.

The characterization of the compressed microstructure also revealed pore formation in the over-aged as-cast condition and in the over-aged extruded, cold-rolled, and recrystallized condition, but not in the over-aged extruded condition. This can be explained by the fact that the cohesion between the particles and the surrounding matrix is much better in the extruded condition because the extrusion process have been performed at elevated temperatures (500-550°C).

Based on the fact that the extruded condition exhibit a much more symmetric macroscopic deformation during compression, and that no pore formation have been formed after the compression it may seem as though the AlMgSi alloy exhibit the best compression properties and is less prone to pore formation and ductile fracture initiation in the extruded condition

Sammendrag

I dette prosjektet ble en AlMgSi-legering med små mengder Fe undersøkt. Målet var å studere hvordan den termomekaniske prosesseringen påvirker de mekaniske egenskapene under kompresjon, avhengig av kornstruktur, tekstur og utherding. Legeringen ble undersøkt etter kompresjon for å kartlegge tendensen til poredannelse og muligheten for bruddinitiering.

Den initiale mikrostrukturen til AlMgSi-legeringen i tre forskjellige tilstander; i) som-støpt tilstand, ii) som-ekstrudert tilstand, og iii) som-ekstrudert, kaldvalset og rekrystallisert tilstand, har blitt karakterisert med tanke på kornstruktur, tekstur og jernpartikler. En ekstrudert og kaldvalset tilstand ble også undersøkt, men kun i forbindelse med karakteriseringen av den initiale mikrostrukturen. De forskjellige tilstandene ble analysert med både LM (lysmikroskop) og SEM (scanning elektronmikroskop) før de ble varmebehandlet på 175°C til forskjellige utherdingstilstander; undereldet tilstand (2 timer), maksimal hardhet (8 timer), og overeldet tilstand (11 dager). De mekaniske egenskapene til de forskjellige tilstandene, med forskjellige utherdinger, ble undersøkt ved kompresjonstesting. Til slutt ble mikrostrukturen til de komprimerte prøvene karakterisert med både LM og SEM for å studere endringene i mikrostrukturen som følge av den deformasjonen som prøvene ble utsatt for under kompresjonstesten.

Ut fra karakteriseringen av den initiale mikrostrukturen til legeringen i forskjellig tilstander er det tydelig at mikrostrukturen er sterkt avhengig av den termomekaniske prosesseringen som legeringen har vært utsatt for. Resultatene fra kompresjonstestingen viste at utherdingstiden i stor grad påvirker spennings-tøyningsoppførselen til legeringen under kompresjon. Forskjeller i spennings-tøyningsoppførsel, slik som flytespenning og arbeidsherding, kan forklares ved hjelp av presipitatene som dannes under utherdingen. Størrelse, tetthet og type av presipitater og hvorvidt de er skjærbare eller ikke-skjærbare er sterkt avhengig av utherdingstiden. Styrken til legeringen varierer med hvilken utherdingstilstand den er i og den utviser størst styrke etter å ha blitt utherdet til maksimal hardhet, og lavest styrke etter å ha blitt utherdet til overeldet tilstand. Hvilken tilstand legeringen er blitt termomekanisk prosessert til har også en viss effekt på spennings-tøyningsoppførselen, men ikke i samme grad som utherdingstilstanden. Den effekten som tilstanden til legeringen har på spennings-tøyningsoppførselen kan muligens forklares med at presipiteringskinetikken er forskjellig avhengig av den termomekanisk historien til legeringen, eller det at selve presipitatstrukturen er forskjellig (størrelse,

tetthet og type). Ulik tekstur hos de forskjellige tilstandene kan også være en mulig forklaring.

Karakteriseringen av mikrostrukturen til de komprimerte prøvene (kun i overeldet tilstand) viste at skjærbånd har blitt dannet under kompresjonstestingen. Skjærbåndene er mye mer tydelige hos den ekstruderte tilstanden sammenlignet med de andre to tilstandene i samme utherdingstilstand, noe som har ført til en veldig ikke-uniform deformasjon av kornene. På samme tid var det den ekstruderte tilstanden som også utviste den mest symmetriske makroskopiske deformasjonen under kompresjonstestingen av alle de tre tilstandene. Dette kan muligens forklares ved hjelp av rekrystallisasjonsteksturen til den ekstruderte tilstanden.

Det ble også påvist poredannelse i den komprimerte mikrostrukturen til både den overeldede som-støpte tilstanden og den overeldede ekstruderte, kaldvalsede, og rekrystalliserte tilstanden, men ikke hos den overeldede ekstruderte tilstanden. Forklaringen på dette kan ligge i at partiklene i den ekstruderte tilstanden vil ha bedre heft med matriks sammenlignet med de to andre tilstandene på grunn av at ekstruderingen har blitt gjennomført ved høye temperaturer (500-550°C).

Basert på det faktum at den ekstruderte tilstanden utviste den mest symmetriske makroskopiske deformasjonen under kompresjonstestingen, samt at ingen poredannelse ble påvist hos denne tilstanden, kan det tyde på at AlMgSi-legeringen har beste kompresjonsegenskaper og er minst utsatt for poredannelse og bruddinitiering når den er i ekstrudert tilstand.

Contents

1 Introduction

Aluminium and its alloys are one of the most commercially used metals today and are utilized in a wide range of applications in various industries, and the automotive industry is one of them. Car manufacturers first used aluminium in cars for decorative reasons already back in 1914. Today more than 100 car elements are made from aluminium alloys including safety components such as bumper beams and crash boxes [1]. However, in order to be used as bumper beams and crash boxes, the aluminium alloys have to meet certain requirements; light weight, good mechanical properties such as high strength and high stiffness, high energy absorption capability, and good deformability [2], in other words they need to show good compression properties. Aluminium alloys that meet these requirements are the age-hardenable alloys like the AlMgSi alloy (6xxx series).

AlMgSi alloys belong to age-hardenable alloys, which gain their strength from work-hardening, precipitation-hardening, and alloying elements in solid solution. The mechanical properties of these alloys are strongly dependent on the thermomechanical history of the material, i.e. what condition it is in and which temper it has been heat-treated to, and it is therefore important to understand the relationship between microstructure evolution during thermomechanical processing and the mechanical properties. Particles (both MgSi precipitates and constituent Fe containing particles) present in the material will have a great influence on the mechanical properties, and they are also dependent on the thermomechanical history of the material. Aluminium alloys will inevitably contain a certain amount of iron (Fe), as an impurity from bauxite, and this iron content tend to accumulate during recycling of aluminium. Aluminium is well known for its recyclability, and the energy required to recycle aluminium is much lower than required to produce primary aluminium (only 5%). The accumulating Fe content may be a problem for aluminium alloys used in car components as the Fe particles may lead to pore formation and eventually ductile fracture initiation due to particle cracking or decohesion from the surrounding aluminium matrix when the material is introduced to different loadings.

This is the background for the present work, for which the aim is to obtain experimental data in order to analyze and evaluate the mechanical properties in compression for aluminium alloys and how these properties are influenced by the thermomechanical processing and the particles (both MgSi precipitates and constituent Fe containing particles) present in the material. The experimental setup for this work includes characterization (with both optical microscopy

(OM) and scanning electron microscopy (SEM)) of the initial microstructure of an AlMgSi alloy in different conditions with respect to grain structure, texture and constituent particles. It also includes artificial ageing at 175°C of the alloy to different tempers before performing an upsetting test on the different conditions/tempers. This is to look at the deformation behavior, and to evaluate the stress-strain response to compression. Finally, the experimental setup also includes a characterization (with both OM and SEM) of the compressed samples with respect to grain structure and constituent particles in order to evaluate the microscopic deformations and to look for possible pore formation, which could eventually lead to a ductile fracture initiation.

This work is a small part of a much larger project at the CRI (Center for Research-based Innovation) SIMLab (Structural Impact Laboratory) at the Department of Structural Engineering, Norwegian University of Science and Technology (NTNU), and SINTEF Materials and Chemistry.

2 Theory

2.1 Aluminium

Aluminium alloys are divided into two major groups depending on their fabrication methods: wrought and cast alloys. Cast alloys will not be further discussed in this report since only wrought alloys were used in this work. Wrought alloys are designated by the numbering system shown in Table 1. The first number specifies the primary alloying elements, while the remaining numbers specifies the composition of the alloy[3].

Table 2-1: Aluminium designation system for wrought alloys[3].

Alloy series	Alloying elements	Age-hardenable
1xxx	Commercially pure Al (>99% Al)	No
2xxx	Al-Cu and Al-Cu-Li	Yes
3xxx	Al-Mn	No
4xxx	Al-Si and Al-Mg-Si	Yes, if magnesium is present
5xxx	Al-Mg	No
6xxx	Al-Mg-Si	Yes
7xxx	Al-Mg-Zn	Yes
8xxx	Al-Li, Sn, Zr, or B	Yes

Wrought aluminium alloys can be further divided, into age-hardenable alloys and non age-hardenable alloys. This division is based on whether the alloys have the ability to be precipitation hardened (age hardened) or not (see Table 2-1) [4]. Age hardening will be further described in section 2.2.4.

2.1.1 Al-Mg-Si alloys

The AlMgSi alloys of the 6xxx series are one of the age-hardenable aluminium alloys. These are of medium to high strength and they can be strengthened by heat treatment (age hardening), through the presence of silicon and magnesium (mostly in the range of 0.3-1.5 wt% Si and Mg), which are the main alloying elements of these alloys. These alloys also have excellent corrosion resistance and good weldability, and in combination with high strength and formability these alloys are used in a vast variety of applications: transport (automotive outer body-panels, railcars, etc.), building (doors, windows, ladders, etc.), marine (offshore structures, etc.), heating (brazing sheet, etc.), etc. The 6xxx series are often extruded to be used for machined products [5].

2.2 Aluminium Processing

After casting, in order to be utilized in commercial use the aluminium alloys needs to be further processed. A typical processing route for the alloy studied in the present work includes homogenization, extrusion, cold rolling, and age hardening. A schematic illustration of a normal processing route for aluminium alloys can be seen in Fig. 2-1 [6].The different processing steps indicated will be described in the following sections.

2.2.1 Homogenization

Homogenization is an important part of the processing route for many aluminium alloys, and is usually performed at high temperatures (450-600°C) [6]. As-cast aluminium alloys tend to have very non-uniform microstructures, and homogenization can be applied in order to eliminate micro segregations and super saturations [7]. There are three main reasons for homogenizing AlMgSi alloys: The first is to obtain a uniform distribution of alloying elements in solid solution, the second is to dissolve low melting point Mg_2Si and Si particles which can cause tearing during extrusion. The third main reason for homogenization of AlMgSi alloys is to transform β-AlFeSi phase particles into α-AlFeSi (α-AlFeMnSi) phase particles, which is assumed to give better extrusion properties [8]. The homogenization process is performed after casting of the alloy and prior to the extrusion, as seen in Fig. 2-1. The homogenization process consists of three distinct steps; heat-up (heating step), soak and cooldown (cooling step) [6].

The first homogenization step is heat-up, and if there are some low melting temperature phases in the as-cast microstructure, they will dissolve by diffusion during the heat-up step. The second homogenization step is the soak, and it is the key step in the development of second-phase particles (dissolution of primaries, precipitation of new phases and possible phase changes) [6]. The soak temperature (with respect to the appropriate phase diagram) is generally the most important factor for the precipitation of particles. Different particles may precipitate at different temperatures, and the soak time may also play a key role in the evolution of the second-phase particle structure [9]. The third and last homogenization step is the cooldown. In the cooldown step it is important to cool rapidly, but to avoid quenching since it will raise the flow stress of the alloy in the further processing. For the 6xxx alloys, the cooldown step is where the magnesium silicon particles are precipitated [6].

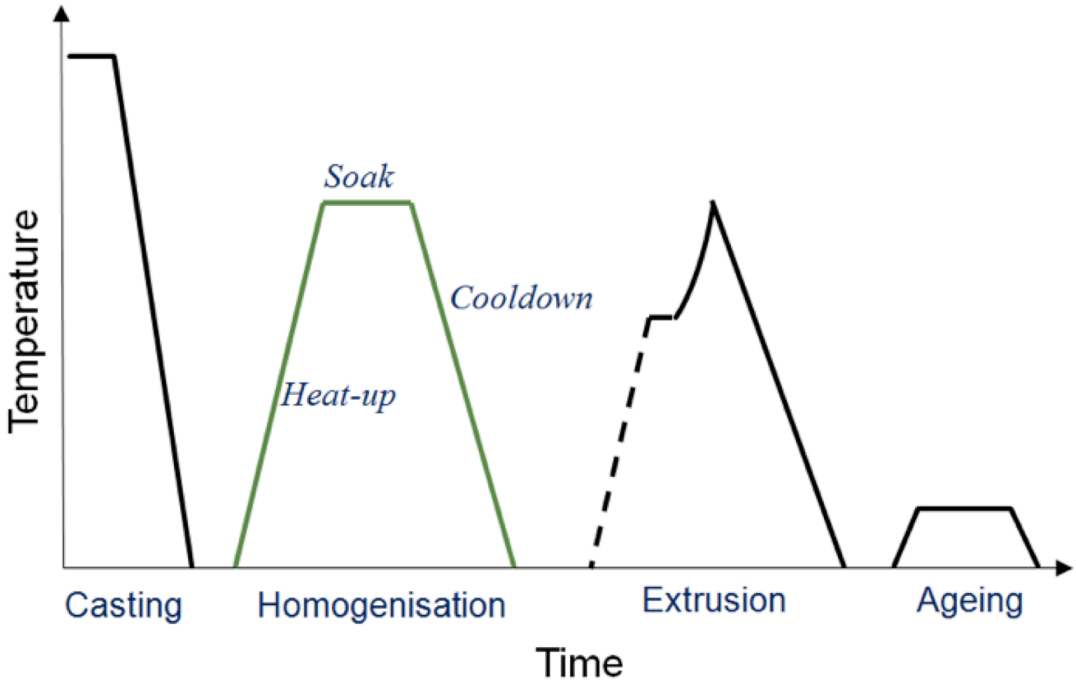

Fig. 2-1: Simplified overview of a normal processing route for aluminium alloys [6].

2.2.2 Extrusion

Because of its good formability, aluminium is a metal very well suited for extrusion, which is a common processing method used for many commercial aluminium alloys and in particular the 6xxx series alloys. In the extrusion process a block of metal is forced through a die orifice under high pressure, which causes a reduction of the metal block diameter. Extrusion is generally used to produce cylindrical bars, hollow tubes or other complex shapes [10]. Fig. 2-2 shows some examples of how complex the extruded shapes can be. Most metals are extruded hot under conditions where the deformation resistance of the metal is low; this is because of the large forces required in the extrusion process. The extrusion process normally takes place in the temperature range of 500-550 °C, which is high enough to make the metal fairly soft, but still below the melting temperature of aluminium (660.3 °C for pure aluminium, little lower for alloys) [10, 11]. Fig. 2-3 illustrates the principles of extrusion.

Fig. 2-2: Examples of extruded materials showing the complexity of the extruded shapes[12].

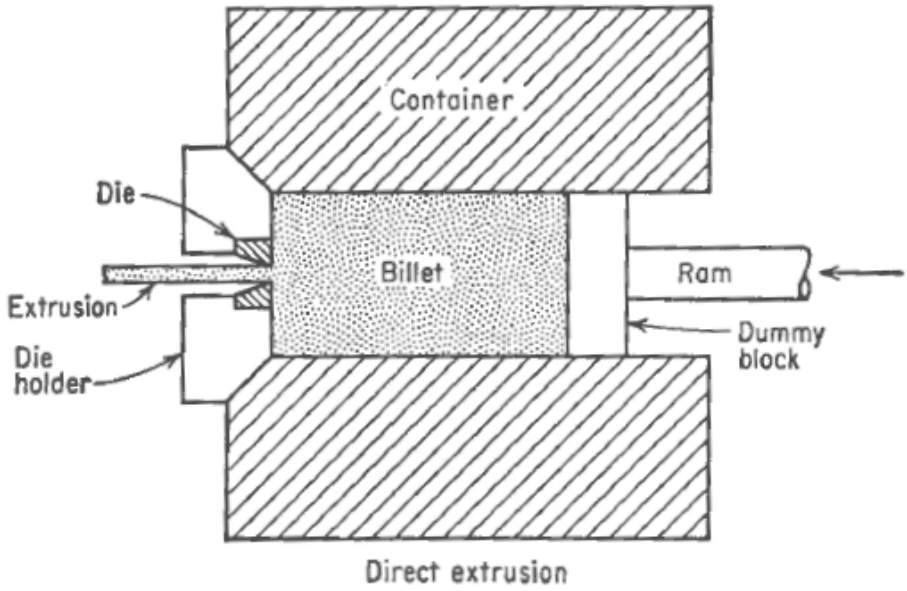

Fig. 2-3: Principle of direct extrusion[10].

2.2.3 Cold-rolling

The good formability of aluminium does not only make the metal well suited for extrusion, its beneficial properties also make it well suited for cold rolling. Rolling is the name of the process that plastically deforms a metal by passing it between rolls. This process allows a high production rate and close control of the final product, and hence it is the most widely used metalworking process in the world. Rolling can be done both hot and cold, but hot rolling will not be further described since only cold-rolling has been used in this work. Cold-rolling of metals has a major importance in the industry, and can be used to produce sheets, strips and foils of metals, which will get a good surface finish and increased mechanical strength. The strain hardening that comes from cold-rolling may be used to increase the strength of the material. The simplest and most common type of rolling mills is the two-high mill, and is also the mill type used in this work [10]. A schematic illustration of cold-rolling is given in Fig. 2-4.

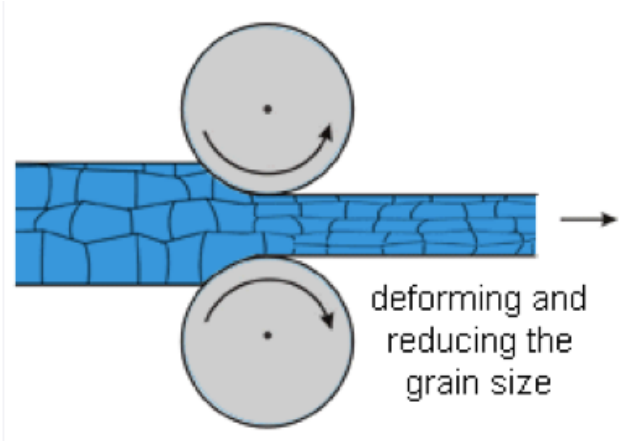

Fig. 2-4: Schematic illustration of cold-rolling [13].

2.2.4 Age hardening

As already mentioned, in order to be used as car safety components the aluminium alloys needs to exhibit good strength. There are various hardening mechanisms that can be used in order to increase the strength of aluminium alloys, and age hardening is one of them, and the most important for AlMgSi alloys.

There are three steps in the age hardening heat-treatment of aluminium alloys. These three steps are schematically illustrated in Fig. 2-5 [14]. The figure shows an illustration of an Al-Cu system but the principle is the same for all age-hardenable aluminium alloys. The first step in the age hardening process is solid solution heat treatment. In this step a homogeneous solid solution, α, is formed by heating the alloy to a temperature above the solvus temperature to dissolve secondary particles and bring as much as possible of the solute into solid

solution. The second step is quenching. When the alloy is quenched the rapid cooling causes the solid α to form a super saturated solid solution α_{SS}. The last step is ageing. In this step the α_{SS} is reheated to below the solvus temperature in order to form finely dispersed precipitates, this is called artificial ageing [15]. There is also a possibility that hardening 'phases' may develop at ambient temperatures, this is called natural ageing[4].

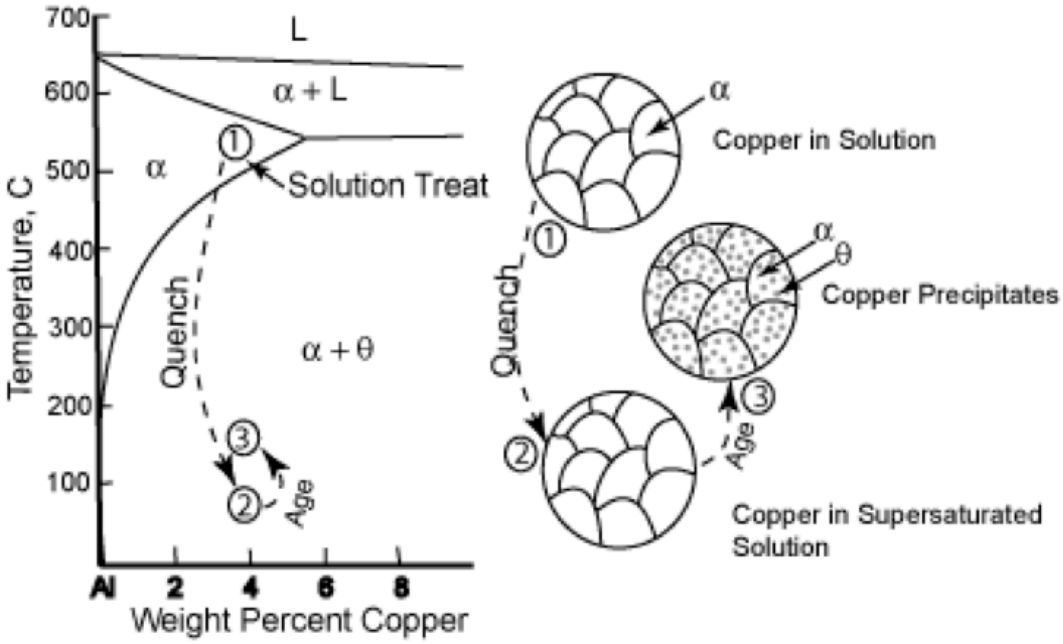

Fig. 2-5: Schematic illustration of the three steps of age-hardening; (1) solid solution heat-treatment, (2) quenching, (3) ageing [14].

Artificial ageing is characterized by different behavior in which the hardness usually increases to maximum (peak-aged) and then decreases (over-aged) if the heat-treatment continues [16]. Artificially aged materials that have not reached the maximum hardness yet are under-aged. A schematic illustration of a normal ageing curve is shown in Fig. 2-6, where the material is under-aged at point (1), peak-aged with maximum hardness at point (2), and over-aged at point (3), where the hardness has started to decrease again. Maximum hardness usually occurs when the alloy has a critical dispersion of GP zones, or an intermediate (metastable) precipitate, or a combination of both. More than one intermediate precipitate may form, and in alloys that are cold-worked after quenching and prior to ageing, the dislocation density is increased and there will be more sites at which heterogeneous nucleation of intermediate precipitates may occur during ageing [16]. The interaction between precipitates and dislocations is very important for all the age-hardenable aluminium alloys. This interaction may be split into two general cases depending on the precipitate size [17]. The first case is the shearable precipitates, where the dislocations are able to cut through the precipitates, a schematic illustration of a dislocation cutting a particle can be

seen in Fig. 2-7 a) [18]. The second case is the non-shearable precipitates, where the precipitates become too large of an obstacle for the dislocations to cut through. The dislocations are forced to either climb over the precipitate or to leave a dislocation loop around it, this is called the Orowan mechanism. A schematic illustration of the Orowan mechanism is shown in Fig. 2-7 b). At low ageing times the precipitates are very small and easy to cut through and are regarded as much weaker obstacles than the other dislocations. However, they become stronger and stronger with increasing ageing time before they become non-shearable [17, 18].

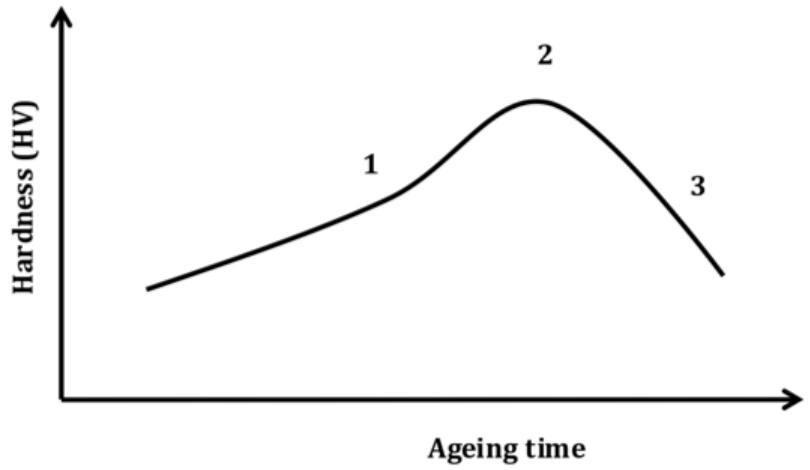

Fig. 2-6: Schematic illustration of a typical ageing curve. The material is under-aged at point (1), peak-aged with maximum hardness at point (2), and over-aged at point (3), where the hardness has started to decrease again.

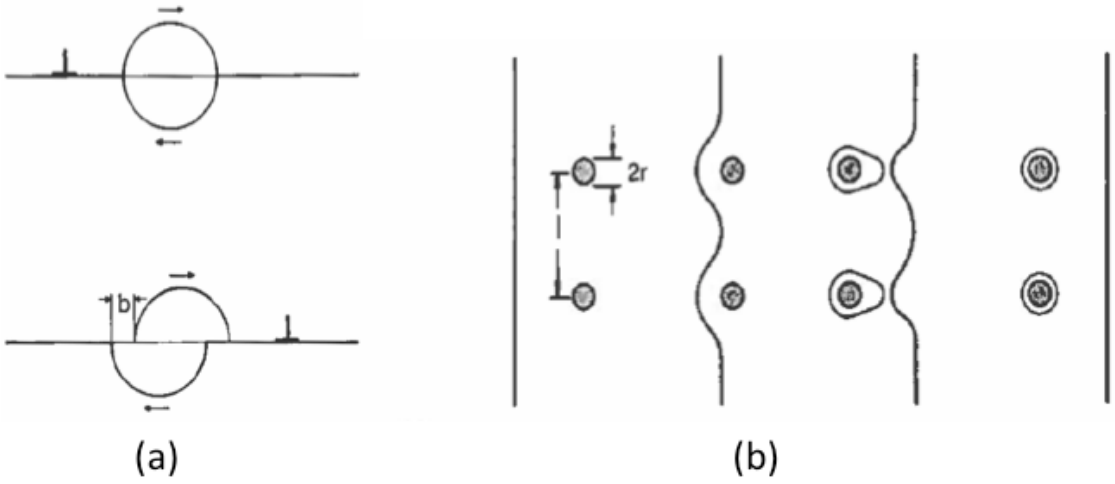

Fig. 2-7: Schematic illustrations of: (a) a dislocation that cuts through a particle, and (b) the Orowan mechanism [18].

The ageing processes in the AlMgSi system are complex, and the appearance of individual clusters of magnesium and silicon atoms, followed by the formation of co-clusters of both elements may initially precede the formation of GP zones [16]. Needle-like Mg_2Si precipitates will appear during the ageing of AlMgSi alloys. However, these precipitates will not occur in Precipitation Free Zones (PFZ), which are adjacent to the grain boundaries and depleted of precipitates. The size of the PFZ's is dependent on the temperature of the heat-treatment, while the morphology and the density of the precipitates are dependent on the heating time [19].

A normal ageing sequence for AlMgSi alloys is given by [20]:

α_{SS} → Clusters of Si atoms, clusters of Mg atoms → Dissolution of Mg clusters → Formation of Mg/Si co-clusters → Small precipitates of unknown structure (GP zones) → β'' precipitates → B' and β'' precipitates → βMg_2Si precipitates

The Mg:Si ratios are close to 1.1 in the Mg/Si clusters co-clusters, the small precipitates, the β'' precipitates and the B' precipitates [20]. The MgSi precipitates inhibits the movement of dislocations, and there is high energy required in order to break the Mg-Si bonds, and it is suggested that this is one of the reasons for the strengthening in these alloys [4]. The main strengthening phase in AlMgSi is found to be the needle-shaped β'' precipitates, and the hardness of the alloy reaches it peak when the β'' precipitates have a maximum density, and the hardness starts to decrease again once the β' and β precipitates starts to appear (during over-ageing) [21]. Which temper the material is heat-treated to affects its stress-strain behavior. This can be seen in Fig. 2-8, which shows the stress-strain curves of a 6xxx series aluminium alloy (AA6082) that have been predicted by Myhr et al. [22]. The figure illustrates the different stress-strain behavior of the different tempers. The initial flow stress of the under-aged material (W10) is predicted to be low because of a low density of β'' precipitates, and hence a low age hardening effect. However, the work-hardening potential will be large due to a high level of solute. The material heat-treated to peak-aged temper (T6) on the other hand, is predicted to have an initial flow stress at peak levels, but at the same time have a decreasing contribution of work-hardening due to solute depletion. Finally, the over-aged material (T7) is predicted to have a lower initial flow stress (than the peak-aged material) because of particle coarsening due to the long ageing time in combination with excessive draining of solute from the aluminium matrix. It is also predicted that all the precipitates in the over-aged material is non-shearable, and hence of the Orowan type, and because of this the storage of geometrically necessary dislocations in their vicinity will lead to a high initial work-hardening rate. However, the rapid increase in σ (true stress) will diminish as the accumulation

of dislocation loops around the precipitates will start to cease and the flow stress will be saturated almost immediately after that, causing the stress-strain curve to flatten out [22].

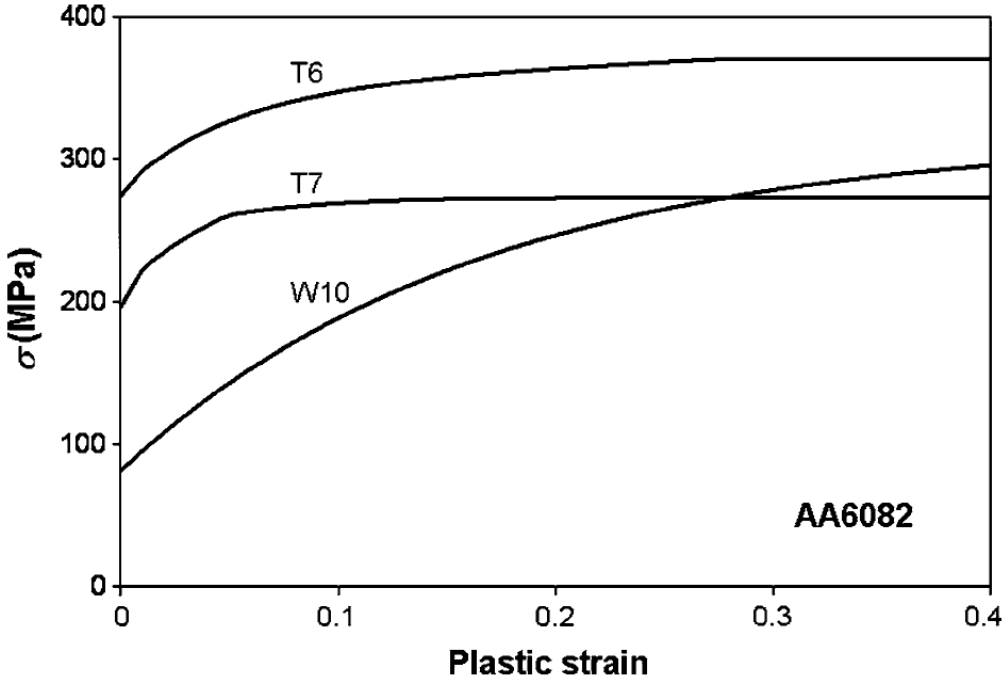

Fig. 2-8: Stress-strain behavior of a 6xxx alloy in under-aged temper (W10), peak-aged temper (T6), and over-aged temper (T7) predicted by Myhr et al. [22].

2.3 Changes in microstructure and properties due to thermomechanical processing

When aluminium alloys undergo thermomechanical processing there will be changes in the microstructures. An illustration of the microstructural features in a rolled aluminium alloy that can develop during deformation is shown in Fig. 2-9. From the figure it can be seen that slip has occurred within the individual grains, which have been elongated. The elongated grains have caused a large increase in the total grain boundary area. Point (a) in the figure shows a deformation band or transition band within one grain that separates two internal regions that have developed two distinct orientations during the deformation process. Point (b) shows coarse intermetallic compounds, (c) shows previous grain boundaries, and (d) shows a shear band, which is a larger discontinuity that tends to form in regions of high strain (true strain $\varepsilon > 1$). These shear bands are typically oriented at ~35° to the rolling plane and cut through existing grain structures. All four points shown in the figure are possible nucleation sites for recrystallized grains [16]. The shear bands are a result of strain homogeneity during rolling and in order to be formed they are strongly dependent on the deformation conditions. Their formation is also dependent on the composition and the texture, as well as the microstructure of the material [23].

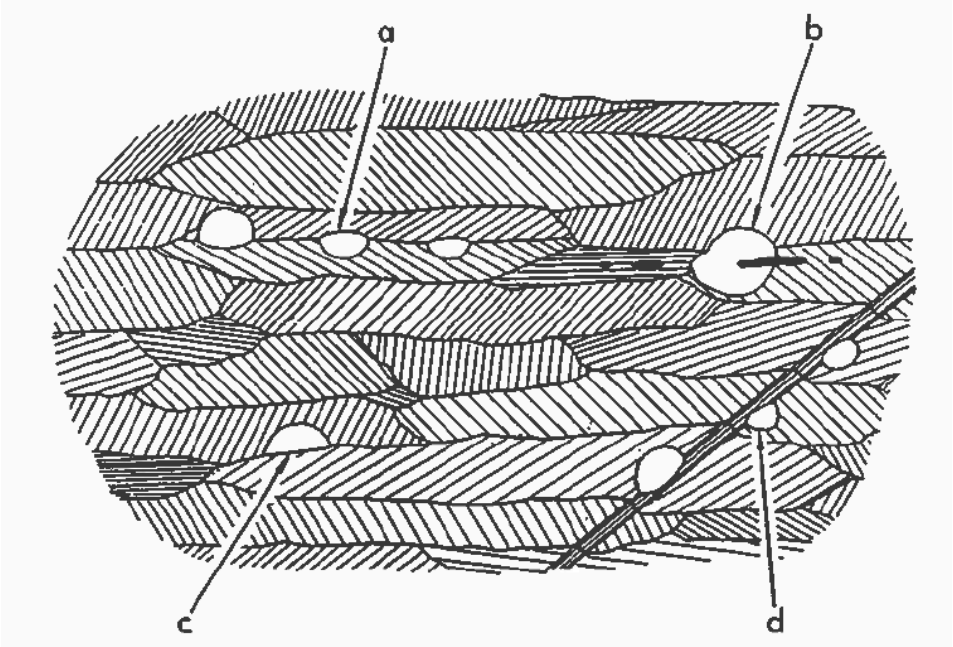

Fig. 2-9: Schematic representation of the microstructure of a rolled alloy. Four possible nucleation sites for recrystallized grains are shown: (a) transition bands, (b) coarse intermetallic compounds, (c) previous grain boundaries, and (d) shear bands [16].

When aluminium and its alloys are being deformed, most of the work expended is given out as heat, and only a very small amount (~1%) will remain as stored energy in the material. The energy that is stored provides the source of all property changes that are typical of deformed metals and are mostly formed from dislocations generated during deformation [23]. During deformation, the grains of a polycrystalline metal will change their shape in correspondence to the macroscopic shape change, e.g. the grains gets elongated, which results in an increase in the total grain boundary area [23].

The dislocation density (ρ_{dis}) is related to the true strain (ε) by

$$\varepsilon = \rho_{dis} b L \qquad \text{(Eq.1)}$$

where b is the Burgers vector and L, the slip length, is the average distance of which the dislocations have moved before being stored during deformation. The energy that is stored in a material is related to the total dislocation density and given by:

$$E_D = c\rho G b^2 \qquad \text{(Eq.2)}$$

where c is a constant in the order of 0.5, and G is the shear modulus [23].

2.3.1 Annealing and recrystallization

Every material wants to minimize the energy they have stored from deformation. By heat-treating the deformed materials (e.g. annealing, solid solution heat-treatment, artificial ageing) they will be relieved from some of the stored energy by reorganization of the dislocations and by formation of subgrains. A schematic illustration of the main annealing steps is shown in Fig. 2-10. The microstructure in (Fig. 2-10 a) shows the material in deformed state, and (Fig. 2-10 b) shows the material in recovered state. When the material is recovered the dislocation structure is partially removed and it reaches a metastable state, and the properties are partially restored. A schematic illustration of the various stages in the recovery of a plastically deformed material is shown in Fig. 2-11 [23]. During deformation the dislocation generation and multiplication will occur faster than annihilation by dynamic recovery. This will lead to an increase in the dislocation content. The increasing amount of dislocations will cause them to tangle (Fig. 2-11 a), and cells will start to form (Fig. 2-11 b). Then there will be annihilation of the dislocations within these cells (Fig. 2-11 c) and subgrain walls will start to form (Fig. 2-11 d), and eventually the subgrains will start to grow (Fig. 2-11 e). This will cause changes to the grain shapes and the internal structure. These are factors that decrease the mean free slip distance and give increased strength to the material [16, 23]. Further restoration of the properties of the deformed material is called recrystallization (Fig. 2-10 c), where new dislocation-free grains are formed within the deformed or recovered structure. These will grow and consume the old grains and create a new grain structure with a low dislocation density (Fig. 2-10 d). Even though the recrystallization removes the dislocations, the material will still have grain boundaries, and these are thermodynamically unstable (represent excess energy to the material). If the material is further annealed it may result in grain growth (Fig. 2-10 e), where smaller grains are eliminated and the larger grains grow and the grain boundaries assume a lower energy configuration [23]. In particular, it is the mechanical properties and the microstructure that is most strongly affected by annealing and heat-treatment subsequent to plastic deformation, while other physical properties (e.g. electrical resistivity) are barely influenced. This can be seen in Fig. 2-12, which illustrates the effect of cold forming and annealing on different properties (for Cu35%Zn alloy, but the principle is the same for heat-treatable Al alloys as well).

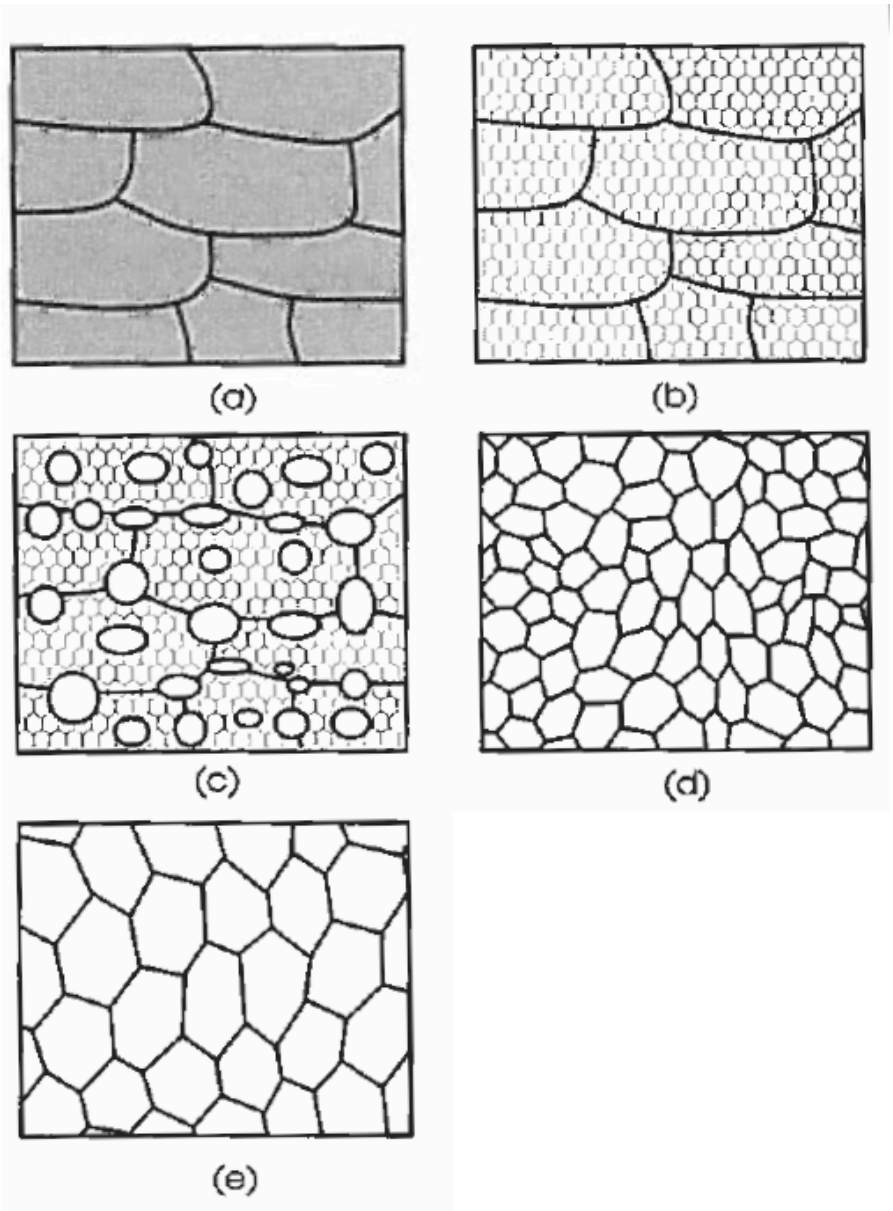

Fig. 2-10:Shcematic illustration of the main annealing processes; a) Deformed state, b) Recovered, c) Partially recrystallized, d) Fully crystallized, e) Grain growth [23].

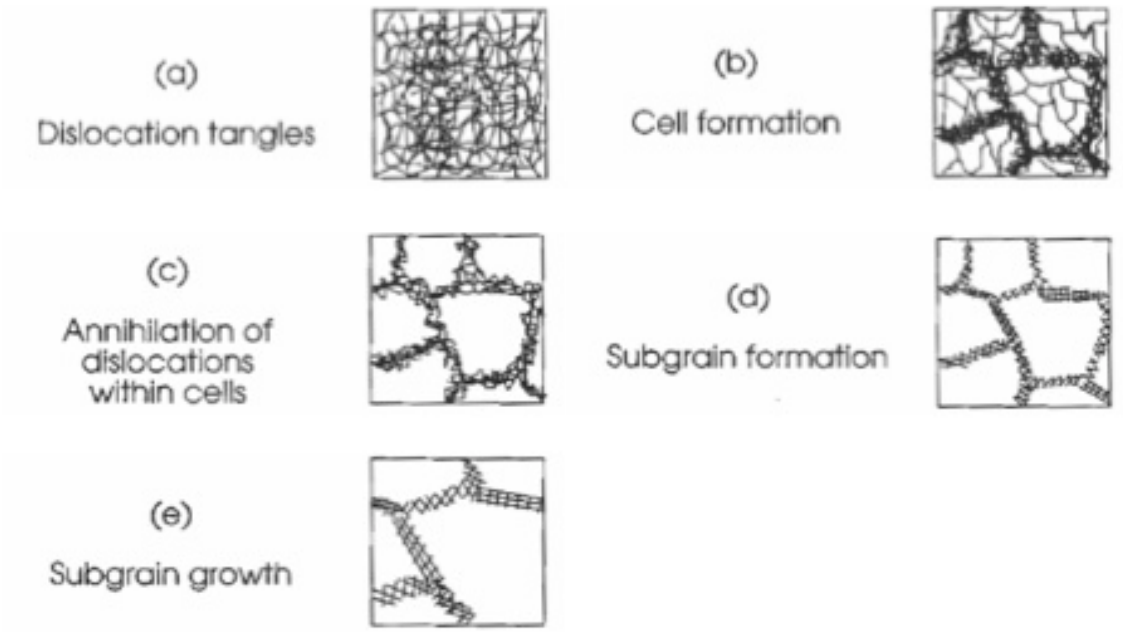

Fig. 2-11: Various stages in the recovery of a plastically deformed material [23].

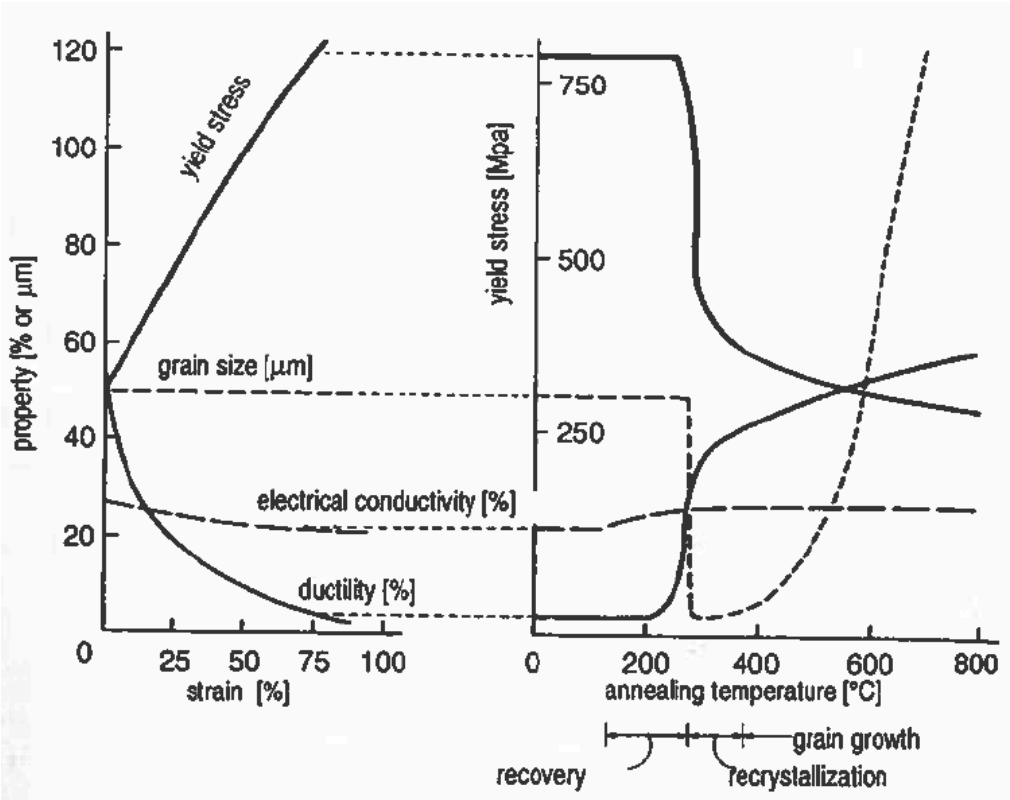

Fig. 2-12: Schematic illustration of the effect of cold forming and annealing on different properties. A Cu35%Zn alloy is used as an example [18].

2.3.2 Texture

The new grains that form during recrystallization in cold-worked aluminium alloys will have an orientation that differs from the old grains. The texture and final grain size in recrystallized products are very dependent on the amount of cold-work and the annealing conditions (i.e. rate of heating, annealing temperature, and annealing time), but also the composition and the size and distribution of intermetallic compounds is of importance, as they tend to restrict grain growth [16]. A material is said to have a crystallographic texture when the grains are not randomly oriented. Materials can also show a morphological texture, when all the grains are oriented in one or more preferential directions. Fig. 2-13 gives an illustration of this. The orientation of a grain is always expressed relative to an external coordinate system, and in flat products this external reference frame consists of the rolling direction (RD) or extrusion direction (ED) in the case of extrusion, the normal direction (ND) and the transverse direction (TD) [24].

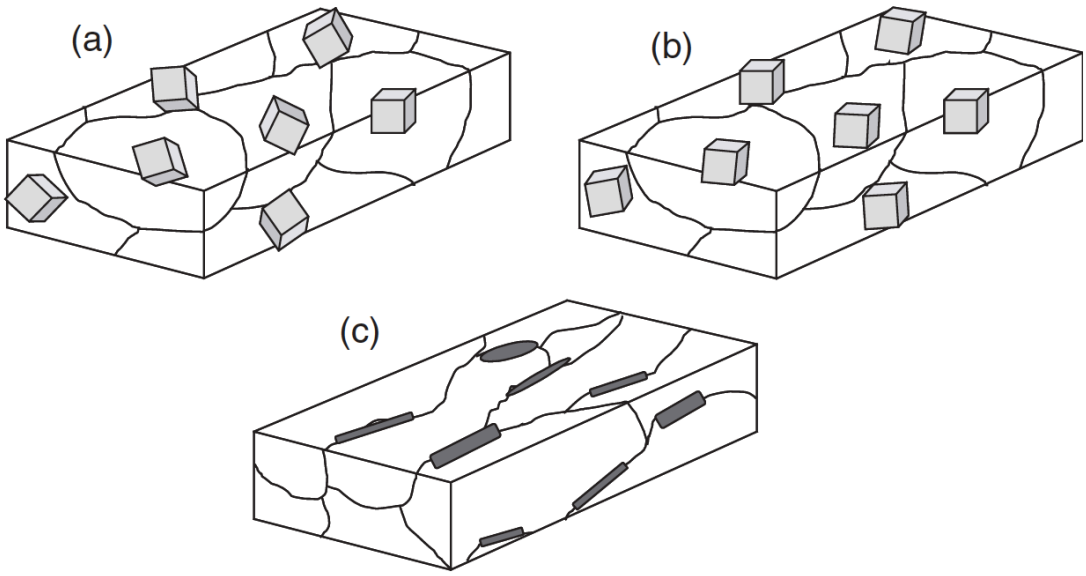

Fig. 2-13: Schematic illustration of a material with; a) no texture, b) crystallographic texture, and c) morphological texture. The small cubes represent the crystallographic orientations of the grains [24].

Textures that are developed during cold-working of a material will cause directionality (anisotropy) in certain mechanical properties. Both the yield and tensile strength can be increased in the working direction, this is called texture hardening, and it has been estimated that, with an ideal fiber texture the strength in the fiber direction may be 20% higher than that for sheet with randomly oriented aggregates of grains [16].

In order to understand the different crystallographic textures in a material and how it affects the properties in the material it is important to have methods of representing the texture and to be able to characterize them. One way of graphically representing the texture data is by the means of pole figures, which are based on stereographic projections. The principle behind stereographic projection is illustrated in Fig. 2-14. In stereographic projection the unit cell of the face-centered-cubic (fcc) aluminium is represented by a unit cube, which is located in the origin of the coordinate system and is surrounded by the unit sphere. The rolling plane normal (ND) is pointed towards the north pole of the unit sphere. A crystallographic direction is chosen (e.g. <100>) and a line is drawn from the cube center and through the 100-planes to the unit sphere surface. Only the intersecting points on the northern hemisphere (the intersections 1, 2, and 3) are taken into account. Then these points are connected in the south pole, which gives the intersecting points (1', 2', and 3') in the equatorial plane. These are the projection points, and the equatorial plane with all the intersecting points of the <100> directions, is called the <100> pole figure [24, 25].

It is not only the <100> orientations that can be used to construct pole figures, but all crystallographic directions. Fig. 2-15 shows a stereographic projection of <111> poles, which shows a Cube texture. Another way of representing the texture data is in the form of an ODF (Orientation Distribution Function), and with these it is possible to describe the complete texture information of a sample [24].

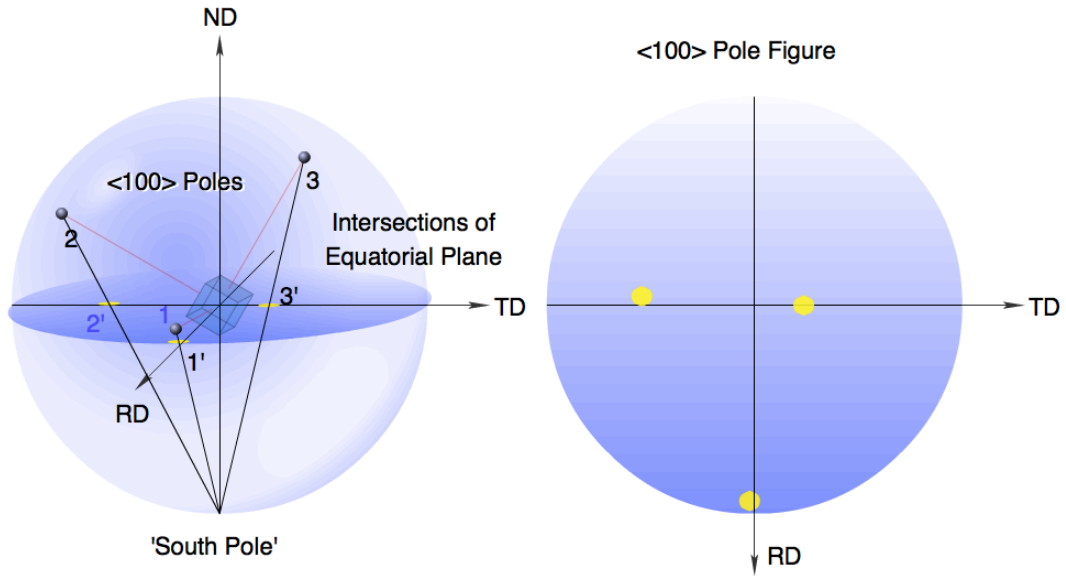

Fig. 2-14: Stereographic projection e in the form of a <100> pole figure [25].

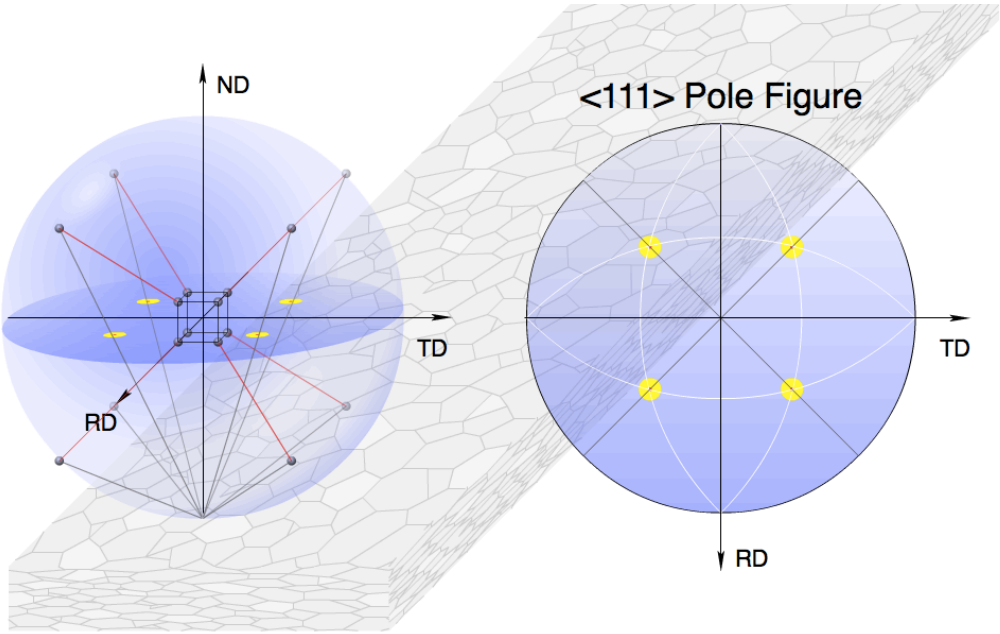

Fig. 2-15: Stereographic projection of a Cube texture in the form of a <111> pole figure [25].

The most important cold deformation textures are those that are developed during cold-rolling [24]. The rolling texture of aluminium alloys and many other fcc metals are dependent on the materials stacking fault energy (SFE). Aluminium has a relatively high SFE, and this prevents deformation twinning. Therefore, deformation in aluminium is solely attained through dislocations slip [26]. The development of a crystallographic texture is dependent on the crystal structure of the material and on the deformation mode, but also the starting texture [24]. Fig. 2-16 shows a schematic representation of a somewhat idealized form of the crystallographic texture after cold-rolling of an fcc material. The texture consists of two 'families' of orientations, the α- and the β-fibre. The fibres form a line through the Euler space [24]. 'Typical' deformation textures can be seen from the pole figure and the ODF shown in Fig. 2-17 and Fig. 2-18, respectively. The pole figure in Fig. 2-17 shows a double fiber texture in an Al alloy [26]. The ODF in Fig. 2-18 show the texture of an aluminium alloy measured after hot- and cold-rolling. The β-fibre components (Brass, S and Cu) are clearly present, and so is the Goss component. An additional Cube {100} <001> component is also visible. However, this is not a traditional component after cold-rolling, but a component that forms during recrystallization. This Cube component is still left from recrystallization during the hot-rolling prior to the cold-rolling, and this illustrates that the starting texture have an influence on the cold-rolling texture [24]. Typical rolling texture components in aluminium alloys are usually Copper ($\{112\}\langle 11\bar{1}\rangle$), Brass ($\{110\}\langle 1\bar{1}2\rangle$) and S ($\{123\}\langle 63\bar{4}\rangle$), and the 111 pole figures for these typical texture components can be seen in Fig. 2-19 a), b), and c), respectively [27].

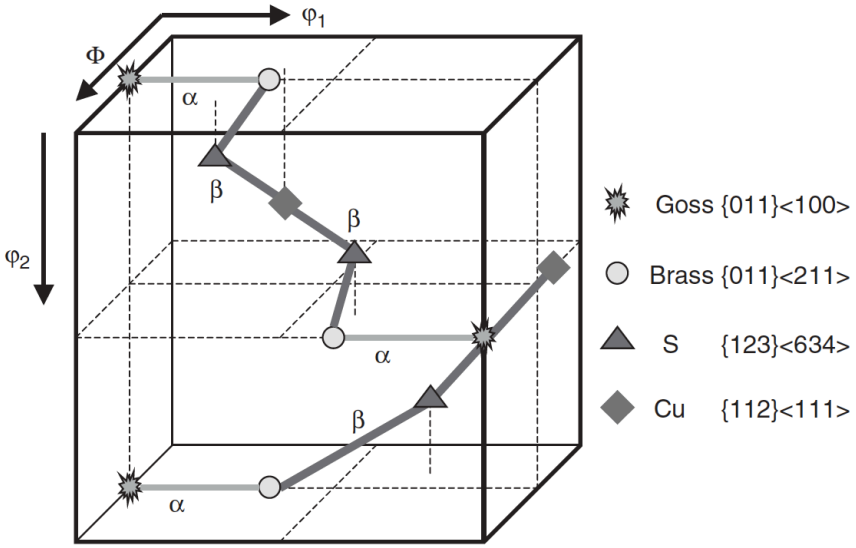

Fig. 2-16:Schematic representation of the cold-rolling texture of fcc materials [24].

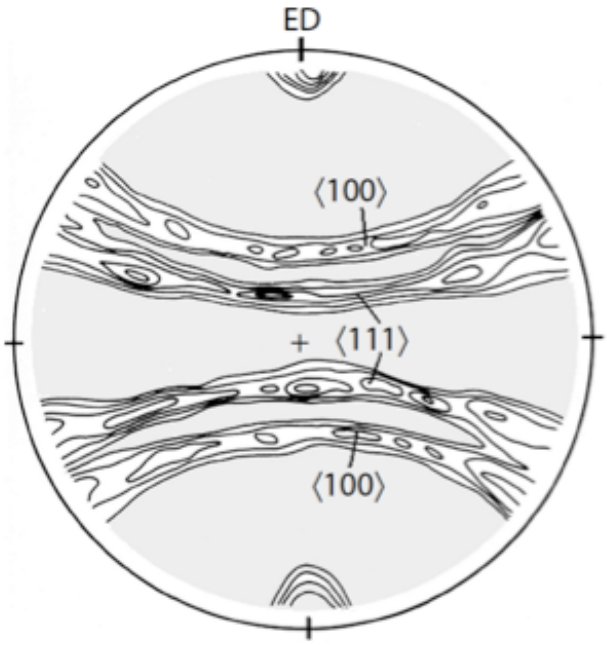

Fig. 2-17: Pole figure of a deformation texture in an Al alloy [26].

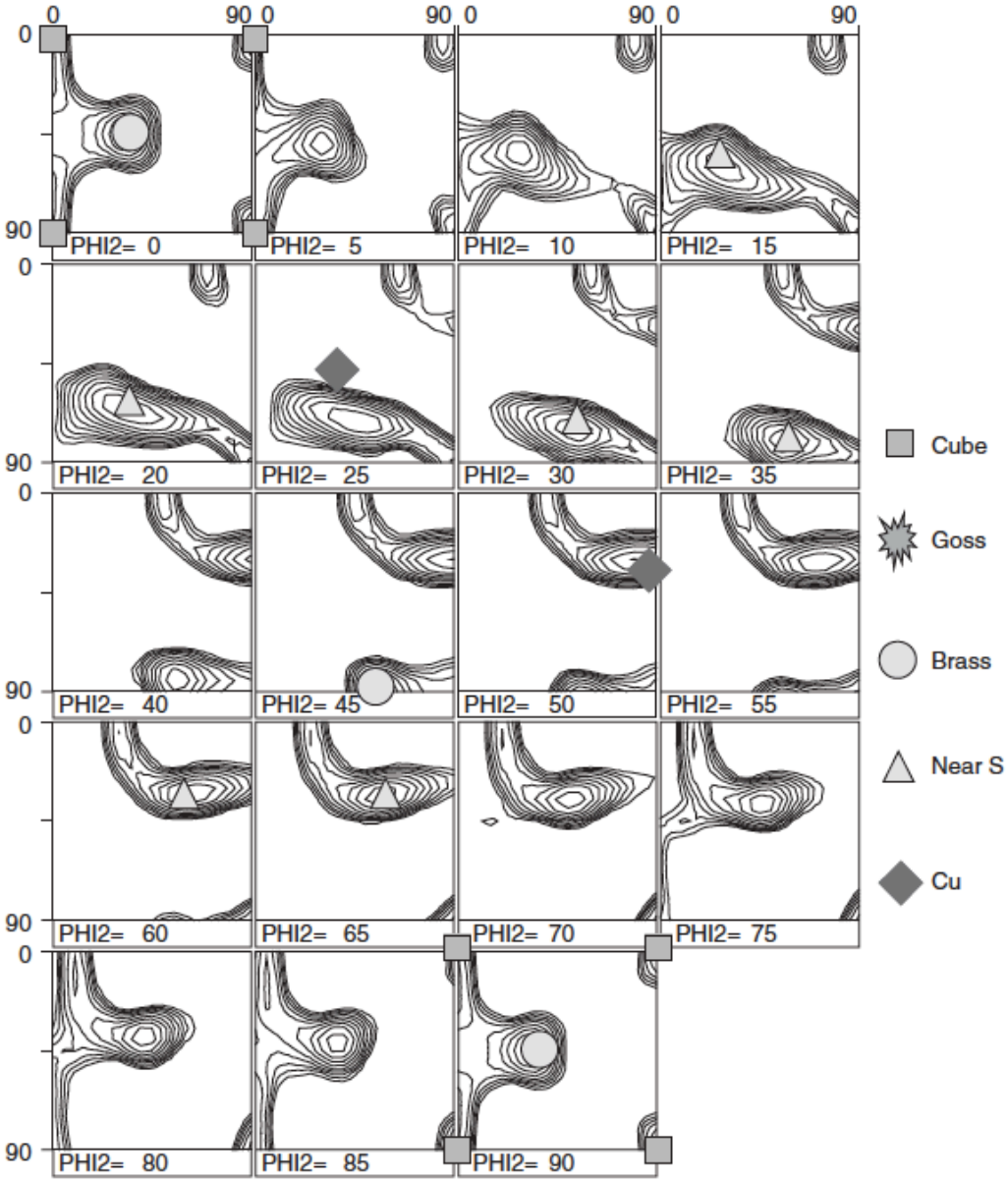

Fig. 2-18: ODF that shows the texture of an aluminium alloy measured after hot- and cold-rolling [24].

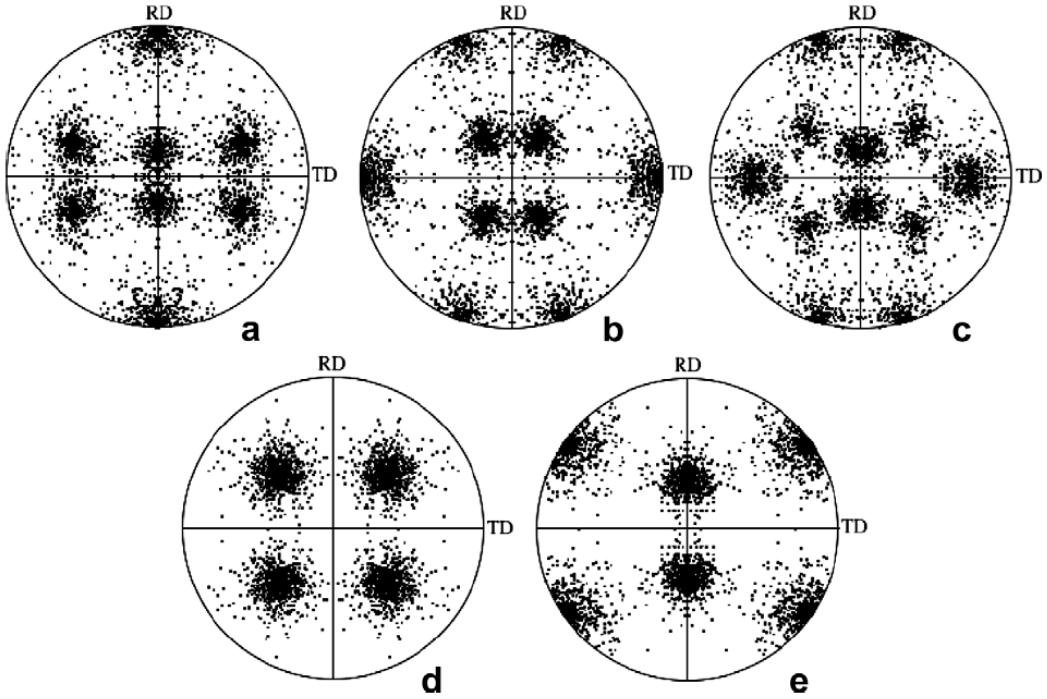

Fig. 2-19: {111} pole figures of computationally generated model textures with 1000 orientations with $\omega_0 = 15°$. (a) Copper texture, (b) Brass texture, (c) S texture, (d) Cube texture, and (e) Goss texture [27].

If a cold deformed material gets annealed, the initial cold deformation texture will change during recrystallization and subsequent grain growth. Several parameters influence the recrystallization textures of fcc materials: The amount of preceding cold deformation, the starting texture and microstructure, the purity of the metal, the amount of grain growth overlapping with recrystallization, etc. [24]. Typical recrystallization texture component in aluminium alloys are usually Cube ({100}<001>) and Goss ({110}<001>), these texture components can be seen in the 111 pole figures shown in Fig. 2-19 d), and e), respectively [27]. The number of impurities and alloying elements affects the recrystallization texture of aluminium alloys. The alloy used in the present work is an AlMgSi alloy with a small amount of Fe). The Mg in the alloy will slow down the recovery during cold deformation and cause formation of shear bands. The recrystallization will then take place in these shear bands and orientations like Goss {011} <100>, P {011} <112> and Q {013} <231> will appear. The Fe and Si atoms will form precipitates that can complicate the texture evolution during recrystallization even further. If these particles are large enough (roughly above 1 μm) they can induce particle-stimulated nucleation (PSN), which have a tendency to weaken the recrystallization texture. This is because the grains that develop around the particles have a near random orientation. This PSN effect seems to be larger after short annealing time at high temperatures than after batch annealing (long anneal at moderate temperatures) [24]. Studies performed by Kuroda & Tverrgaard [27] have shown that Cube texture gives a lower

strength, but a high ductility and formability and that Cube texture can prevent shear band formation. While Goss texture on the other hand, can initiate the formation of shear bands [27].

2.3.3 Fe particles

All aluminium alloys will inevitably contain a certain amount of iron. Iron is always present as an impurity from bauxite, and due to the low solubility of iron in aluminium, most of the intermetallic particles that form in aluminium alloys contain Fe. This Fe content has a tendency to accumulate in the aluminium alloys with repeated recycling. There are many different intermetallic phases and particles that can form during the solidification of aluminium alloys. The formation of these intermetallic particles is dependent on factors like subtle changes in composition, cooling rate and grain refinement [6]. Some of these particles also form during the thermomechanical processing shown in Fig. 2-1.

Intermetallic particles of needle-like β-AlFeSi are formed at the grain boundaries and interdendritic regions during the casting of 6xxx aluminium alloys. These particles have poor cohesion to the surrounding Al matrix, which leads to poor ductility and formability. During homogenization these β particle will transform into smaller and rounder α-AlFeSi (α-AlFeMnSi) particles, which are more workable and lead to enhanced ductility and formability [28]. The particles (including Mg_2Si precipitates) in these alloys usually make up a large volume fraction (typically 1%) and their size is typically in the range of 1 to 10 μm. The most typical particles in the 6xxx alloys are the plate–like β-Al_5FeSi particles and rounded α-$Al_{12}(Mn,Fe)_3Si$ particles [29]. Research made by Couto et al. [28] on the second phase particles that form in 6xxx alloys after varies homogenization techniques revealed that Mg_2Si precipitates can be formed after homogenization if the material is air cooled. The Mg_2Si precipitates appear as dark spots in the BSE (backscattered electrons) images (see Fig. 2-20 a), while the AlFeSi particles appear bright in the BSE images (this is due to a difference in the mean atomic number, for further details see Section 2.5). However, their research also revealed that no Mg_2Si precipitates would form if the material were water quenched after homogenization (Fig. 2-20 b) [28].

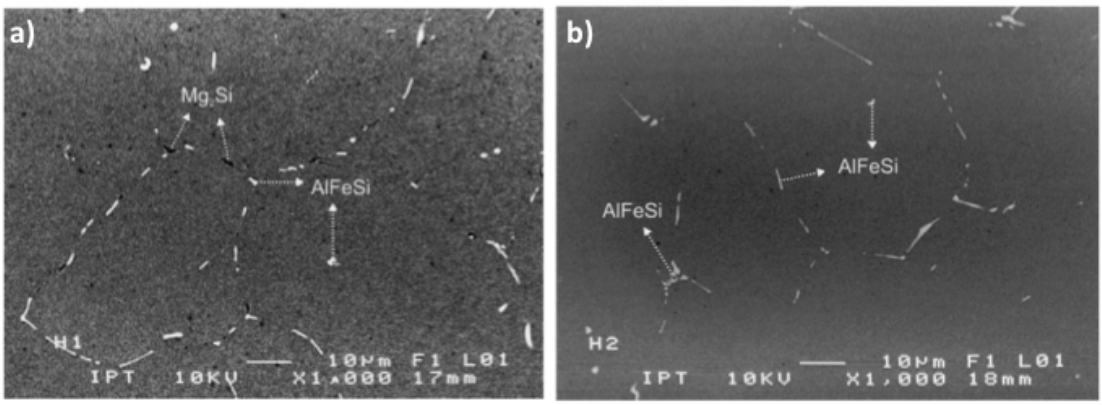

Fig. 2-20: BSE images (backscattered electrons) showing that Mg_2Si precipitates may form if the material is air cooled (a) after homogenization. No Mg_2Si precipitates will form if the material is water quenched (b) [28].

As already mentioned, the presence of iron particles in aluminium may lead to poorer mechanical properties, which in turn will lead to poorer compression properties. The Fe particles can also lead to pore formation and fracture initiation in the material. The three most common fracture mechanisms in metals are ductile fracture, cleavage fracture, and intergranular fracture. Aluminium is a very ductile metal, and the most relevant fracture mechanism for this work is ductile fracture.

As already mentioned, it is important for aluminium alloys used in car safety components to exhibit good formability. However, this formability is limited by ductile fracture [30]. A schematic illustration of the ductile fracture mechanisms is presented in Fig. 2-21. The figure illustrates ductile fracture where tensile stresses are applied, but the principle applies for compressive stresses as well. Ductile fracture initiates from pore formation around a second-phase particle or inclusion. The pores start to form when a sufficient amount of stress is applied to break the interfacial bounds between the particle and the ductile matrix, or to crack the particles. After the pores have started to form they will continue to grow and eventually coalesce if further plastic strain and hydrostatic stress are applied. The coalescent pores will sooner or later lead to ductile fracture in the material [31].

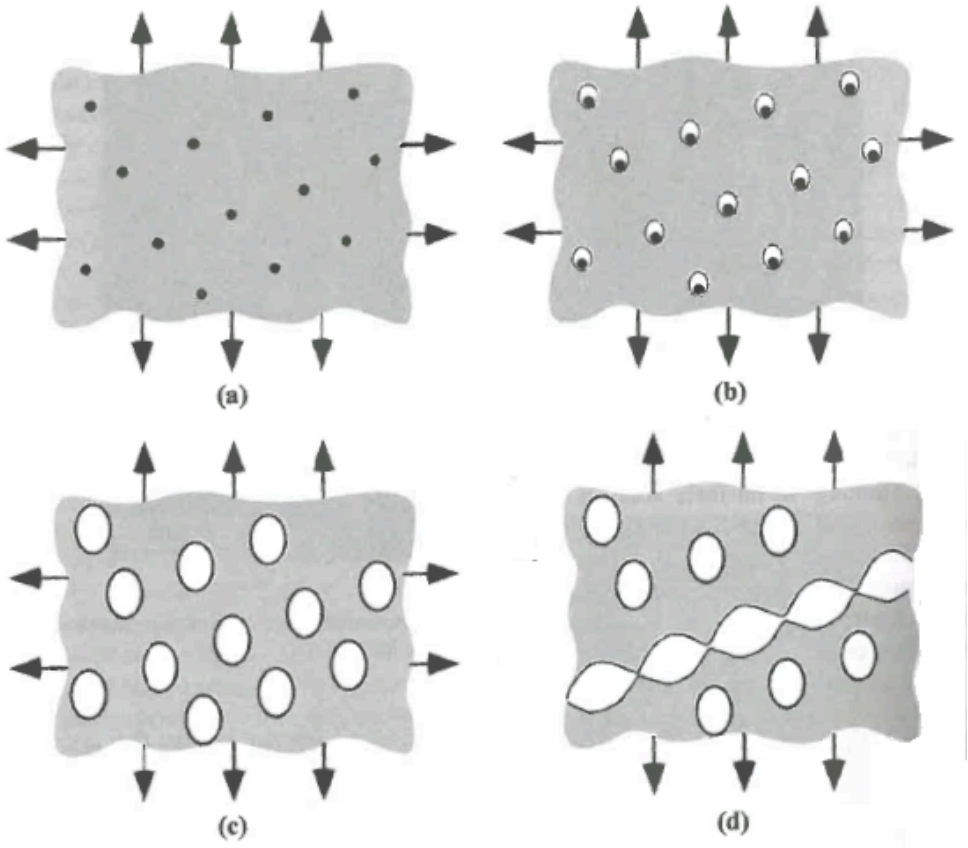

Fig. 2-21: Illustration of ductile fracture mechanism in metals: (a) inclusions/particles in a ductile matrix, (b) pore formation, (c) pore growth, (d) pore coalescence and fracture [31].

There exist many mathematical models for pore growth and coalesce. One of them is the Gurson-Tvergaard model, which is based on a model originally developed by Gurson and then later modified by Tvergaard. Pores influence the global flow behavior and through this influence they appear in the model indirectly. The pores effect is averaged through the material, which is assumed to be continuous and homogeneous. The Gurson-Tvergaard exhibits hydrostatic stress dependency, unlike the original Gurson model. The model also contains a failure criterion. It is assumed that ductile fracture occurs due to plastic instability, which produces a band of localized deformation. This kind of plastic instability will occur more easily in a Gurson-Tvergaard material (continuous and homogeneous) because of the strain softening induced by hydrostatic stress. The model is derived from a rigid-plastic analysis of a solid with a pore volume fraction f that are approximated by a homogeneous spherical body, which contains a spherical pore. The yield surface and flow potential g is given by [31].

$$g(\sigma_e, \sigma_m, \bar{\sigma}, f) = \left(\frac{\sigma_e}{\bar{\sigma}}\right)^2 + 2q_1 f cosh\left(\frac{3q_2\sigma_m}{2\bar{\sigma}}\right) - (1 + q_3 f^2) = 0 \qquad \text{(Eq. 3)}$$

where

$\sigma_e = macroscopic\ von\ Mises\ stress$
$\sigma_m = macroscopic\ mean\ stress$
$\bar{\sigma} = flow\ stress\ for\ the\ matrix\ material\ of\ the\ cell$
$f = current\ pore\ fraction$

Typical values used for metals are:

$q_1 = 1.5$
$q_2 = 1.0$
$q_3 = {q_1}^2$

The von Mises yield surface for an incompressible material is recovered by the setting $f = 0$ [31].

2.4 Compression

The aluminum alloys used as car safety components needs to exhibit good compression properties since they are meant to absorb the energy in a collision through compression deformation. If the compression properties are poor, the aluminium alloys will fracture much more easily, which compromises the deformability and the energy absorption capability.

2.4.1 Compression deformation

Different tests have been developed in order to investigate how different materials respond to compression deformations, and the upsetting test is one of them. The principle behind an upsetting test is described in the Experimental Setup chapter. A sample with very coarse grain structure that consist of very few and large grains will have a deformation behavior similar to single crystals during compression. The test samples will begin to contort, as the slip planes will start to rotate toward a position parallel to the compression plates. This is schematically illustrated in Fig. 2-22, which shows the compression of a single crystal. This “picture” can be transferred to and applies only to the samples with really coarse grain structure (few grains in relevant work piece), while this deformation behavior is not an issue for samples with a fine grain structure where the deformation behavior will be more complex, generally involving more slip systems. The amount of rotation increases as the compression deformation proceeds [32].

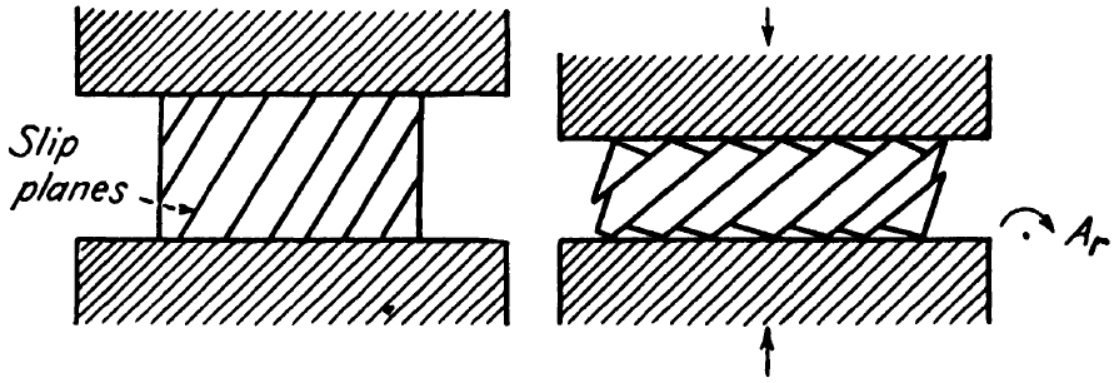

Fig. 2-22: Homogeneous lattice rotation in compression. Rotation is around axis Ar, and the slip plane approaches the compression plane [32].

2.4.2 Stress-strain response to compression

The force and displacement data that can be obtained from measurement at frequent intervals during the upsetting test can be used in calculations of stress and strain. The uniaxial compressive stress, *s* (engineering stress) is related to the deformation force *F* by [30]:

$$s = \frac{F}{A_0} \qquad \text{(Eq. 4)}$$

where A_0 is the initial area of the test specimens.

The engineering (nominal) strain *e* is defined as [30]:

$$e = \frac{\Delta L}{L_0} \qquad \text{(Eq. 5)}$$

where L_0 is the initial length of the test specimen. The engineering strain is what one obtains from a tension or compression test.

Once the engineering (nominal) strain is obtained, the true strain ε can be calculated according to [30]:

$$\varepsilon = \ln(1 + e) \qquad \text{(Eq. 6)}$$

The true stress σ can then be calculated by [30]:

$$\sigma = s(1 + e) \qquad \text{(Eq. 7)}$$

By plotting the true stress against the true strain one will get a stress-strain curve that is based on the continuous changes in dimensions during the

upsetting test, and that gives a true indication of the deformation characteristics of the actual aluminium alloy tested [10].

However, for complex deformations the true stress-strain curves can get noisy and irregular (wavy), and it is then convenient to use a generalized Voce fitting in order to smoothen the stress-strain curves.

First, the plastic strain needs to be calculated, this can be done by [30]:

$$\varepsilon_p = \varepsilon - (\frac{\sigma}{E}) \quad \text{(Eq. 8)}$$

where E is the Yong's Modulus. The value used for aluminium in this work is 35000 MPa, which was found by using the slope function in Excel.

The generalized Voce equation (with three terms) that can be used to conveniently describe the stress-strain curve is then given by [33]:

$$\sigma_v = \sigma_0 + Q_1\left(1 - exp\left(-C_1\varepsilon_p\right)\right) + Q_2\left(1 - exp\left(-C_2\varepsilon_p\right)\right) + Q_3\left(1 - exp\left(-C_3\varepsilon_p\right)\right)$$

(Eq. 9)

where σ_v is the calculated true stress from the plastic strain, and σ_0, Q_1, C_1, Q_2, C_2, Q_3, and C_3 are the work-hardening parameters, where $C = \frac{\theta}{\sigma_s}$ and Q= σ_s , where θ is the work-hardening rate and σ_s is the saturated stress. The interpretation of the generalized Voce equation is shown in Fig. 2-23. The figure only shows the generalized Voce equation with two terms, but the principle is the same for three terms [17]. The third term of the generalized Voce equation represent the stress-strain curve at maximum strength.

By plotting σ_v against ε_p a smoother adapted version of the stress-strain curves can be achieved.

In order to take a closer look at the stress-strain behavior the work-hardening rate θ can be plottet against the plastic strain in a modified Kocks-Mecking plot. The work-hardening rate θ can be found as [33]:

$$\theta = \frac{d\sigma_v}{d\varepsilon_p} = Q_1C_1exp\left(-C_1\varepsilon_p\right) + Q_2C_2exp\left(-C_2\varepsilon_p\right) + Q_3C_3exp\left(-C_3\varepsilon_p\right) \quad \text{(Eq. 10)}$$

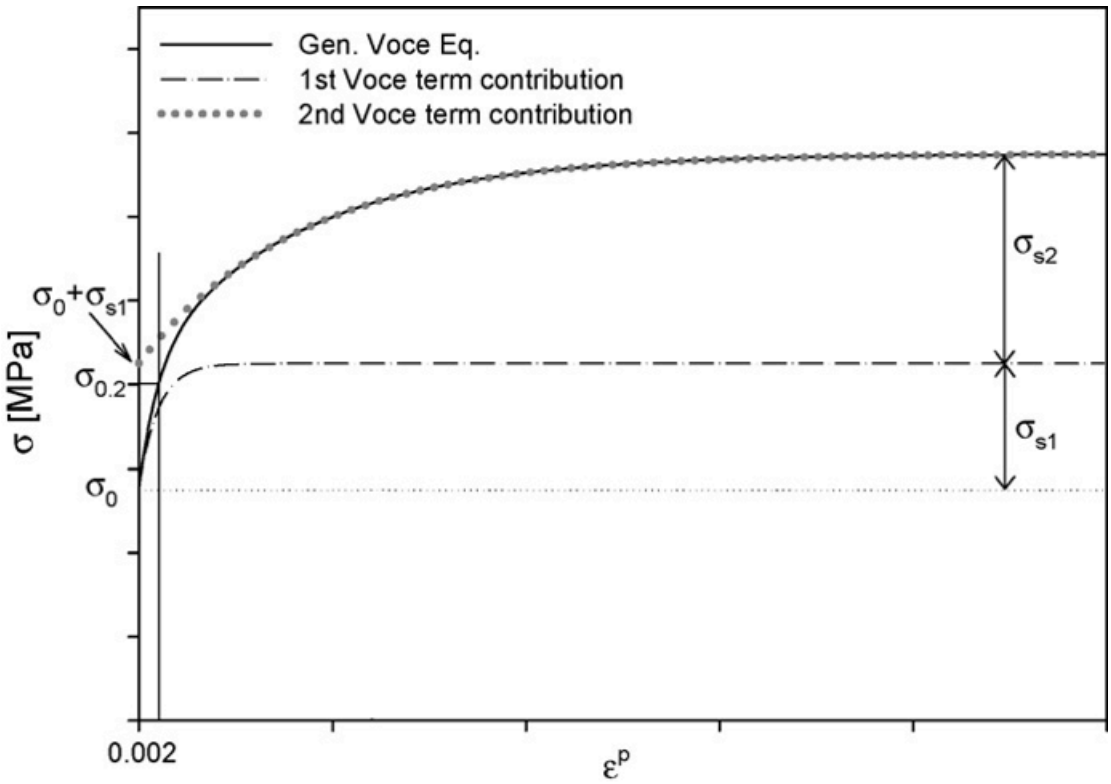

Fig. 2-23: The interpretation of the two terms in the generalized Voce equation[17].

2.5 Scanning Electron Microscopy (SEM)

As ductile fracture initiates from pore formation around inclusions or second-phase particles it is important to use an adequate instrument (e.g. scanning electron microscopy (SEM)) to analyze the particle structure to look for pore formation and to investigate possible fracture initiation. The SEM is a valuable instrument and is often used to characterize heterogeneous materials and microscale surfaces. [34]. Conventional SEMs have a typical resolution of 10 nm if an acceleration voltage of 1kV is applied. If an acceleration voltage of 20 kV is applied the resolution value is typical 3 nm. However, there are SEMs that have a better resolution than the conventional SEMs. The Field Emission SEM (FESEM) has a typical resolution of 2 nm and 1 nm if an acceleration voltage of 1 kV and 20 kV is applied, respectively. The main difference between a conventional SEM and a FESEM is the electron gun. The electron gun of a FESEM needs ultra high vacuum (typical 10^{-8} Pa) [35]. During a SEM analysis the area to be investigated is radiated with a focused electron beam, and when the electrons hit the specimen surface many different signals are created that can be detected in order to create images, e.g. secondary electrons (SE) and backscattered electrons (BSE). Fig 2-24 shows a schematic illustration of the different signals that can be detected in SEM. SE images are mainly created by topographic contrast, while BSE images can be created by the use of atomic number contrast (Z-contrast) or diffraction contrast [36]. BSE signals were used in the SEM analysis in the present work, and will be further described in the following section.

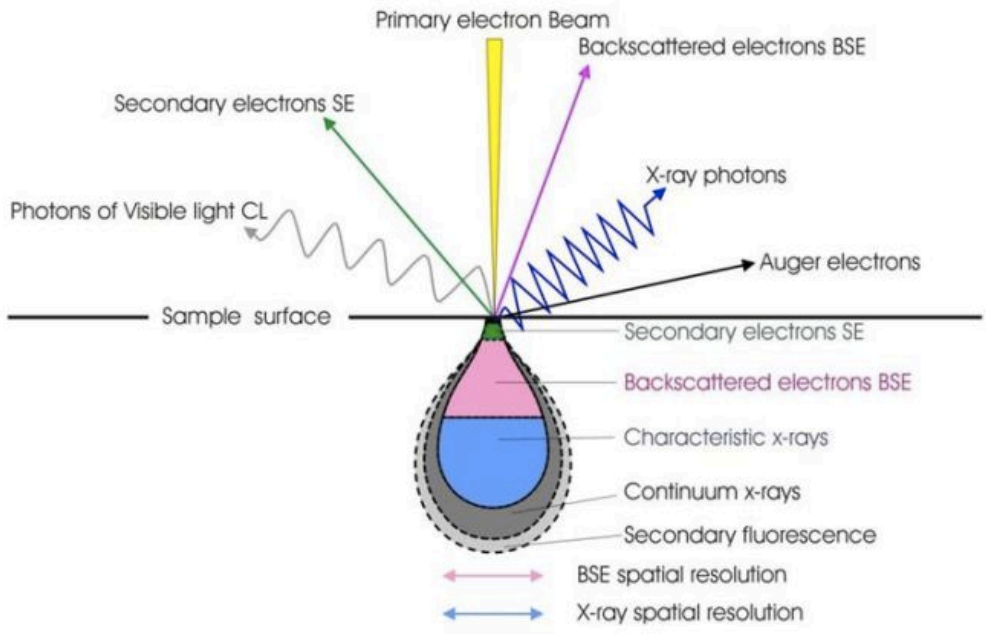

Fig. 2-24: Schematic illustration of the various signals that can be detected in SEM [37].

2.5.1 Backscattered Electrons (BSE)

The backscattered electrons (BSE) are the fraction electrons that gets reflected when the primary electrons hit the specimen surface. Backscattered electrons that hits the BSE detector produces a signal that eventually creates the image. The backscatter can happen by either single elastic scattering (scattering angle higher than 90°), where the primary electrons get reflected by the Coulomb field around the core, or by multiple elastic scattering, where the net directional change is big enough for the electrons to escape the sample. It is beneficial to use atomic number contrast (Z-contrast) when analyzing particles and pores. This is because the fraction of backscattered electrons increases with increasing atomic number. Phases with a high mean atomic number will appear brighter in a BSE image (since they reflect more electrons) than phases with low mean atomic number. This way it would be easy to detect iron particles in an aluminium alloy. The iron particles would appear bright on a darker aluminium matrix in a BSE image, while Mg_2Si particles again would appear darker than the matrix [36].

During a SEM analysis it is important to choose a right value of the acceleration voltage. It can be seen in Fig. 2-25 that the penetration depth of the electrons is bigger for a high acceleration voltage than for a low one. It is important that the voltage is not too low because then the penetration depth of the electrons would be too close to the specimen surface. It is also important to not choose a too high acceleration voltage, because then the penetration depth would be too great, and particles too deep into the specimen would be detected and give a somewhat false impression of the particle structure. A good value of the acceleration voltage during a BSE analysis is typically 10 kV [36].

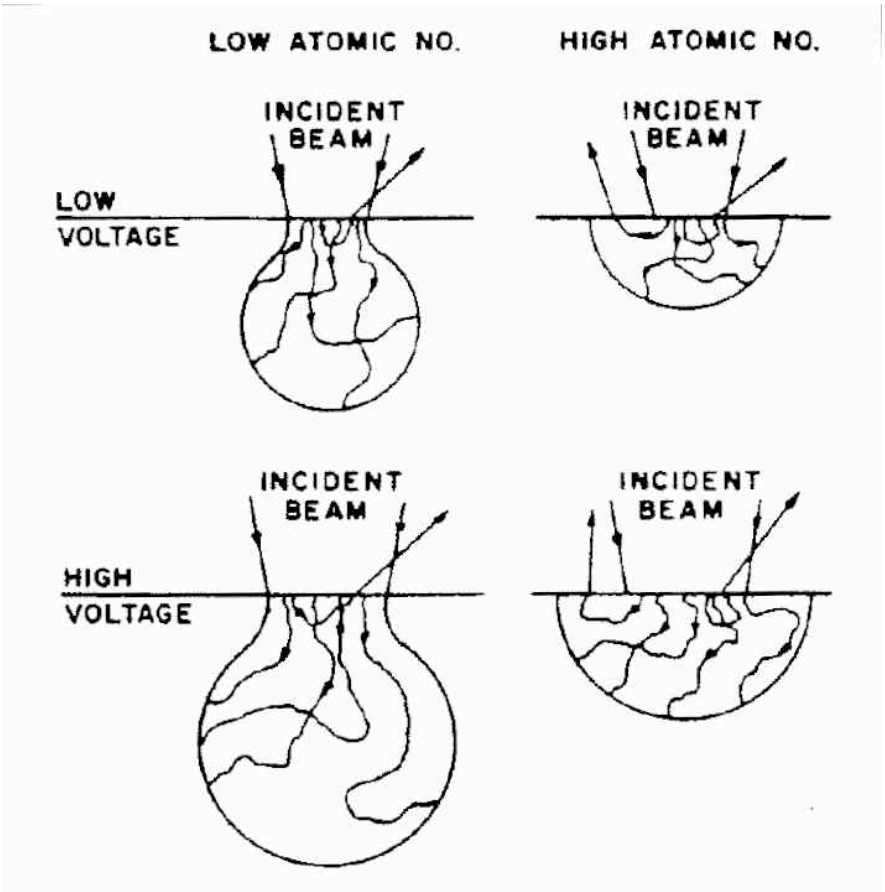

Fig. 2-25: The distribution of backscattered electrons [36].

3. Experimental Setup

3.1 Materials and Methods

The material used in this work was a 6xxx series AlMgSi alloy (Al-0.5Mg-0.4Si-0.2Fe). Three different conditions of the alloy were used; i) as-cast condition, ii) extruded condition, and iii) extruded, cold-rolled and recrystallized condition. The different conditions were heat-treated to three different tempers (under-aged temper, peak-aged temper, and over-aged temper) before the thermomechancal properties were investigated during compression in an upsetting test. The microstructures of the different conditions in different tempers were characterized prior to the upsetting testing, including an extruded and cold-rolled condition (not used further in the upsetting test). This additional condition was only included in the characterization in order to observe the microstructural changes the alloy undergoes during mechanical processing.

The as-cast condition was provided in the form of a billet material and has been homogenized prior to this work. The homogenization process can be seen in Fig. 3-1. The soak temperature of the homogenization was 600°C, with a heating rate of 100°C/h to this temperature. The soak time was 2.5 hours, followed by cooling down to ambient temperatures with a cooling rate of 300°C/h. Even though the as-cast condition has been homogenized it is called the as-cast condition in this report.

The extruded condition was provided as two different profiles with different dimensions. The first profile (10 mm x 50 mm) was used as the extruded condition, while the second profile (20 mm x 50 mm) was further processed and eventually used as both the extruded and cold-rolled condition and the extruded, cold-rolled and recrystallized condition. The recrystallization of the material is done in order to randomize the crystallographic texture which is introduced during extrusion and cold-rolling. This will remove some of the excess energy in the material introduced during previous processing. The further processing of this extruded profile (20 mm x 50 mm) will be described in section 3.1.2 and section 3.1.3.

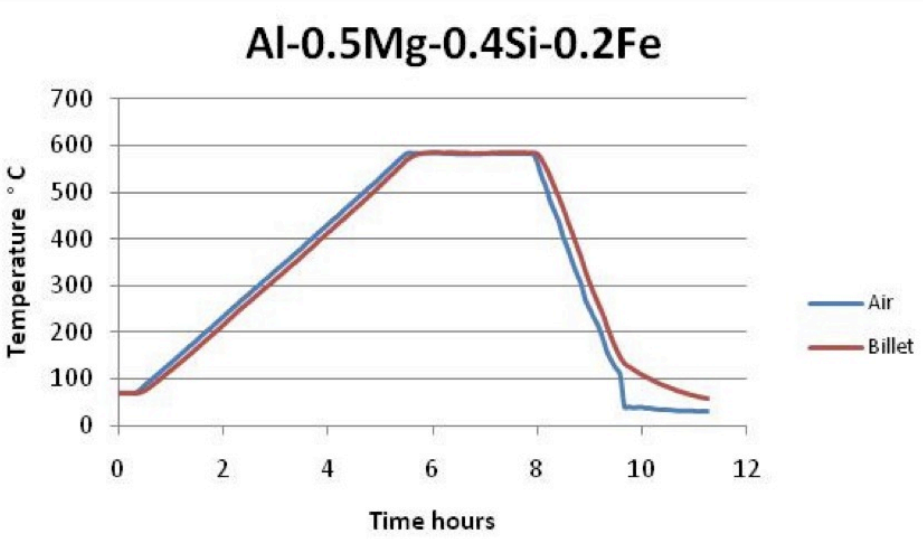

Fig. 3-1: The homogenization procedure for AlMgSi. The soak temperature is 600°C, with a heating rate of 100°C/h. The soak time is 2.5 hours, with the cooling rate of 300°C/h.

3.1.1 Cold-rolling

The second of the extruded profiles (20 mm x 50 mm) was further processed by cold-rolling, but first it was heat-treated at 540°C for 30 minutes in order to dissolve AlMgSi particles that have been formed initially to avoid cracking during the cold-rolling. The cold-rolling was done by cross-rolling with a two-high pullover laboratory rolling mill. The profile was first rolled on one side, then turned 90° and rolled on the other side. The rolling was performed on both sides (every other rolling step) until the dimensions of 12 mm x 12 mm were reached, which corresponds to a strain of 0.86. The profile was water cooled between each rolling step. Some of the cold-rolled material was used as the extruded and cold-rolled condition in order to characterize microstructural changes during mechanical processing. However, this condition was not used in the upsetting test. The rest of the cold-rolled material was further processed by heat-treatment and recrystallization in order to be used as the extruded, cold-rolled and recrystallized condition in the upsetting test.

3.1.2 Vickers hardness testing and age hardening curves

A preliminary study was performed on the extruded condition before the actual heat-treatment of the materials prior to the mechanical testing. This was done in order to select the appropriate heating time and temperature. Some test samples where made from the first extruded profile (10 mm x 50 mm) and heated-treated at 540°C in a salt bath for 30 minutes. Then they were quenched and held at ambient temperatures for 24 hours before being heat-treated again at 175°C

in an oil bath for 100, 1 000, 5 000, 10 000, 25 000, 100 000 and 1 000 000 seconds. The hardness of each of the heat-treated samples was measured with a Vickers hardness test (HV1) as an average of five indentations. The mean hardness (the average of 5 measurements) was plotted against the heating time in an age hardening curve. Based on this age hardening curve (see chapter 4. Results) the ageing time for under-aged temper (2 hours), peak-aged temper (8 hours), and over-aged temper (11 days) were selected.

3.1.3 Heat-treatment

All the conditions were heat-treated to three different tempers; under-aged temper, peak-aged temper, and over-aged temper. First, the conditions were solution heat treated at 540°C in a salt bath for 30 minutes, except for the extruded, cold-rolled and recrystallized condition, which was heat-treated (annealed and recrystallized) at 520°C for 10 minutes. The lower temperature was to ensure that the recrystallized grains would not grow to abnormal size. All the conditions were quenched after the first heat-treatment, and held at ambient temperatures for 24 hours. Then they were artificially aged at 175°C in an oil bath for 2 hours (under-aged temper), 8 hours (peak-aged temper), and 11 days (over-aged temper).

3.2 Characterization of initial materials

3.2.1 Texture

A determination of the texture was made for the extruded condition, the extruded and cold-rolled condition, and the extruded, cold-rolled and recrystallized condition. The texture of a material is of importance because it can cause directionality (anisotropy) in the mechanical properties. The texture determination was done by the use of a texture goniometer, and the texture was later characterized by stereographic projection in the form of 111 pole figures and ODFs. A schematic sketch of a texture goniometer can be seen in Fig. 3-2. The sample to be investigated gets hit by an X-ray beam, which gives four reflections and four pole figures, which in turn are used to calculate the corresponding ODFs. Before the texture determination the samples had to be prepared first. Their size had to be cut down to fit the dimensions shown in Fig. 3-3 (22mm x 14 mm). Then they were ground down to 1200/2400 mesh, before being etched. The samples where first etched in Alubeis (10-20% NaOH + 1 teaspoon sugar per liter fluid), whereafter they were shortly dipped in water before being further etched in 20-30% HNO_3 for about 20-30 seconds.

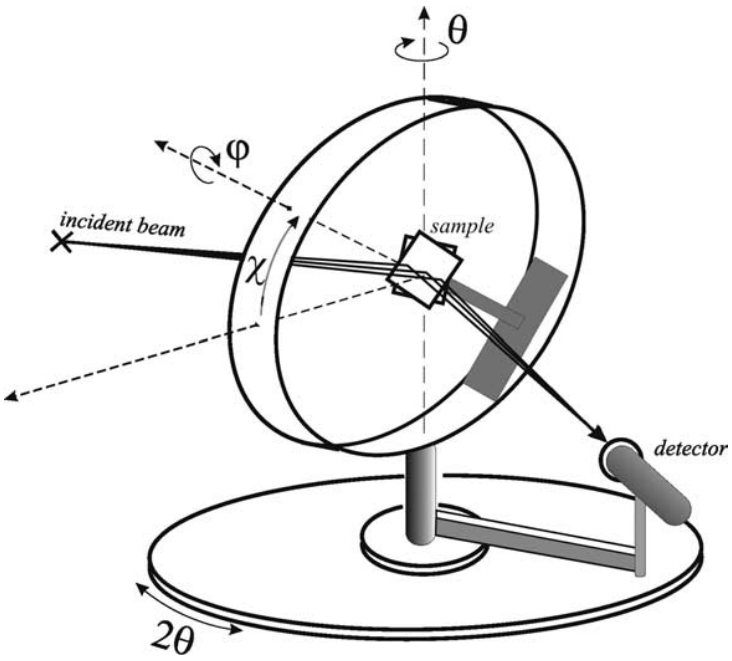

Fig. 3-2: Schematical sketch of a texture goniometer. χ, φ, θ are the different goniometer angles.

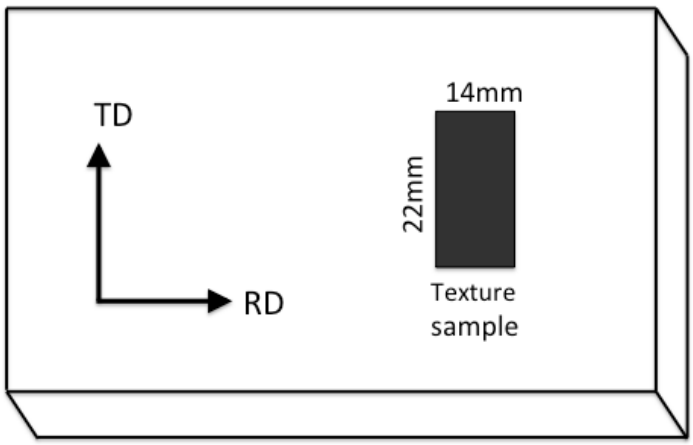

Fig. 3-3: the geometry for a standard texture sample.

3.2.2 Optical microscopy (OM)

The initial microstructure (both grain and particle structure) of the different conditions (including the extruded and cold-rolled condition) was characterized with optical microscopy. Before the characterization the materials were prepared by manually grinding with P80, P320, P500, P1200, and P2400 grinding paper before being mechanically polished with 6 µm, 3 µm, and 1µm polishing plates. Since the Fe particles is much harder than the ductile Al-matrix the samples had to be chemically polished using a 10% OP-S solution for 1 minutes and then pure H_2O for 30 seconds. This was i to get rid of "comet tails" created by the particles

The initial particle structure was then characterized with an optical microscope, a Zeiss instrument was used for the as-cast condition and a Leica MEF4M instrument was used for the other conditions. In order to see the initial grain structure the samples had to be anodized using a 5% HBF_4 aqueous solution for 90 seconds. A sub-parallel λ-plate, which gives polarized, light had to be used in order to obtain contrast between the different grains in the microstructure.

3.3.2 Scanning Electron Microscopy (SEM)

The microstructure of the samples was also characterized by the use of Scanning Electron Microscopy (SEM) in order to take an even closer look at the constituent particles in the materials. However, before the samples could be analysed with SEM, further preparations had to be done.

SEM Preparations/ion milling

After the OP-S polishing that was used to prepare the samples for the optical microscopy analysis, the samples were further prepared for SEM-analysis by using ion milling for 20 minutes. The ion milling process uses submicron ions that are accelerated and bombarded onto the surface of the samples while they are mounted on a rotating table inside a vacuum chamber. This is done in order to remove some of the surface and possible defects on it. The ion milling instrument used in the present work was an IM-3000 and a picture of it can be seen in Fig. 3-4. The ion milling was performed with a tilting angle of 75-80° and with an acceleration voltage of 4 kV.

Backscattered Electrons (BSE)

In order to get a more detailed image of the particles and their size and distribution, detection of backscattered electron (BSE) was used for the SEM-analysis. The SEM instrument used in the present work was a Field Emission (FE) Hitachi SU6600 SEM, and pictures of it can be seen in Fig. 3-5. An acceleration voltage V_{acc} of 10.0 kV and a working distance between 9.2-17.4 mm were used during the characterization. The Fe particles will appear bright on a darker aluminium matrix in the BSE images, since the Fe aparticles has a higher mean atomic number than the Al matrix and they will therefore generate more backscattered electrons.

Fig. 3-4: The ion milling instrument used in the present work, an IM-3000.

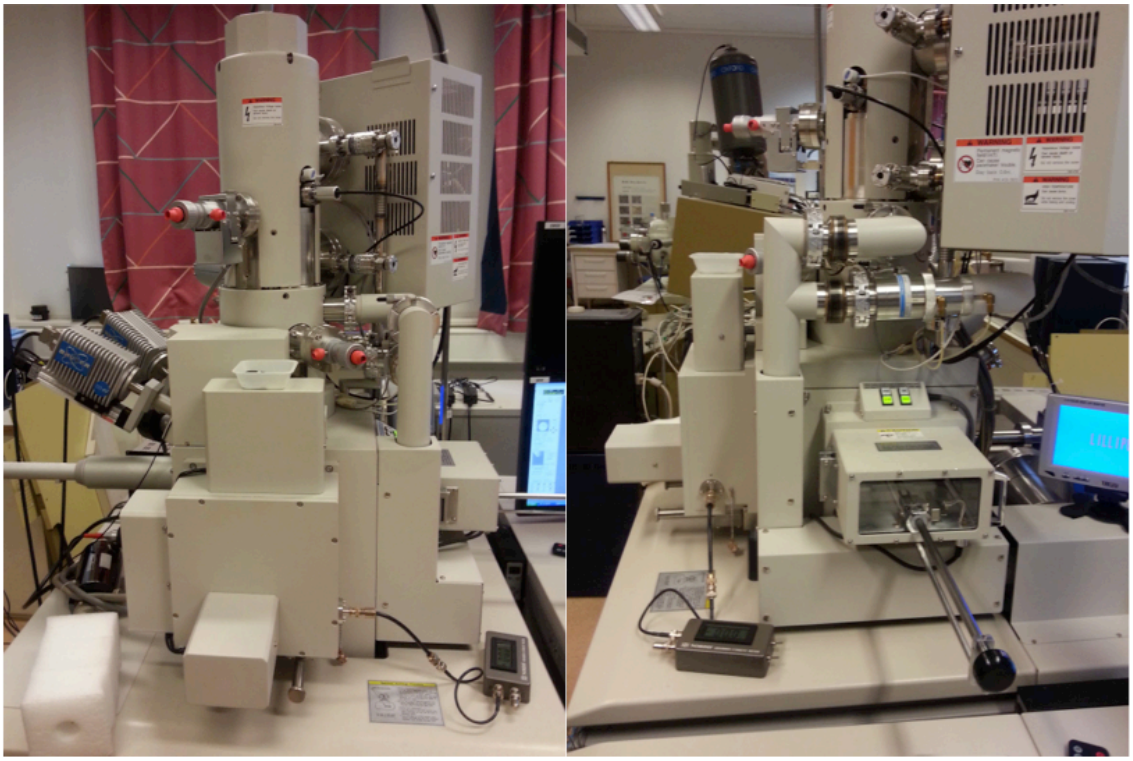

Fig. 3-5: The SEM instrument used in the present work, a Field Emission (FE) Hitachi SU6600 SEM.

3.3 Upsetting testing

In order to look at the mechanical properties and the deformation behavior during compression the different conditions in all tempers were tested with an upsetting test. There were three parallels of each condition/temper, which made a total of 27 test samples. The sample annotation and the corresponding conditions and tempers for the materials used in the upsetting test are presented in Table 2-1. The first number in the sample designation indicates the condition of the sample; 1, 2, and 3 indicate the as-cast condition, the extruded condition, and the extruded, cold-rolled and recrystallized condition, respectively. The letter indicates which temper the materials have been heat-treated to; U, P, and O indicate the under-aged temper, peak-aged temper, and over-aged temper, respectively. The last designation number indicates which parallel it is.

Test samples were made of the different conditions in the form of cylindrical pieces with the dimensions of 9 mm in diameter and 13.5 mm in height. These were made at the mechanical workshop at NTNU. A simplified sketch showing the principle behind an upsetting test can be seen in Fig. 3-6. Compressive force is applied in order to deform the cylindrical test pieces to produce cylinders with smaller height and larger diameter. It was very important to take accurate measurements of height and diameter of the samples prior to the testing, since an extensometer was used to measure the displacement of the test pieces during the compression. The samples were compressed to a predetermined strain, about $\varepsilon \sim 0.7$. The upsetting test was run with an initial strain rate of 0.002 s^{-1}. Carbon pasta was used as a lubricant to reduce the friction between the test pieces and the compression blocks in order to avoid barreling. The data gathered from the upsetting test were used to determine the stress-strain response of the different conditions/tempers. The machine used for the testing was an Instron 8032 (Fig. 3-7), and a camera setup was used to record test images every 10 seconds in order to document the deformation behavior of the different samples.

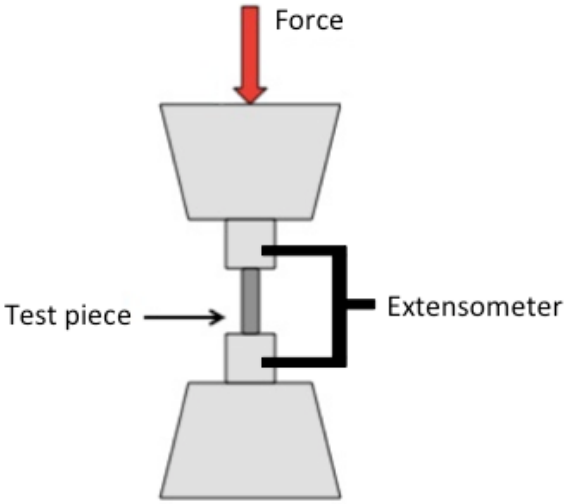

Fig. 3-6: Simplified sketch showing the principle behind an upsetting test.

Fig. 3-7: The machine used for the upsetting testing, an Instron 8032. A camera setup was used to record test images every 10 seconds, and an extensiometer was used to measure the displacement during the compression.

Table 2-1: AlMgSi samples used in the upsetting test and the corresponding conditions and tempers.

Sample	Condition	Temper
1U-1	As cast	Under aged
1U-2	As cast	Under aged
1U-3	As cast	Under aged
2U-1	Extruded	Under aged
2U-2	Extruded	Under aged
2U-3	Extruded	Under aged
3U-1	Extr./cold-rolled/recr.	Under aged
3U-2	Extr./cold-rolled/recr.	Under aged
3U-3	Extr./cold-rolled/recr.	Under aged
1P-1	As cast	Peak
1P-2	As cast	Peak
1P-3	As cast	Peak
2P-1	Extruded	Peak
2P-2	Extruded	Peak
2P-3	Extruded	Peak
3P-1	Extr./cold-rolled/recr.	Peak
3P-2	Extr./cold-rolled/recr.	Peak
3P-3	Extr./cold-rolled/recr.	Peak
1O-1	As cast	Over aged
1O-2	As cast	Over aged
1O-3	As cast	Over aged
2O-1	Extruded	Over aged
2O-2	Extruded	Over aged
2O-3	Extruded	Over aged
3O-1	Extr./cold-rolled/recr.	Over aged
3O-2	Extr./cold-rolled/recr.	Over aged
3O-3	Extr./cold-rolled/recr.	Over aged

3.4 Characterization of compressed samples

The microstructure of the different conditions was characterized after the upsetting test in order to look at the microstructural changes due to the compression deformations and to look for pore formation and possible fracture initiation. Only the microstructure of the conditions (all three) in over-aged temper was characterized after compression. The same preparations and methods used for the characterization of the initial conditions were used on the compressed ones. The compressed test pieces of the over aged conditions were cut in half in order to look at the microstructures in the cross-sections normal to the compression axis. Furthermore, the pieces needed to get molded before the

preparation (mechanical grinding and polishing), and since the molding material was a non-conducting material the samples needed to be coated with carbon before the SEM analysis in order to avoid charging during the analysis. The same SEM BSE analysis that was used on the initial microstructures was used again on the compressed microstructure order to look at the particle structure and to look for possible pore formation.

4. Results

4.1 Initial Microstructure

The results from the characterization of the initial microstructure of the different conditions (including the extruded and cold-rolled condition) are presented in the next sections. It is important to study the initial microstructure of the different conditions in order to understand the microstructural changes the AlMgSi undergoes during the different thermomechanical processing steps (extrusion, cold-rolling, heat-treatment), and this is also the reason why the initial microstructure of the extruded and cold-rolled condition is included in the characterization.

4.1.1 Grain structure

The initial grain structure of the different conditions can be seen in Fig. 4-1. The grain structure of as-cast condition (Fig. 4-1 a) consists of many equiaxed grains in medium size (~70-80 μm). The grains in the extruded condition (Fig. 4-1 b) are also fairly equiaxed but larger in size (~120 μm). This is a recrystallized grain structure, which means that a spontaneous recrystallization has occurred at the end of the extrusion die. The extrusion direction (ED) and the direction normal (ND) to the extrusion direction are indicated with arrows in the image. The rolling direction (RD) is also indicated with arrows in Fig. 4-1 c) and d) for the extruded and cold-rolled condition and the extruded, cold-rolled and recrystallized condition, respectively. From Fig. 4-1 c) it can be seen that the grains in the extruded and cold-rolled condition have a clear deformation structure, the grains have been elongated in the rolling direction. The extruded, cold-rolled and recrystallized condition in Fig. 4-1 d) has a recrystallized grain structure that consists of many medium sized (~50-60 μm) equiaxed grains.

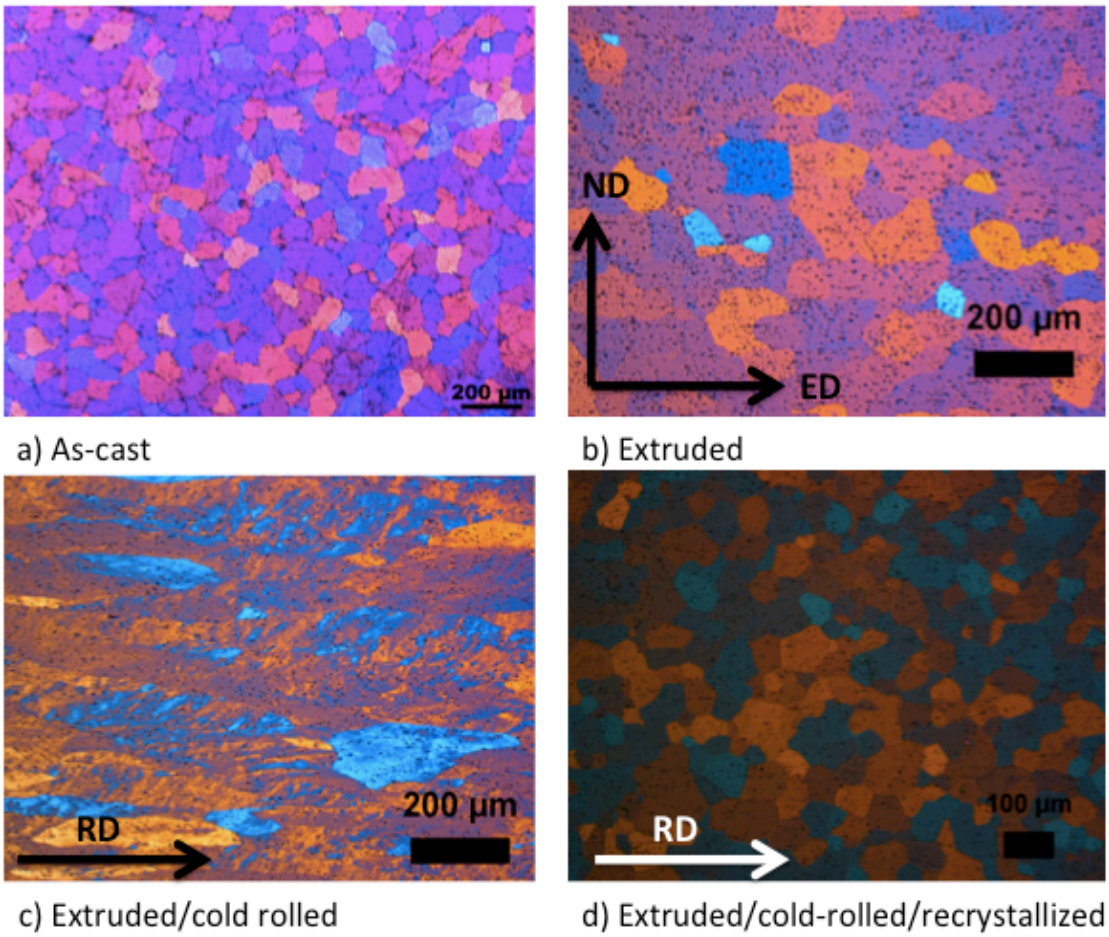

Fig. 4-1: Images of the initial grain structures of AlMgSi in different conditions: a) As-cast, b) Extruded, c) Extruded/cold-rolled, d) Extruded/cold-rolled/recrystallized. The extrusion (ED) and rolling direction (RD) is implied with arrows, so is the direction normal to the extrusion direction (ND).

4.1.2 Particle structure

The initial particle structure of the different conditions (including the extruded and cold-rolled condition) is shown in Fig. 4-2 and Fig. 4-3, which show optical micrographs and SEM BSE images, respectively. The initial particle structure in the as cast condition, as seen in Fig 4-2 a), consists of relatively few particles. These particles vary a lot in both size and shape. Some of them are small and spherical, while others are larger and more irregular in shape. From the BSE image in Fig. 4-3 a), it can also be seen that these particles are mainly located at grain boundaries. A few coarse Mg_2Si precipitates may also be seen these are indicated with red arrows in the image. Both Fig. 4-2 b) and Fig. 4-3 b) show images of the initial particle structure of the extruded condition. The direction of the extrusion (ED) and the direction normal to it (ND) are indicated in the images. Some of the particles are spherical, while others are more plate-like. The particles seem to be both oriented and aligned in the direction of the extrusion.

Images of the initial particle structure of the extruded and cold-rolled condition can be seen in Fig. 4-2 c) and Fig. 4-3 c). The particle structure consists of many particles that are inhomogeneously distributed and that vary some in both shape and size. A randomization of the particle structure has taken place, and the particles do not seem to be oriented or aligned in a preferred direction anymore (as compared to the extruded condition). The initial particle structure of the extruded, cold-rolled and recrystallized condition can be seen in Fig. 4-2 d) and Fig.4-3 d). The particles in this condition seem to be somewhat smaller than the particles in the other conditions. The particles are inhomogeneously distributed and seem to be mostly small and spherical, i.e. they do not vary much in size and shape. A few Mg_2Si precipitates can also bee spotted in particle structure (Fig. 4-3 d) these are indicated with red arrows in the image.

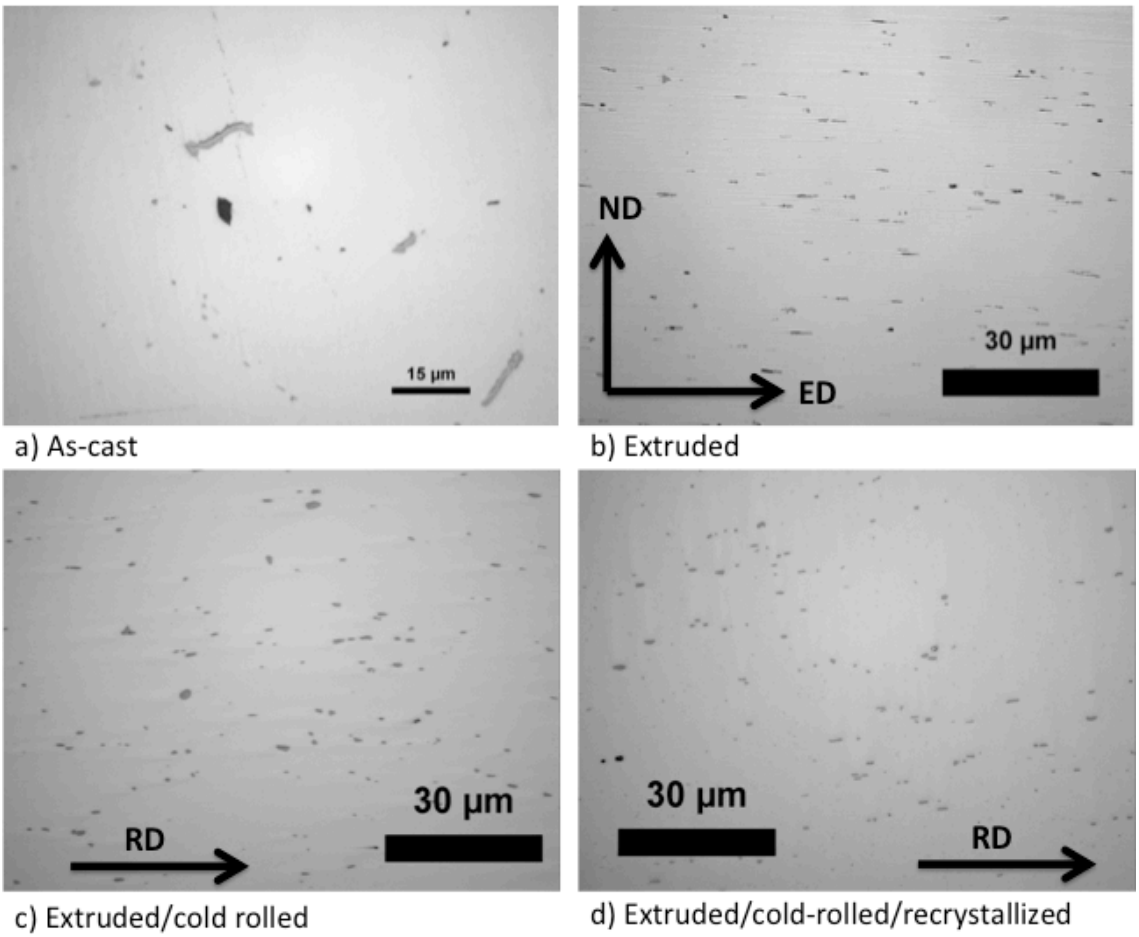

Fig. 4-2: Optical micrographs showing the initial particle structure of AlMgSi in four different conditions: a) As cast, b) Extruded, c) Extruded and cold rolled, d) Extruded, cold-rolled and recrystallized. The extrusion direction (ED), the direction normal to it (ND), and the rolling direction (RD) are indicated with arrows in the micrographs.

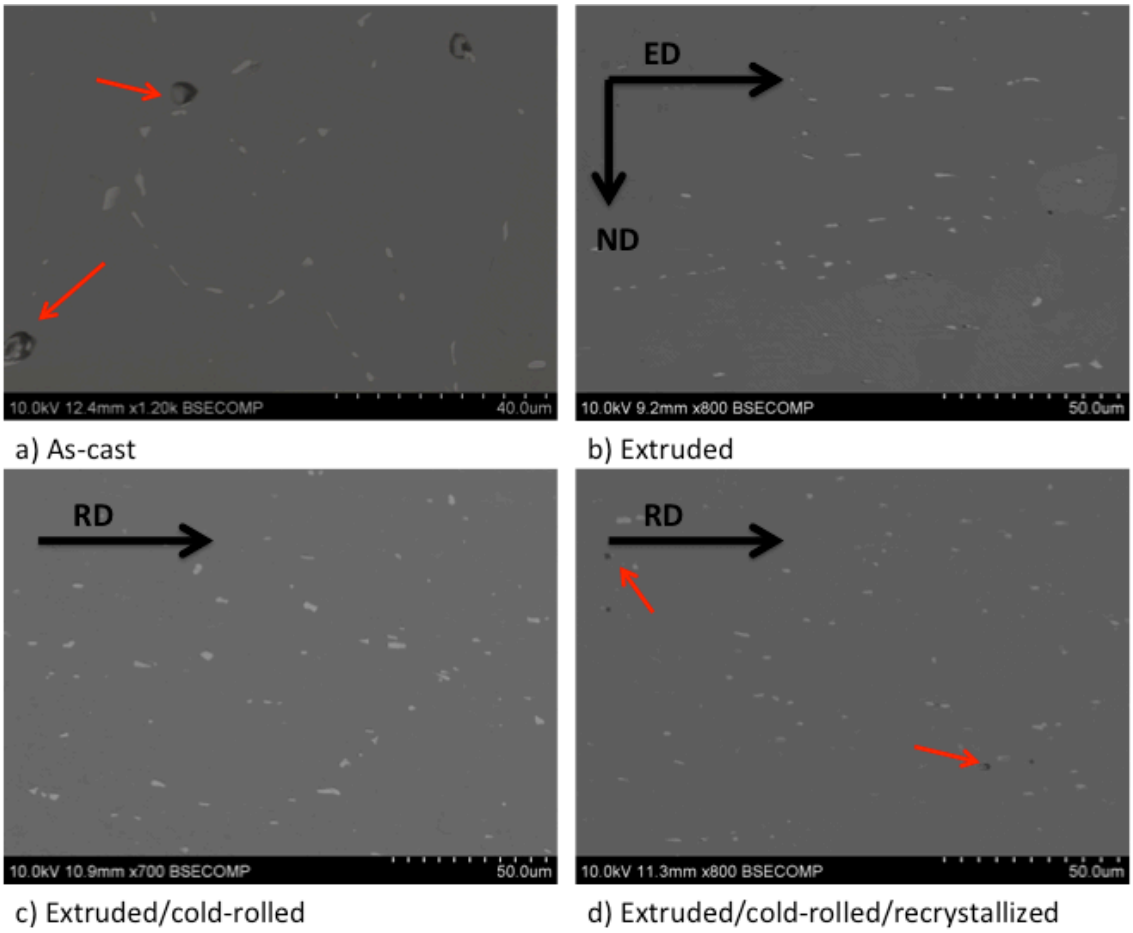

Fig. 4-3: SEM BSE micrographs of AlMgSi in different conditions: a) As cast, b) Extruded, c) Extruded and cold rolled, d) Extruded, cold-rolled and recrystallized. The extrusion direction (ED), the direction normal to it (ND), and the rolling direction (RD) are indicated with arrows in the micrographs.

4.2 Texture

Stereographic projections of the texture of the extruded condition can be seen in the form of 111 pole figures and an ODF in Fig. 4-4. From the pole figures and the ODF it can be seen that the extruded condition exhibit a texture that is dominated by Cube texture. However, a little Goss texture can also be seen. Both the Cube and the Goss texture are typical recrystallization textures in aluminium alloys. The texture of the extruded and cold-rolled condition can be seen in Fig. 4-5, which shows 111 pole figures and the corresponding ODF. Both the 111 pole figures and the ODF show that the extruded and cold-rolled condition has a very weak (deformation) texture. Fig. 4-6 shows 111 pole figures and the corresponding ODF of the texture of the extruded, cold-rolled and recrystallized condition. The texture of this condition is also very weak and the texture pattern in both the pole figures and the ODF shows that this condition exhibits a texture that is close to random.

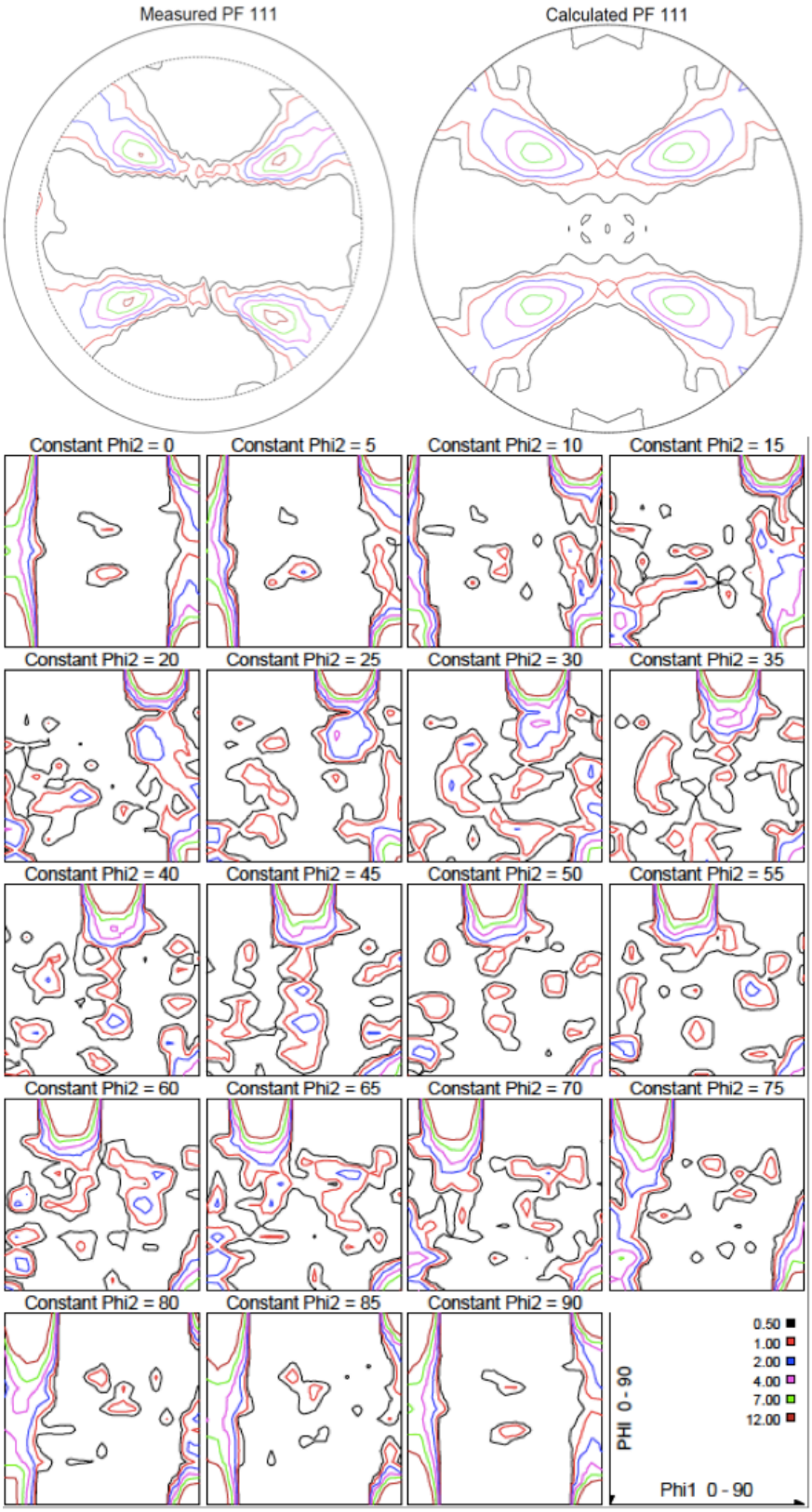

Fig. 4-4: Texture of AlMgSi in extruded condition; cube texture

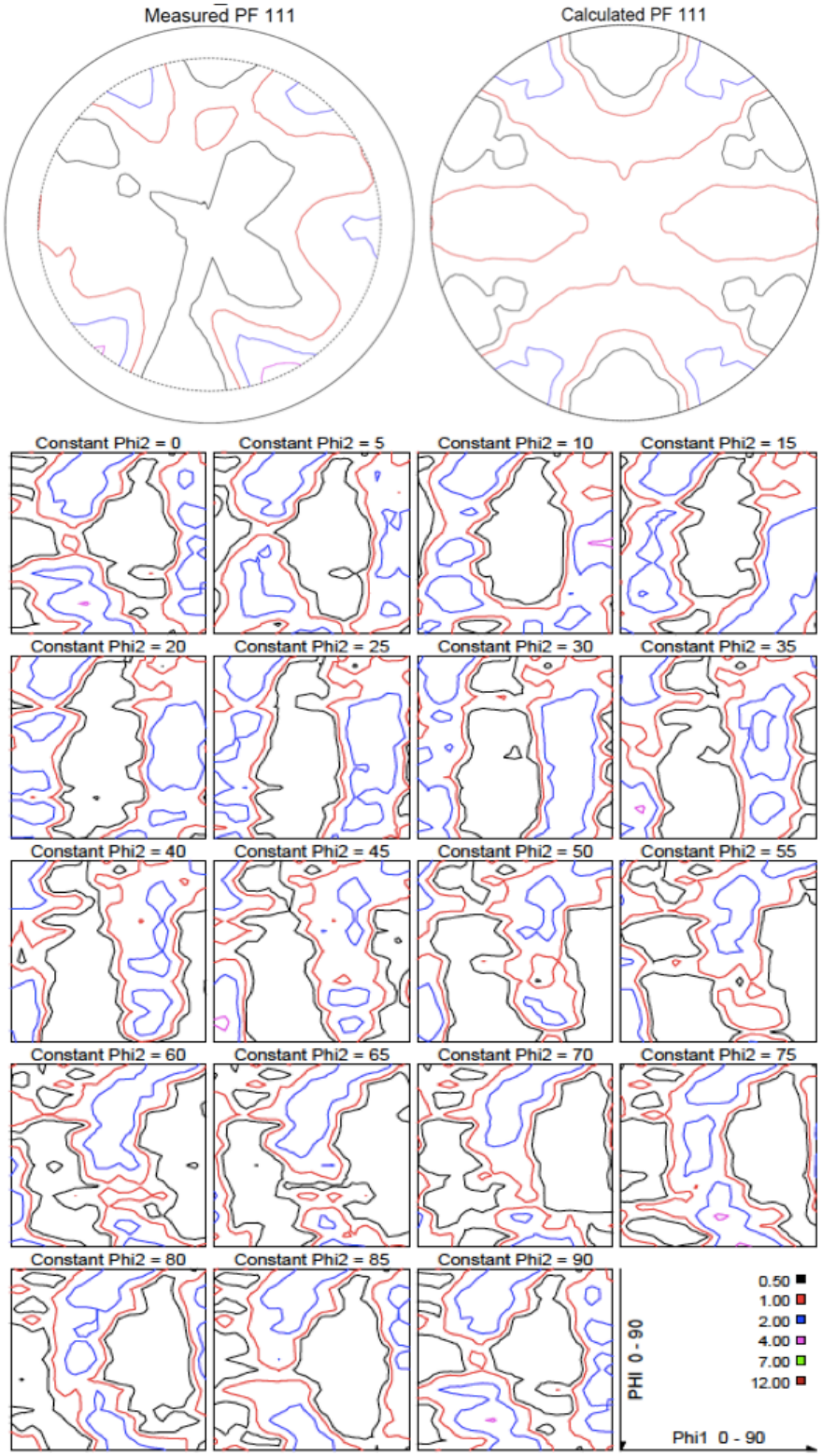

Fig. 4-5: Texture of AlMgSi in extruded and cold rolled condition; weak deformation texture.

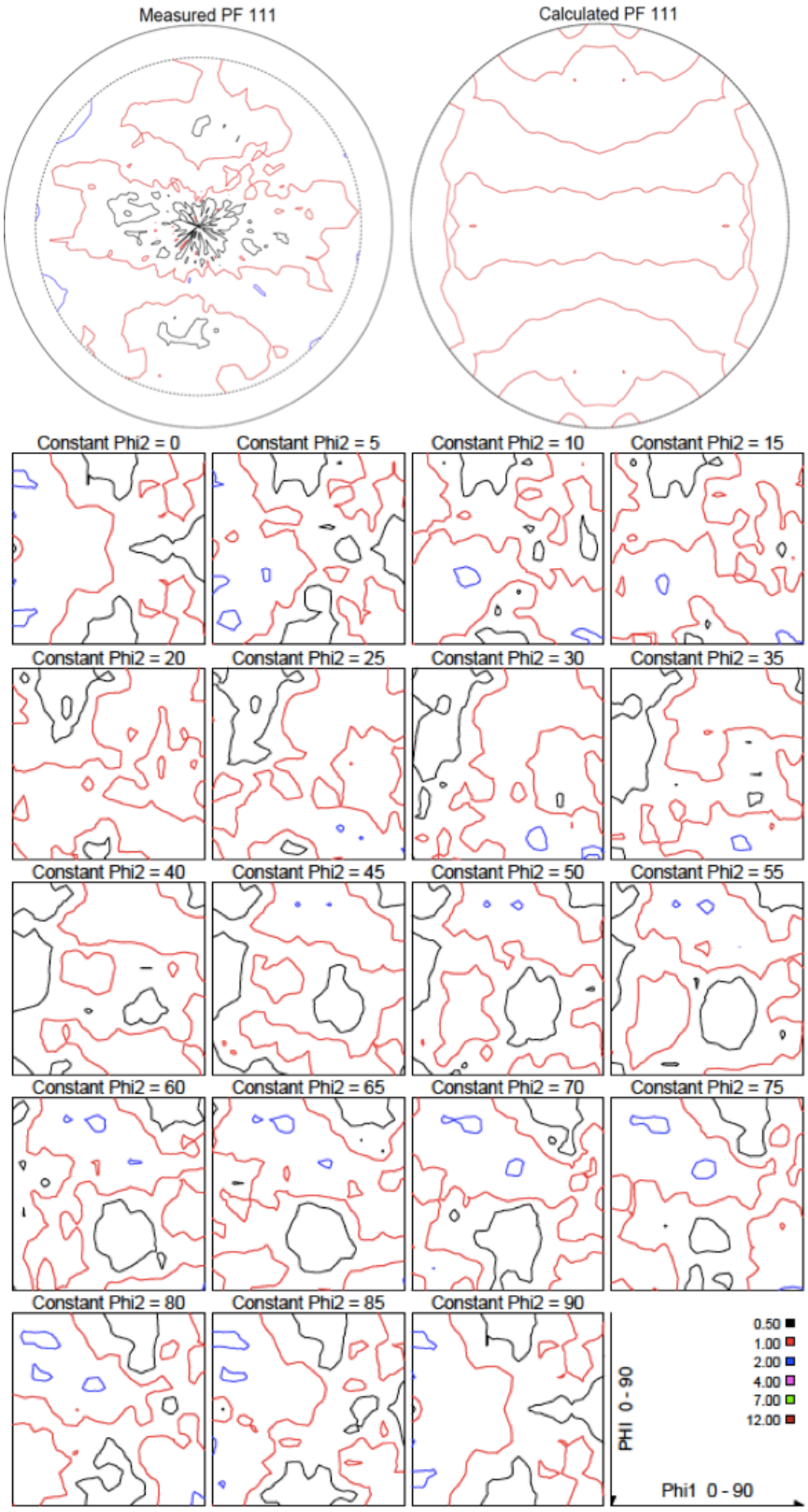

Fig. 4-6: Texture of AlMgSi in extruded, cold rolled and recrystallized condition; close to random texture.

4.3 Age hardening curves

The results from the preliminary study performed before the actual heat-treatment prior to the mechanical testing can be seen in Table 4-1 and Fig. 4-7. The Vickers hardness testing (HV1) of the extruded condition for various age hardening times when heated to 175°C are compiled in Table 4-1. These results are also presented in Fig. 4-7, where the mean hardness (the average of 5 measurements) is plotted against the ageing time. It can be seen that the Vickers hardness generally increases with increasing ageing time until it reaches its peak at about 90 000 seconds (about 25 hours). After that, the Vickers hardness starts to decrease with increasing ageing time. The ageing times that were chosen for the under-aged temper, the peak-aged temper, and the over-aged temper are 2 hours, 8 hours, and 11 days, respectively. The chosen ageing time for the different tempers are marked in Fig. 4-7. It should be noted that the ageing time chosen for the peak-aged temper do not correspond to the peak hardness shown in Fig. 4-7. The conditions heat-treated to peak-aged temper will in reality be slightly under-aged. However, the conditions that are heat-treated for 8 hours are named as peak-aged in this report. It should also be noted that the ageing curve shown in Fig. 4-7 only shows the ageing sequence for the extruded condition. The same ageing behavior is assumed for all conditions and therefor used for all the samples.

Table 4-1: Results form the Vickers hardness testing (HV1)

Ageing time (s)	1 (HV)	2 (HV)	3 (HV)	4 (HV)	5 (HV)	Average (HV)
100	49	51	50	51	51	50.4
1000	59	63	59	60	60	60.2
5000	61	59	56	55	58	57.8
10 000	67	68	68	70	70	68.6
25 000	82	85	83	85	87	84.4
100 000	101	103	99	100	98	100.2
1000 000	78	78	80	81	76	78.6

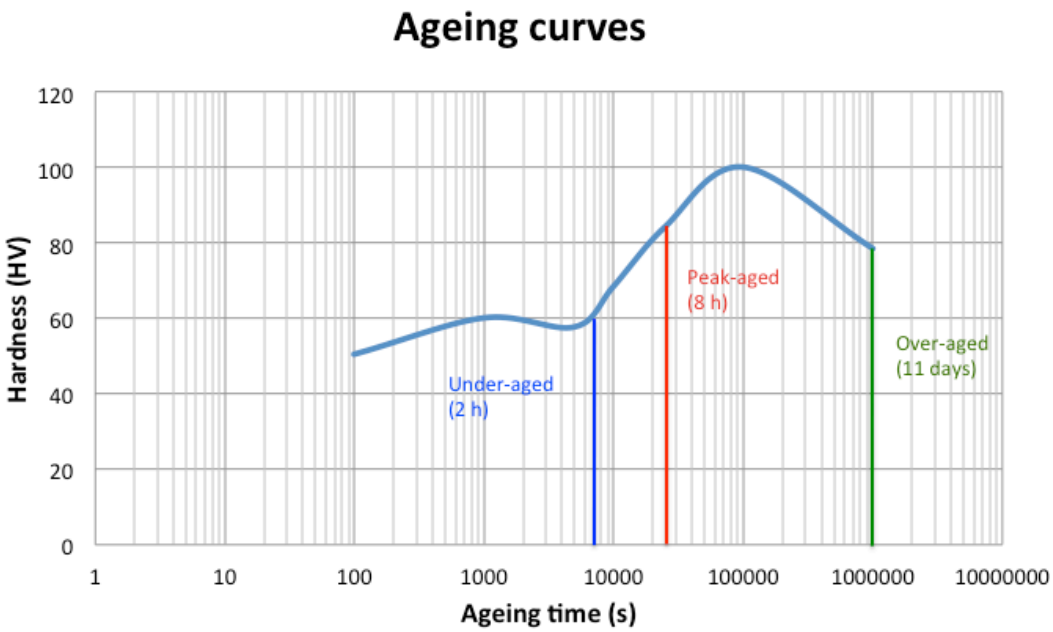

Fig. 4-7: Ageing curves for the extruded condition with an ageing temperature of 175°C for various ageing times. The ageing times that were selected for the different tempers are indicated in the figure.

4.4 Mechanical testing

The AlMgSi alloys stress-strain response to compression is dependent on its condition and how it has been heat-treated (which temper). The results from the mechanical testing are presented in this section. It should be noted that there are only two test parallels of the peak-aged as-cast condition. The third parallel got ruined during the making of the test pieces for the upsetting test.

4.4.1 Stress-strain response to compression

The different conditions stress-strain response to compression is compiled in various stress-strain curves shown in Fig. 4-8, Fig. 4-9 and Fig. 4-10. The engineering stress-strain curves of the different conditions in each of the tempers (all test parallels) can be found in Fig. 4-8, where (a), (b), and (c) shows the curves for the as-cast condition, the extruded condition, and the extruded, cold-rolled and recrystallized condition, respectively. It can be seen from the figures that there is an upward curvature at large strains. This behavior is very different from the stress-strain behavior during a tension test. This upward curvature can be understood from the increased diameter of the specimen, and hence an increase in the specimen area A, as the compression goes on. It can also be seen that there are little dispersion between the parallels, and all the curves for the different conditions show the same tendency; the conditions that have been heat-treated to peak-aged temper exhibit the highest strength, and the

conditions that have been over-aged show about the same initial flow stress as the peak-aged conditions but the work-hardening of the over-aged conditions decreases after about 0.05-0.09 engineering strain, and the strength of the under-aged conditions ascends above that of the over-aged conditions somewhere around 0.2-0.4 engineering strain.

Fig. 4-9 shows the true stress-strain curves of the different conditions, where the engineering stress-strain curves (from Fig. 4-8) have been fitted by the use of Eq. 4-9, i.e. by using a generalized Voce equation with three terms. The generalized Voce fitted stress-strain curves are shown in Fig. 4-9 and Fig. 4-10, with only one selected parallel of each material (the dispersion between the parallels is negligible, as can be seen from Fig. 4-8). The parameters used for the curve fittings are presented in Table 4-2, where only the parameters for the selected parallels shown in Fig. 4-9 and Fig. 4-10 are presented. The parameters for all the parallels can be seen Table A1 in the Appendix.

The stress-strain behavior of the different tempers can be seen much clearer in Fig. 4-9 than in Fig. 4-8. The under-aged material show the same stress-strain behavior in all three conditions, the same does the peak-aged and the over-aged material. The under-aged conditions show a very low initial flow stress. However, the work-hardening potential is large (high initial slope of the curve). The work-hardening rate decreases and the curve gets linear after about 0.2 plastic strain, but the work-hardening is still relatively high as the curve keeps on increasing, and the curve ascends above that of the over-aged condition. The initial flow stress of the peak-aged material is high, but slightly lower than that of the over-aged conditions. The initial work-hardening rate seems to be a little higher than that of the under-aged conditions (slightly steeper initial slope of the curve). The work-hardening rate decreases and the curve enters a linear regime after about 0.1 plastic strain. The work-hardening rate is still relatively high in the linear regime (only slightly lower than that of the under-aged conditions). The peak-aged conditions exhibit the highest final strength. The stress-strain behavior of the peak-aged conditions is very similar to the stress-strain behavior of the under-aged conditions (only with higher strength). The stress-strain behavior of the over-aged conditions on the other hand, are very different. The over-aged conditions exhibit the highest initial flow stress, but also the highest initial work-hardening as they exhibit the highest initial slope of the curve (this is much less pronounced for the over-aged extruded condition). However, after bout 0.007-0.07 plastic strain the work-hardening rate rapidly decreases and the stress-strain curves abruptly starts to flatten out and becomes linear. The curves are not entirely flat in the linear regime, but keeps on increasing with a very small slope of the curve. The over-aged conditions exhibit the lowest final strength.

As already noted, the under-aged material show about the same stress-strain behavior in all three conditions, and the same does the peak-aged and the over-aged materials. In order to look at the difference between the different conditions of the material in the same temper the generalized Voce fitted curves that were shown in Fig. 4-9 are plotted together in a different way in Fig. 10, the conditions with the same temper are plotted together in the same diagram. The conditions that have been heat-treated to peak-aged temper are plotted together in Fig. 4-10 a), and it can be seen from the figure that the as-cast condition and the extruded, cold-rolled and recrystallized condition exhibit the same stress-strain response to compression as their curves are overlapping almost perfectly. The under-aged extruded condition on the other hand, exhibits a lower strength than the two other conditions in the same temper.

The stress-strain curves of the peak-aged conditions can be seen in Fig. 4-10 b). From the figure it can be seen that the peak-aged extruded condition starts with the lowest initial flow stress, however the work-hardening rate in the linear regime ($\varepsilon \sim > 0.1$) is much higher (much steeper slope of the curve) than that of the other two conditions in the same temper. The final strength of the extruded condition is slightly higher than that of the extruded, cold-rolled and recrystallized condition. The condition with the lowest final strength after being heat-treated to peak-aged temper is the as-cast condition.

Fig. 4-10 c) shows the generalized Voce fitted stress-strain curves of the conditions that have been heat-treated to over-aged temper. It can be seen that both the as-cast condition and the extruded, cold-rolled, and recrystallized conditions exhibit the same stress-strain behavior. Both condition have a high initial work-hardening rate (high initial slope of the curve), and both curves abruptly start to flatten out as the work-hardening rate rapidly starts to decrease. This happens at slightly lesser plastic strain for the extruded, cold-rolled, and recrystallized condition, which exhibit the lowest strength of these two conditions. The over-aged extruded condition exhibit a somewhat different stress-strain behavior than the other two conditions in the same temper. The curve is much 'softer' as the initial slope of the curve is much less steep than for the other two conditions (smaller initial work-hardening), and it does not flatten out as abruptly.

The work-hardening parameters used to fit the curves with the generalized Voce equation with three terms are presented in Table 4-2. However, it should be noted that for the samples where the parameter Q_1 is equal to zero the curves are practically only fitted with two terms of the generalized Voce equation. It should also be noted that the Q_3 parameter was fixed to have a constant value of 400 MPa.

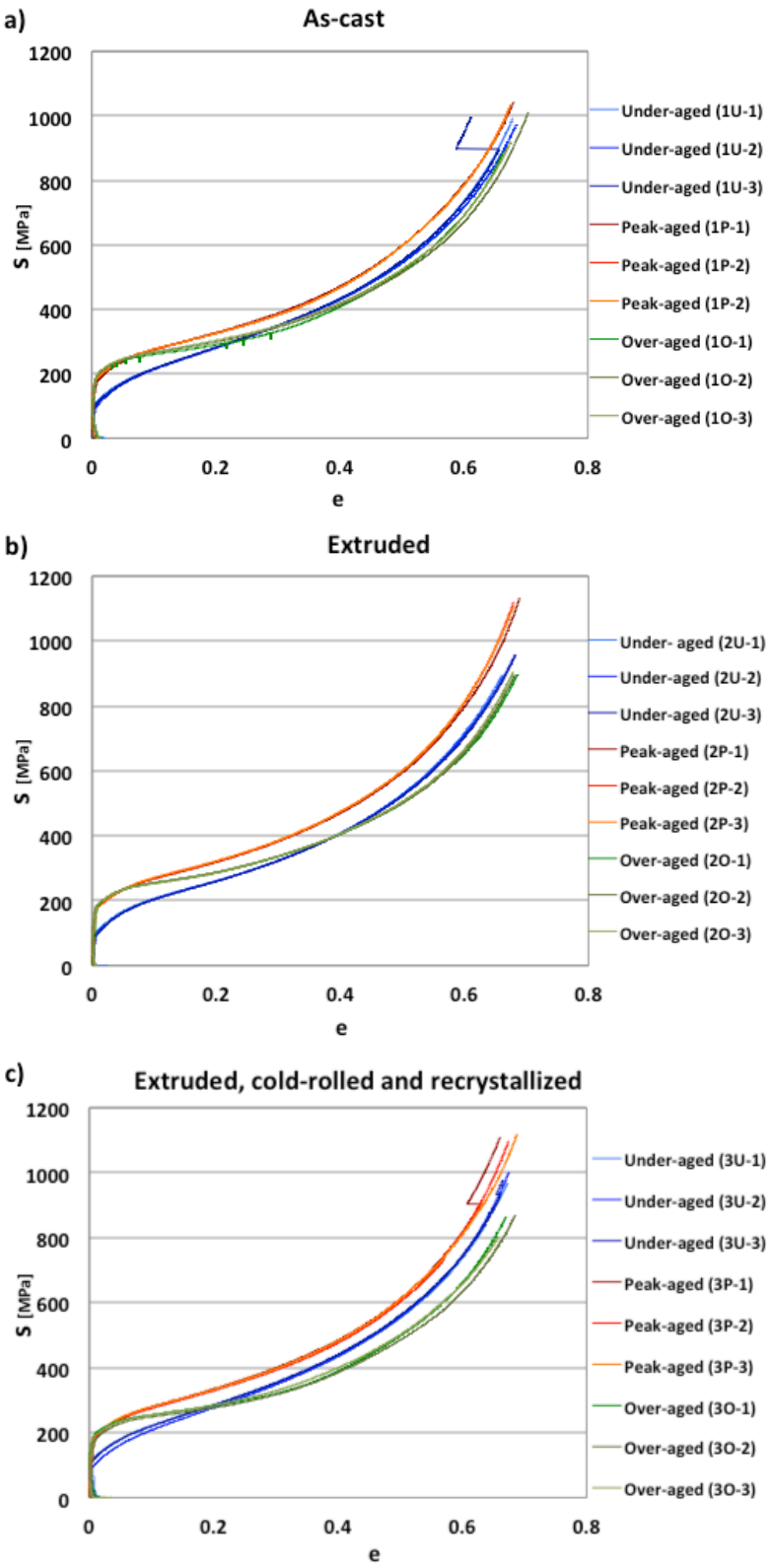

Fig. 4-8: Engineering stress-strain curves of the different conditions: a) As-cast, b) Extruded, c) Extruded, cold-rolled and recrystallized. The curves for all the test parallels of the three tempers; under-aged (2 hours), peak-aged (8 hours), and over-aged (11 days), are plotted together.

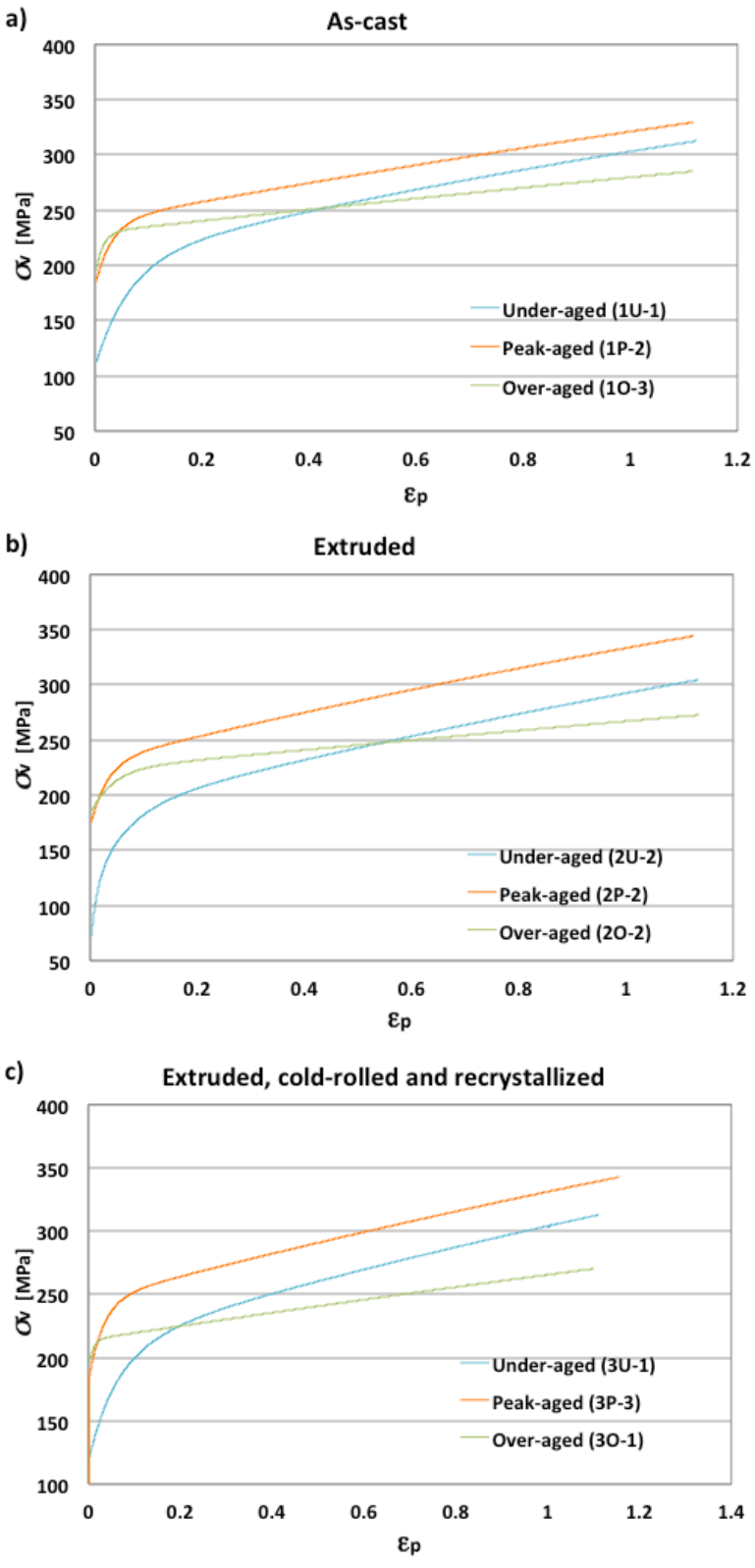

Fig. 4-9: Stress-strain curves (fitted with three terms generalized Voce equation) of the three different conditions: a) As cast, b) Extruded, c) Extruded, cold-rolled, and recrystallized. The three tempers; under aged (2 hours), peak (8 hours), and over aged (11 days), are plotted together.

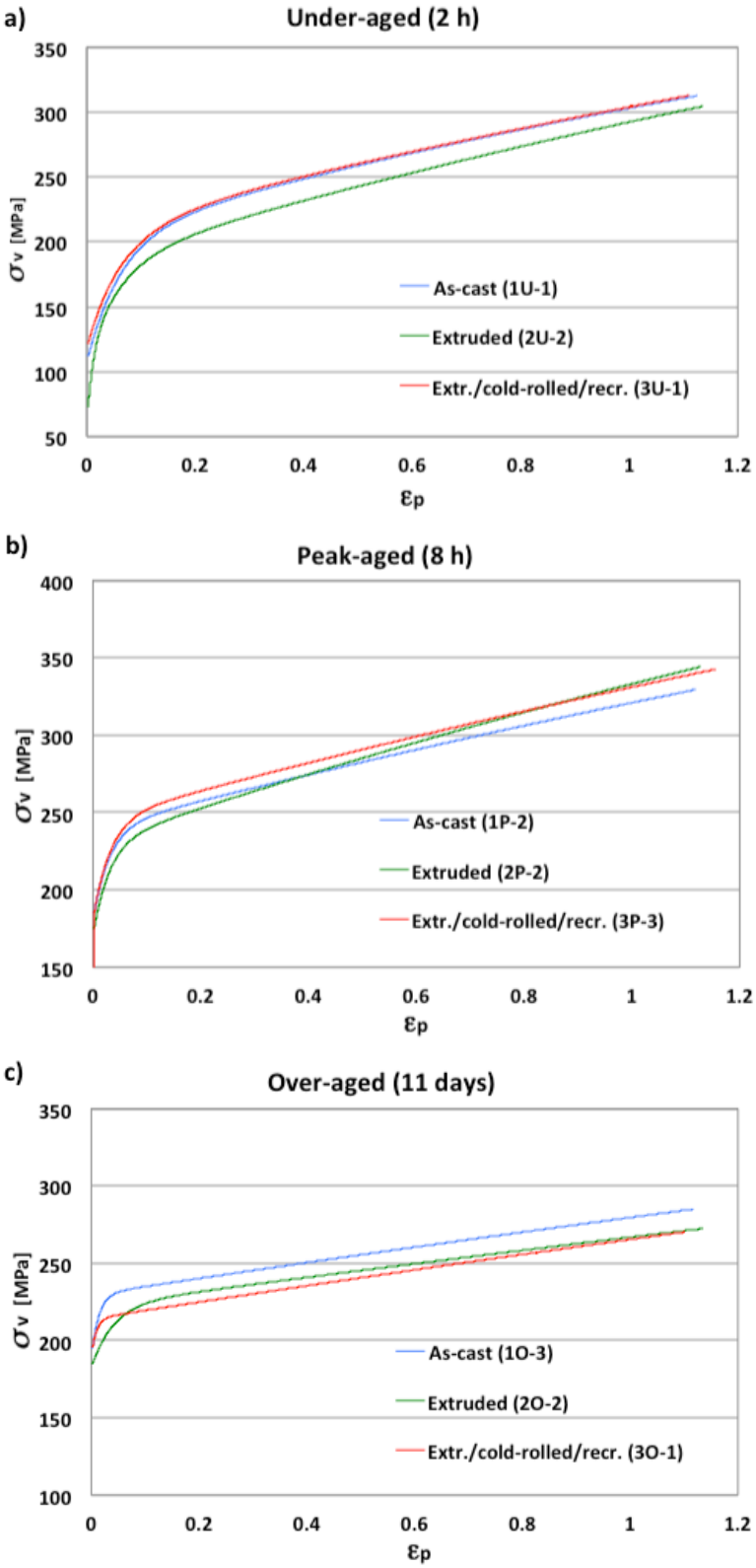

Fig. 4-10: Stress-strain curves (fitted with three terms generalized Voce equiation) of AlMgSi in three different tempers: a) under-aged, b) peak-aged, c) over-aged. The curves of the three conditions; the as-cast condition, the extruded condition, and the extruded, cold-rolled, and recrystallized condition, are plotted together.

Table 4-2: Work-hardening parameters used in the curve fitting (for the selected parallels) with the three terms generalized Voce equation.

Material	σ_0 (MPa)	Q_1 (MPa)	C_1	Q_2 (MPa)	C_2	Q_3 (MPa)	C_3
As cast (1U-1)	107.70	276.90	0.44	96.05	15.71	400	1.00
Extruded (2U-2)	60.91	72.67	15.79	51.10	87.12	400	0.31
Extr./cold r./recr. (3U-1)	117.87	50.75	10.91	42.15	22.10	400	0.27
As cast (1P-2)	180.45	0	15.21	59.15	32.74	400	0.22
Extruded (2P-2)	170.71	0	15.30	58.73	32.97	400	0.30
Extr./cold r./recr. (3P-3)	180.55	0	16.32	64.60	31.32	400	0.24
As cast (1O-3)	188.60	0	10.74	41.00	74.01	400	0.13
Extruded (2O-2)	182.51	0	10.21	39.92	24.80	400	0.12
Extr./cold r./recr. (3O-1)	190.48	0	9.25	23.51	105.25	400	0.14

4.4.2 Upsetting testing

Selected test images taken during the upsetting test can be seen in Fig. 4-11. All the conditions shown in the images have been heat-treated to over-aged temper. The images on the left shows the original shape of test pieces at the start of the upsetting test, the images in the middle shows the test pieces halfway through the upsetting test (after about 200 seconds), while the images on the right shows the test pieces at the end of the upsetting test (after about 400 seconds). Fig. 4-11 a) shows test images of the as-cast condition. It can be seen from the images that halfway through the upsetting test the test piece is somewhat skewed and there is a tendency of barreling. The barreling is also noticeable at the end of the test. Test images of a test piece of the extruded condition can be seen in Fig. 4-11 b). It can be seen from the images that barreling has occurred halfway through the test, but that the test piece is not skewed. The barrel shape can also be seen at the end of the test. A test piece of the extruded, cold-rolled and recrystallized condition can be seen in the test images shown in Fig. 4-11 c). The test piece is very skewed halfway through the test, and there is also a case of barreling. Both the skewed shape and the barreling can still be seen in the test piece at the end of the upsetting test.

It was the over-aged extruded condition that showed the most symmetric deformation during the upsetting test compared to the other conditions in the same temper. The other two conditions (the extruded condition and the extruded, cold-rolled and recrystallized condition) showed a very asymmetric deformation as they both got very skewed during the upsetting test.

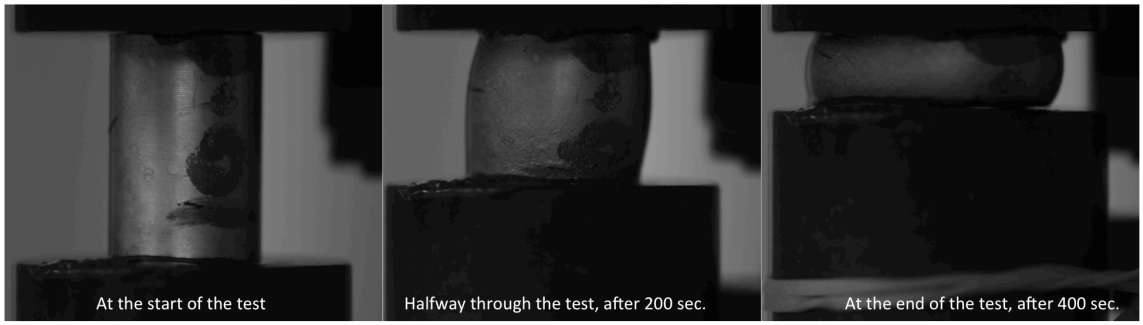

a) As-cast condition (over-aged temper)

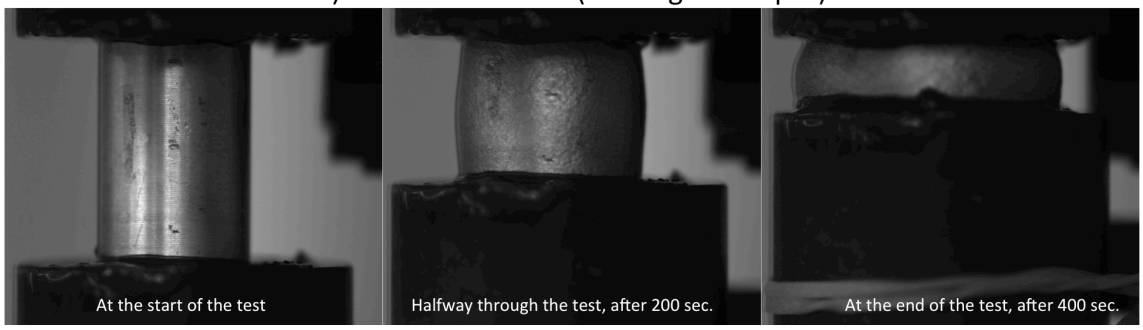

b) Extruded condition (over-aged temper)

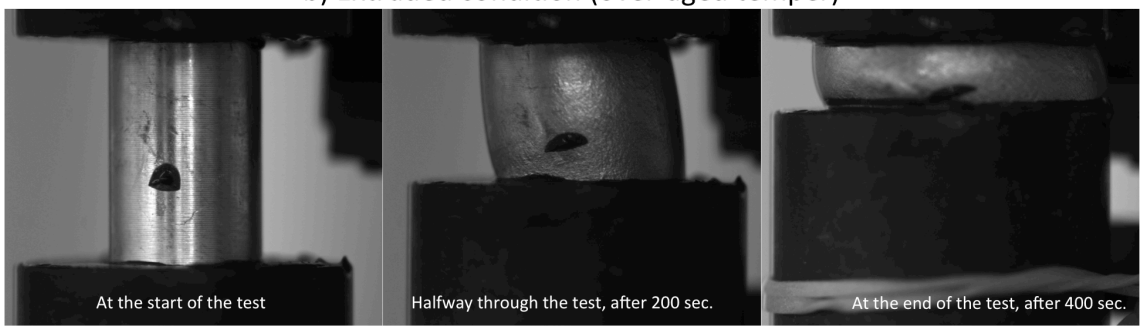

c) Extruded, cold-rolled and recrystallized condition (over-aged temper)

Fig. 4-11: Test images taken during the upsetting testing.

4.5 Characterization of compressed samples

4.5.1 Macrostructure

Optical micrographs of the different conditions (all in over-aged temper) taken after compression can be seen in Fig. 4-12. The compressed test piece of the as-cast condition can be seen in Fig. 4-12 a), and it shows that the test piece is ellipsoidal after the upsetting test. The test piece of the extruded condition (Fig. 4-12 b)) has a fairly circular shape. Fig. 4-12 c) shows the shape of the compressed test piece of the extruded, cold-rolled and recrystallized condition, which have an ellipsoidal shape.

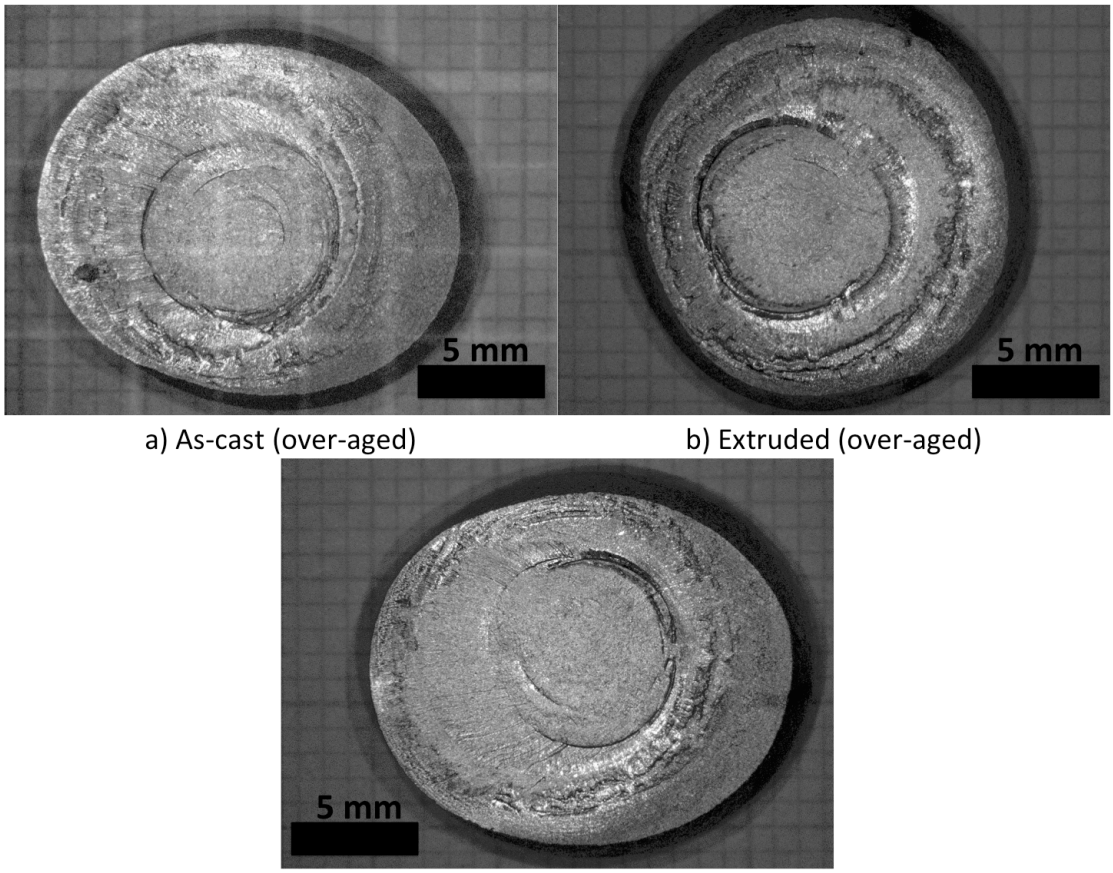

a) As-cast (over-aged)

b) Extruded (over-aged)

c) Extruded, cold-rolled, and recrystallized (over-aged)

Fig. 4-12:Optical micrographs showing the post-compression shape of the different over-aged conditions; a) As-cast, b) Extruded, c) Extruded, cold-rolled and recrystallized.

4.5.2 Grain structure

The compressed grain structure of the different over-aged conditions can be seen in Fig. 4-13, which shows optical micrographs of the whole cross-section (normal to the compression axis) of the test pieces after compression. Red lines in the images indicate the deformation pattern that has developed during compression. The deformation pattern is created by shear bands that consist of elongated and plate-like grains, which have a preferred orientation in the direction of the metal flow. The shear bands in the as-cast condition (Fig. 4-13 a) and the extruded, cold-rolled, recrystallized condition (Fig. 4-13 c) seem to be quite similar, and the other grains in their respective grain structures seem to be equiaxed and to have about the same size. The shear band formation is more pronounced in the extruded condition, this can be seen in Fig. 4-13 b). The deformation in this condition seem to be mainly located in the shear bands, which has resulted in a very non-uniform deformation, leaving some areas in the grain structure almost deformation free. One of these areas is marked as area (1). Another area, which is much closer to the shear bands and much more affected by the deformation, is marked as area (2). Fig. 4-14 shows a magnified image of area (1) and area (2). It can be seen that the grains in area (1) are comparatively large and fairly equiaxed and they seem to have been unaffected by the deformation, while the grains in area (2) are deformed and elongated. Some non-uniform deformation can also be seen in the other two conditions as well, however, much less pronounced.

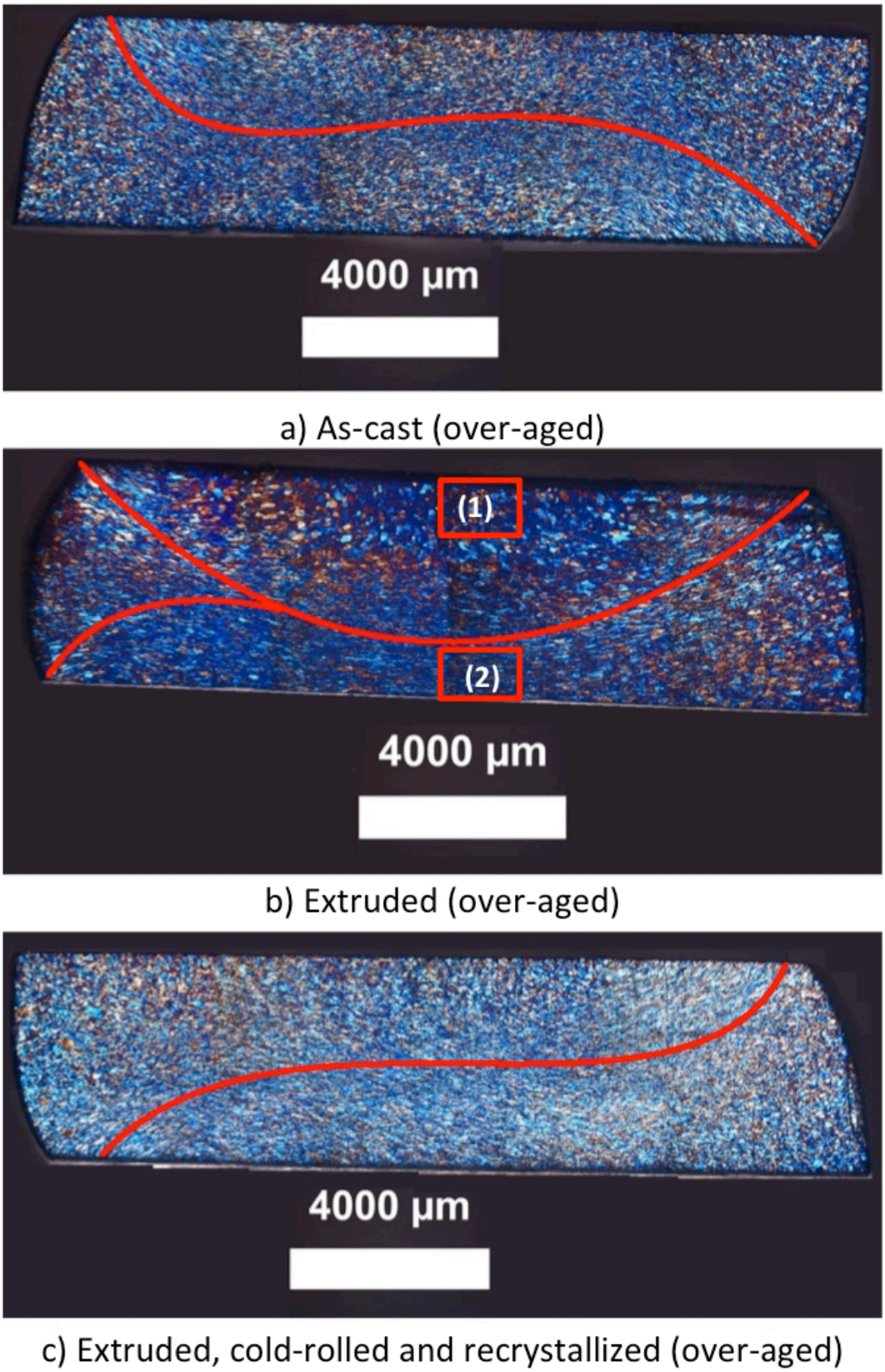

Fig. 4-13: Cross-section (normal to the compression axis) of the different conditions in over-aged temper: a) As-cast condition, b) Extruded condition, c) Extruded, cold-rolled and recrystallized condition.

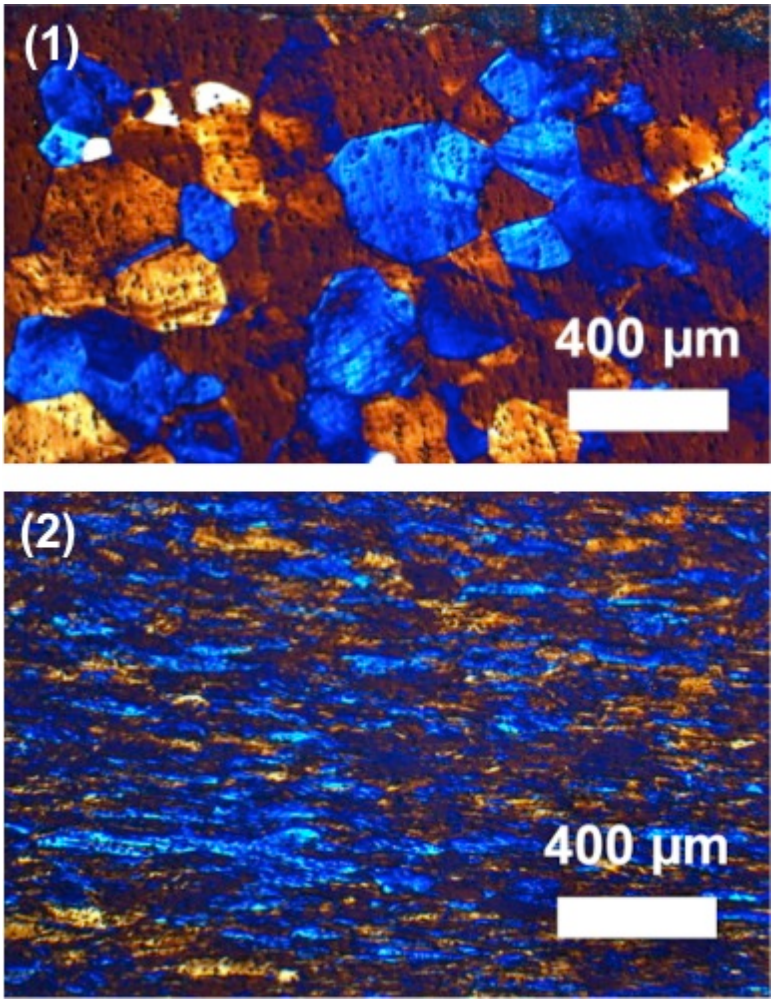

Fig. 4-14: Area (1) and (2) in the compressed grain structure of the over-aged extruded condition shown in Fig 4-13 b).

4.5.3 Particle structure

The compressed particle structure of the different over-aged conditions can be seen in Fig. 4-15, which shows optical micrographs taken around the center of the cross-section normal to the compression axis. The particle structure in the as-cast condition consists of particles that vary somewhat in size and shape, this can be seen in Fig. 4-15 a), some of the particles are round while other are elongated and plate-like. The particles are inhomogeneously distributed in the cross-section and do not seem to have any preferred orientation or alignment, and they are no longer mainly located at the grain boundaries. Fig. 4-15 b) shows the compressed particle structure of the extruded condition. The particles in this condition are inhomogeneously distributed, and vary somewhat in both shape and size and do not seem to have any preferred orientation or alignment. The compressed particle structure of the extruded, cold-rolled and recrystallized condition can be seen in Fig. 4-15 c). It shows particles of various size and shape, but most of them seem round and they seem slightly larger than the particles

seen in the particle structure of the two latter conditions. The particles do not seem to have any preferred orientation or alignment

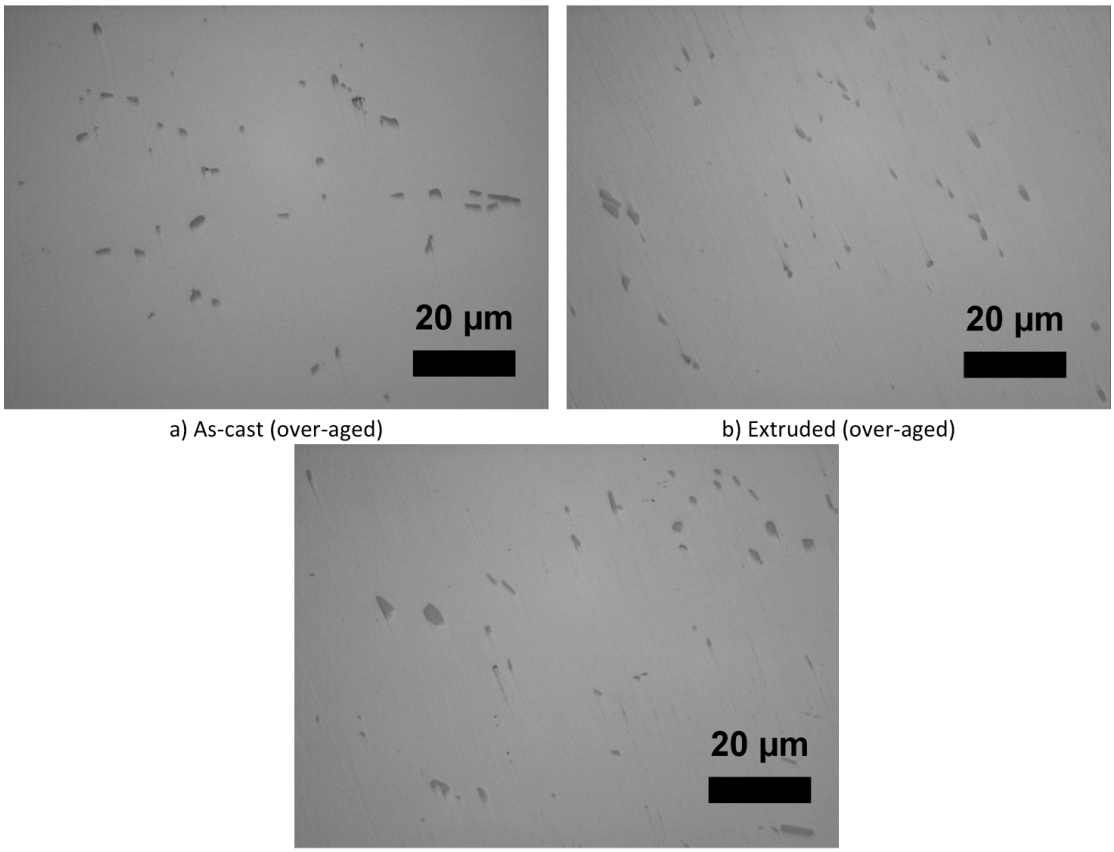

a) As-cast (over-aged)

b) Extruded (over-aged)

c) Extruded, cold-rolled and recrystallized (over-aged)

Fig. 4-15: Optical micrographs showing compressed particle structure of the different conditions in over-aged temper; a) As cast, b) Extruded, c) Extruded, cold rolled and recrystallized.

The compressed particle structure of the different over-aged conditions can be seen more detailed in SEM BSE (scanning electron microscopy backscattered electron) images compared to OM (optical microscopy) images. Fig. 4-16, Fig. 4-17, and Fig. 4-18 show BSE images of the compressed particle structure of the as-cast condition, the extruded condition, and the extruded, cold-rolled, and recrystallized condition, respectively. All the BSE images are taken from around the center of the cross-section normal to the compression axis.

The compressed particle structures of the as-cast condition can be seen in Fig. 4-16. It can be seen from Fig. 4-16 a) that the particles vary a lot in both size and shape. Some of the particles are small and spherical, while others are larger and more plate-like. The particles are inhomogeneously distributed, and they are no longer mainly located at the grain boundaries. From Fig. 4-16 b) it can also be seen that pores have started to form around some of the particles. The pores are indicated with red arrows in the image. It can be seen that the pores are comparatively small and mainly connected to the particles.

Fig. 4-17 shows BSE images of the extruded condition. It can be seen from both Fig. 4-17 a) and b) that the particle structure consists of particles that varies in both size and shape; some are spherical, while others are elongated and plate-like. From Fig. 4-17 b) it looks as though the plate-shaped particles are oriented so they point (with their long axis) in the same direction, the upper right corner of the image.

The BSE images in Fig. 4-18 show the compressed particle structure of the extruded, cold-rolled, and recrystallized condition. From Fig. 4-18 a) it can be seen that the particles varies a in both shape and size. There are both spherical and elongated and plate-like particles. The particles distribution is inhomogeneous. From Fig. 4-18 b) it can be seen that there have been some pore formation in this condition, the pores are indicated with red arrows in the image. The pores are comparatively small and seem to be mainly connected to particles.

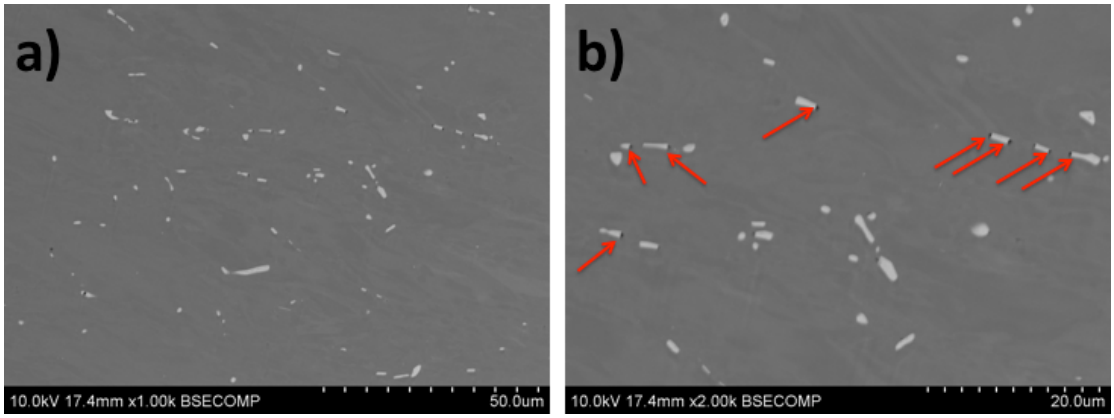

Fig. 4-16: SEM BSE images of the compressed particle structure of the over-aged as-cast condition. The arrows in b) indicates the pore formation. The images are taken from the center of the cross-section normal to the compression axis of the specimen.

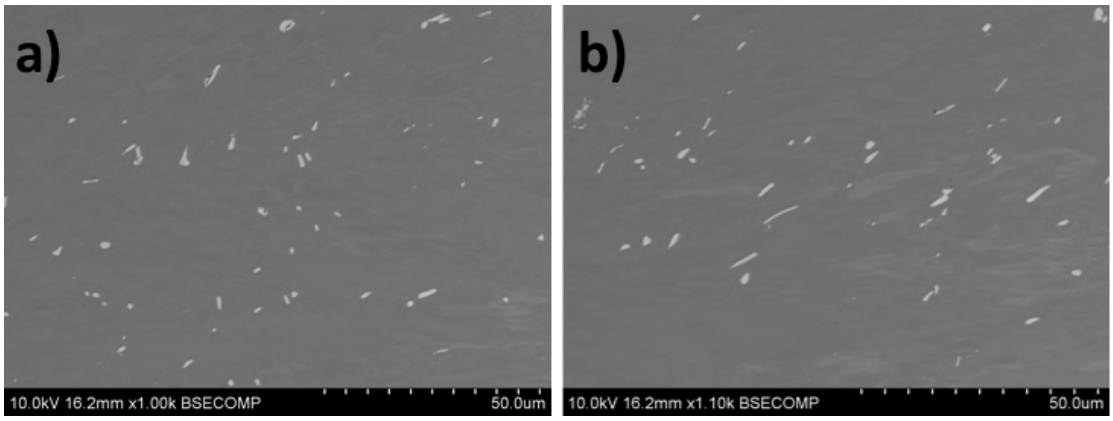

Fig. 4-17: SEM BSE images of the compressed particle structure of the over-aged extruded condition. The images are taken from the center of the cross-section normal to the compression axis of the specimen.

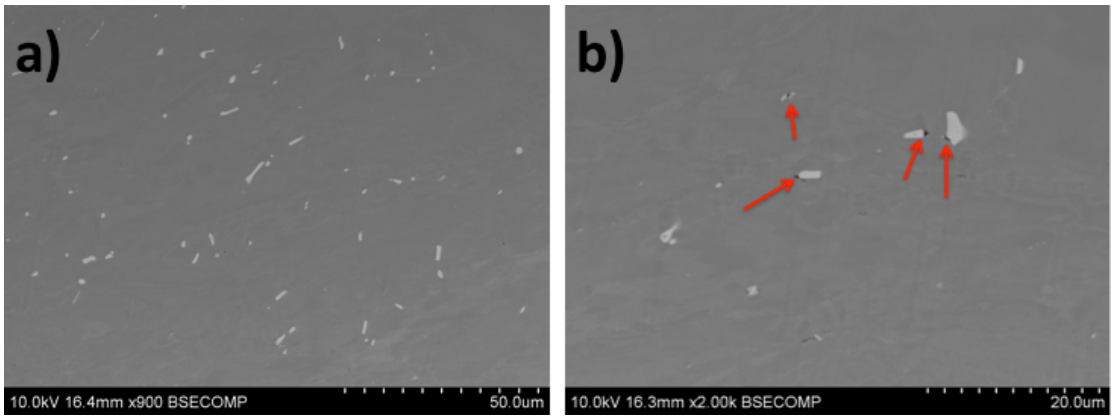

Fig. 4-18: SEM BSE images of the compressed particle structure of the over-aged extruded, cold rolled and recrystallized condition. The arrows in b) indicates the pore formation. The images are taken from the center of the cross-section normal to the compression axis of the specimen.

5 Discussion

5.1 Microstructural changes during thermomechanical processing

5.1.1 Grain and particle structure

Based on the results from the characterization of the initial microstructure of AlMgSi alloy in the different conditions (including the extruded and cold-rolled condition) it is obvious that the material undergoes several microstructural changes during thermomechanical processing. This can be seen in Fig. 4-1, which shows the initial grain structure of the different conditions and illustrate how the grains change after each processing step. The grains are medium sized (~70-80 μm) and equiaxed in the as-cast condition (Fig. 4-1 a). The material obtains a new recrystallized grain structure after extrusion. This is due to spontaneous recrystallization of the deformed structure that develops during extrusion, which happens at the exit of the extrusion die. The mechanical forces applied during the extrusion are sufficient to considerably deform the material, and at the same time the extrusion temperature, about 500-550°C, is high enough to cause spontaneous recrystallization of the deformed structure during/after extrusion. The new spontaneously recrystallized grain structure of the extruded condition can be seen in Fig. 4-1 b). The grains are equiaxed just as the ones in the as-cast condition but somewhat larger (~120 μm).

After cold-rolling the grains get elongated in the rolling direction, this can be seen in Fig. 4-1 c), and this is because they change their shape in correspondence to the macroscopic changes in the material, cf. Fig. 2-9 and Fig 2-10 a) and b). The elongated grains cause a large increase in the total grain boundary area, which serve as possible nucleation sites for recrystallized grains. Excess energy that is introduced during the cold-rolling are stored in the material and released during recrystallization, which happens after heat-treatment (520°C for 10 minutes) of the material. The recrystallization happens by the rearrangement of dislocations and nucleation of new strain free grains [23].The recrystallized grain structure (Fig. 4-1 d) has the same equiaxed grains as the grains in the as-cast condition and the spontaneously recrystallized grains in the extruded condition. However, they are somewhat smaller in size (~50-60 μm).

Also the particle structure of the material is affected by the thermomechanical processing. This can be seen from Fig. 4-2 and Fig. 4-3, which show OM (optical microscopy) images and BSE (backscattered electrons) images of the different conditions, respectively. The particle structure in the as-cast condition (Fig 4-1 a, and Fig. 4-2 a) consists of relatively few particles, which vary in both size and

shape. Some are large and plate-like, while others are small and spherical. The particles are inhomogeneously distributed and located mainly at the grain boundaries. As previously mentioned, because the grains change in correspondence to the macroscopic changes they get elongated and oriented in the extrusion direction during extrusion. This also affects the particle structure. After extrusion the particles tend to get aligned and oriented along the extrusion direction. This can be seen from the images of the extruded condition (Fig 4-2 b, and Fig. 4-3 b). The cold-rolling step can have the same effect on the particle structure and make them even more aligned and oriented in the rolling direction. However, in this work cross-rolling have been applied and this have lead to a randomization of the particle distribution, i.e. the lining up after extrusion is disrupted and the spatial distribution becomes more random again (as before extrusion). This can be seen in Fig. 4-2 c) and Fig. 4-3 c), which both show the initial particle structure of extruded and cold-rolled condition. The particles do not seem to be lined up in the extrusion/rolling direction any longer and they seem to be randomly oriented.

5.1.2 Texture

The texture of the material also changes during mechanical processing. The change in the texture between the different processing steps can be seen from the 111 pole figures and the corresponding ODFs in Fig. 4-4, Fig. 4-5, and Fig. 4-6, which show the texture of the extruded condition, the extruded and cold-rolled condition, and of the extruded, cold-rolled and recrystallized condition, respectively. After extrusion the material gets a texture dominated by Cube texture. However, a little Goss texture can also be seen. This can be seen from the 111 pole figures and the corresponding ODF in Fig. 4-4. Both the Cube and the Goss texture are typical recrystallization textures [27], and the formation of these texture components during extrusion confirms that the material has been spontaneously recrystallized during the extrusion step.

After being further processed by cold-rolling the material should regain a deformation texture. The texture of the extruded and cold-rolled condition resembles a typical aluminium deformation texture, this can be seen from the 111 pole figures and the ODF in Fig. 4-5. However, the texture is very weak, and a one to one correspondence with the typical rolling texture seen in Fig. 2-17 and Fig. 2-18 is difficult to see. The reason why a typical fiber texture cannot be seen in the material is probably because of the cross-rolling.

The deformation texture after cold-rolling is removed when the material is subjected to yet another heat-treatment leading to a second recrystallization. This can be seen from the 111 pole figures and the corresponding ODF in Fig. 4-

6, which show the texture of the extruded, cold-rolled and recrystallized condition. The texture is extremely weak and close to random.

5.2 Stress-strain response to compression

The different conditions response to compression deformation during the upsetting test can be seen in Fig. 5-1, and can say something about their mechanical properties. The under-aged material show the same stress-strain behavior in all three conditions, the same does the peak-aged and the over-aged materials. This can be seen from the stress-strain curves presented in Fig. 5-1. The under-aged conditions show a very low initial flow stress. This is due to the low ageing time (2 hours) and hence there will be a low density of β'' precipitates and low age hardening effect [21]. Furthermore, the precipitates present will be of the shearable type [17]. However, the work-hardening potential is large (high initial slope of the curve), this can also be seen from the corresponding modified Kocks-Mecking plots in Fig. 5-2, which shows a relative little and slow drop in the work-hardening rate θ. This is most pronounced for the under-aged as cast condition (Fig 5-1 a). The high work-hardening potential of the under-aged conditions can be understood from the high level of solute left due to the low ageing time [22]. The stress-strain behavior of the under-aged conditions is in good accordance with the stress-strain behavior predicted by Myhr er al. [22], cf. Fig. 2-8.

Also the peak-aged material shows the same tendency in stress-strain behavior in all three conditions. From Fig. 5-1 it can be seen that the initial flow stress of the peak-aged material is relatively high, but slightly lower than the initial flow stress of the over-aged conditions. The work-hardening potential and the initial work-hardening is large (compared to that of the under-aged conditions), this can be seen from the relatively steep initial slope of the curve and the corresponding modified Kocks-Mecking plots in Fig. 5-2. The work-hardening rate θ decreases and the stress-strain behavior become more linear somewhere around 0.1 plastic strain. However, instead of flattening out the stress-strain curve in Fig. 5-1 keeps on increasing but with a smaller slope of the curve. This stress-strain behavior is somewhat different compared to the stress-strain behavior predicted for peak-aged temper in Fig. 2-8. The initial flow stress is not at a peak level, but slightly lower than that of the over-aged conditions, and the stress-strain behavior is more similar to that of the under-aged conditions, only with a higher strength. This can be explained by the fact that the peak-aged conditions in reality are slightly under-aged (cf. Fig. 4-7 for the ageing curve of the extruded condition) and have not been aged long enough to reach a peak hardness or a peak density of β'' precipitates, and there may still be a decent amount of solute left in the aluminium matrix.

Also the over-aged material shows the same stress-strain behavior in all the three conditions. Fig. 5-1 show that the over-aged conditions exhibit the highest initial flow stress. It can also be seen that the over-aged conditions exhibit the highest initial work-hardening as they have the steepest initial slope of the curves (this is much less pronounced for the over-aged extruded condition). However, the work-hardening rate rapidly decreases after about 0.007-0.07 plastic strain, and after that the stress-strain curve starts to flatten out and becomes linear. The rapid decrease in the work-hardening rate of the over-aged conditions can be seen more clearly in the corresponding Kocks-Mecking plots in Fig. 5-2. The drop in the work-hardening rate θ is very large and abrupt, this is less pronounced for the over-aged extruded condition. The high initial work-hardening of the over-aged conditions can be explained by the fact that all the precipitates are non-shearable, which leads to Orowan looping [22]. Because of the storage of geometrically necessary dislocations in the vicinity of the precipitates, the initial work-hardening rate gets high. The abrupt decrease in the work-hardening can be explained by the fact that the accumulation of dislocation loops around the precipitates starts to cease, and the flow stress starts to get saturated [22]. Even though the flow stress of the over-aged conditions does not reach a completely saturated level in this case, the stress-strain behavior of the over-aged conditions is still in good accordance with the stress-strain behavior predicted in Fig. 2-8.

As already noted, the stress-strain behavior of the under-aged material is the same in all three conditions, and that this is the case for the peak-aged and the over-aged materials as well. So in order to analyze the results presented in Fig. 5-1 even further, the stress-strain curves are plotted together in another way in Fig. 5-3. This is to look at the dispersion between the conditions for each of the ageing tempers. The under-aged conditions can be seen in Fig. 5-3 a), and it shows that the as-cast condition and the extruded, cold-rolled, and recrystallized condition have almost identical stress-strain curves (they are overlapping almost perfectly), while the extruded condition differ from the other two conditions. The shape of the curve is the same, but the strength is lower, especially the initial strength (the initial flow stress). The explanation for this deviation may lay in the initial grain size of the different conditions. All conditions exhibit approximately the same grain structure (since the extruded condition has been spontaneously recrystallized during/after extrusion, and the extruded, cold-rolled, and recrystallized condition has been recrystallized during the heat-treatment). The grain size of the extruded condition is larger (~120 μm) than that of the as–cast condition (~70-80 μm) and the extruded, cold-rolled, and recrystallized condition (~50-60 μm). This may be one of the reasons why the extruded condition exhibit a lower strength than the other two conditions in the same temper, because of the Hall Petch relations, which says that the strength of the

material increases with decreasing grain size [4]. However, the grain size of the different conditions does not vary too much, so it is not expected that this would make any difference on the strength. It is more likely that the difference in the strength of the under-aged conditions can be explained by the differences in the texture. As already mentioned, the extruded condition exhibits a typical recrystallization texture dominated by Cube texture (as can be seen in Fig. 4-4), due to spontaneous recrystallization during/after the extrusion. The extruded, cold-rolled, and recrystallized condition on the other hand, exhibit a texture that is close to random (Fig. 4-5). This is because of the deformations introduced during the cross-rolling and the subsequent annealing, which has removed the existing texture and created a new close-to random texture. The Cube texture gives a lower strength and higher ductility [27] and may be the reason why the extruded condition exhibits a lower strength than the other two conditions.

The stress-strain curves of the peak-aged conditions are shown in Fig. 5-3 b) and it can be seen that the stress-strain behavior is about the same for the as-cast condition and the extruded, cold-rolled, and recrystallized condition (the latter exhibit a slightly higher work-hardening rate in the linear regime ($\varepsilon\sim>0.1$), and hence have a higher final strength). The extruded condition on the other hand, exhibits a much higher work-hardening rate than the other two conditions in the linear regime ($\varepsilon\sim>0.1$) (much steeper slope of the curve). Due to this high work-hardening the extruded condition has the highest final strength even though it also has the lowest initial strength (initial flow stress). The higher work-hardening rate for the extruded condition can be explained by the fact that the conditions may have different precipitation kinetics. It should be noted that the ageing curves shown in Fig. 4-7 are only based on the ageing sequence of the extruded condition. The same ageing time where chosen for all the different conditions, as the same ageing curve was assumed for the other two conditions as well. In reality, the ageing curves for the as-cast condition and the extruded, cold-rolled, and recrystallized condition may look somewhat different. Fig. 5-4 gives a general illustration of two different ageing curves and how the same ageing time may give a different ageing temper.

It may seem as though the precipitation kinetics are faster for the extruded, cold-rolled, and recrystallized condition, especially since it reaches a typical over-aged stress-strain behavior (high initial slope of the curve before it abruptly flattens out, cf. Fig. 2-8) faster than the other two conditions, as can be seen in Fig. 5-1 c). It can also be seen that the typical over-aged stress-strain behavior is less pronounced for the extruded condition, which have a somewhat soft curve with a lower initial slope and the curve does not flatten out as abruptly as for the two other conditions in the same temper. Again, this can be explained by the different precipitation kinetics of the conditions, but it may also be because of different precipitation structure. The precipitation type, density and size may be

different for the different conditions, and may be one of the reasons why there is dispersion in the stress-strain behavior, as seen in Fig. 5-1. However, the precipitate structures have not been analyzed so it is not possible to tell for sure if there is a difference there, but it is reasonable to believe so because of the different thermomechanical history of the different conditions. Another explanation for the differences in these stress-strain curves may be because of the different deformation behavior during compression. The deformation of the grains in the over-aged extruded condition is much more non-uniform than the deformation in the other two conditions in the same temper, this can be seen in Fig. 5-5. The deformed microstructure of the compressed samples will be more thoroughly discussed in the next section.

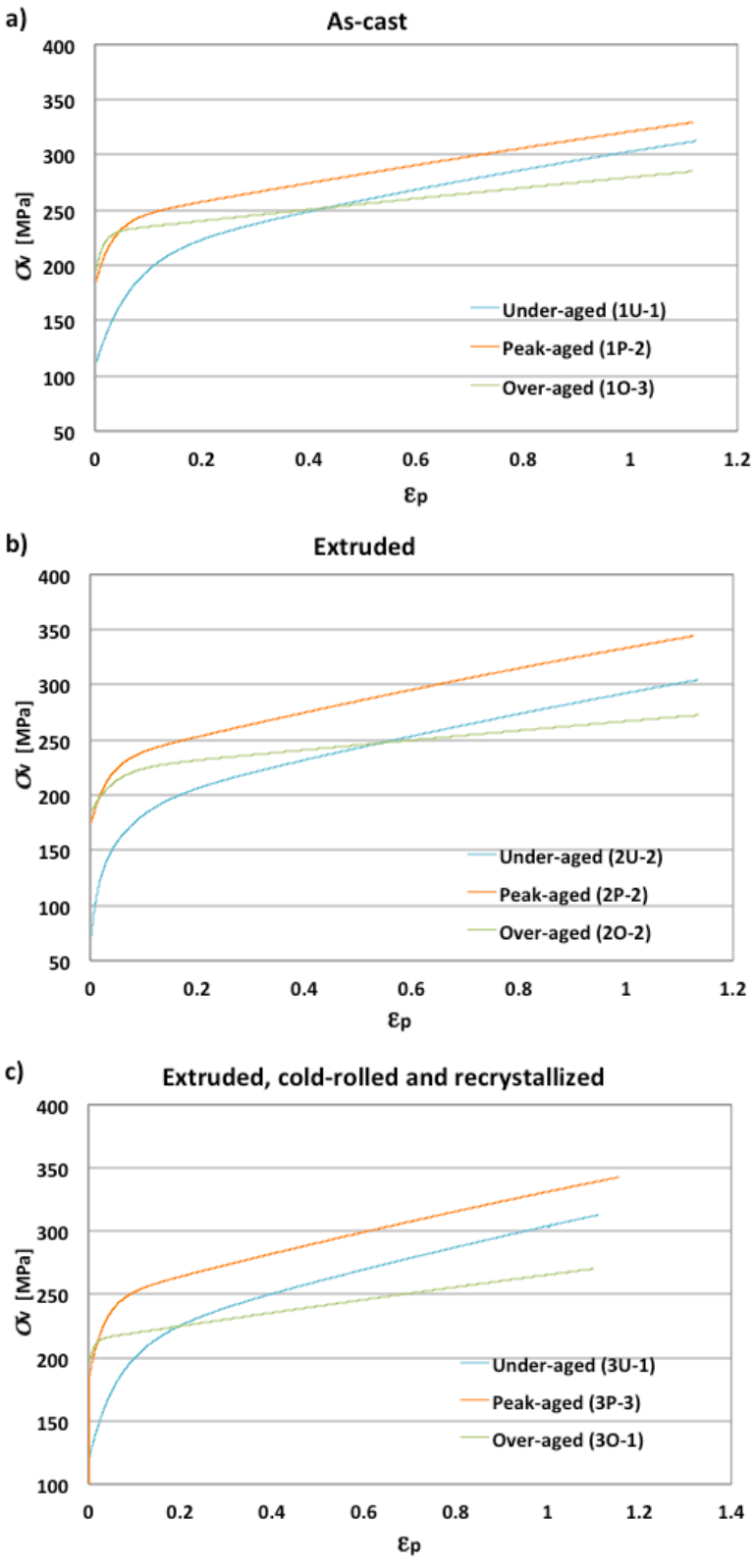

Fig. 5-1: Stress-strain curves (fitted with three terms generalized Voce equiation) for AlMgSi in: a) As-cast condition, b) Extruded condition, c) Extruded, cold-rolled, and recrystallized condition. The three tempers; under aged (2 hours), peak (8 hours), and over aged (11 days), are plotted together.

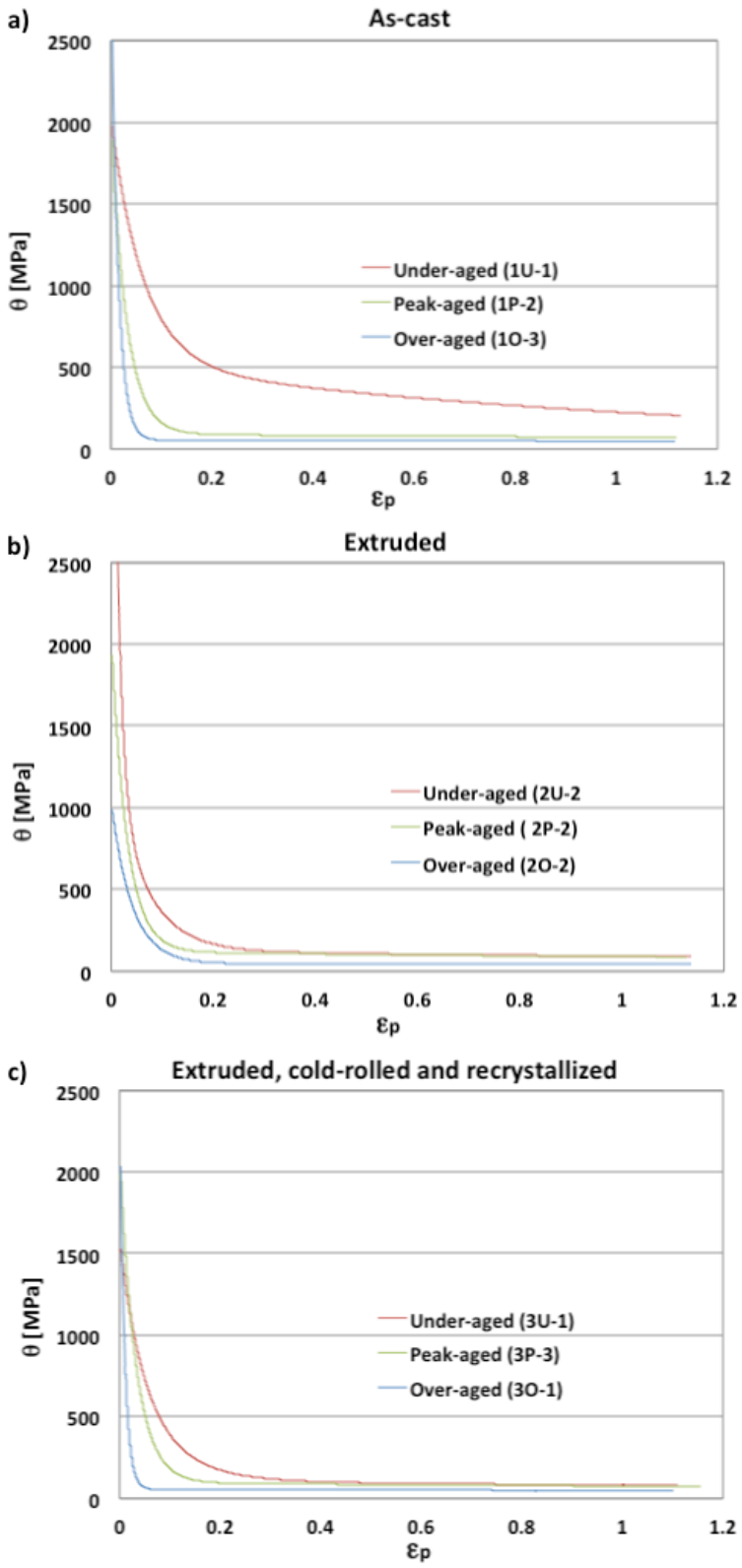

Fig. 5-2: Modified Kocks-Mecking plots of the different conditions in different tempers. a) As-cast, b) extruded, c) extruded, cold-rolled, and recrystallized.

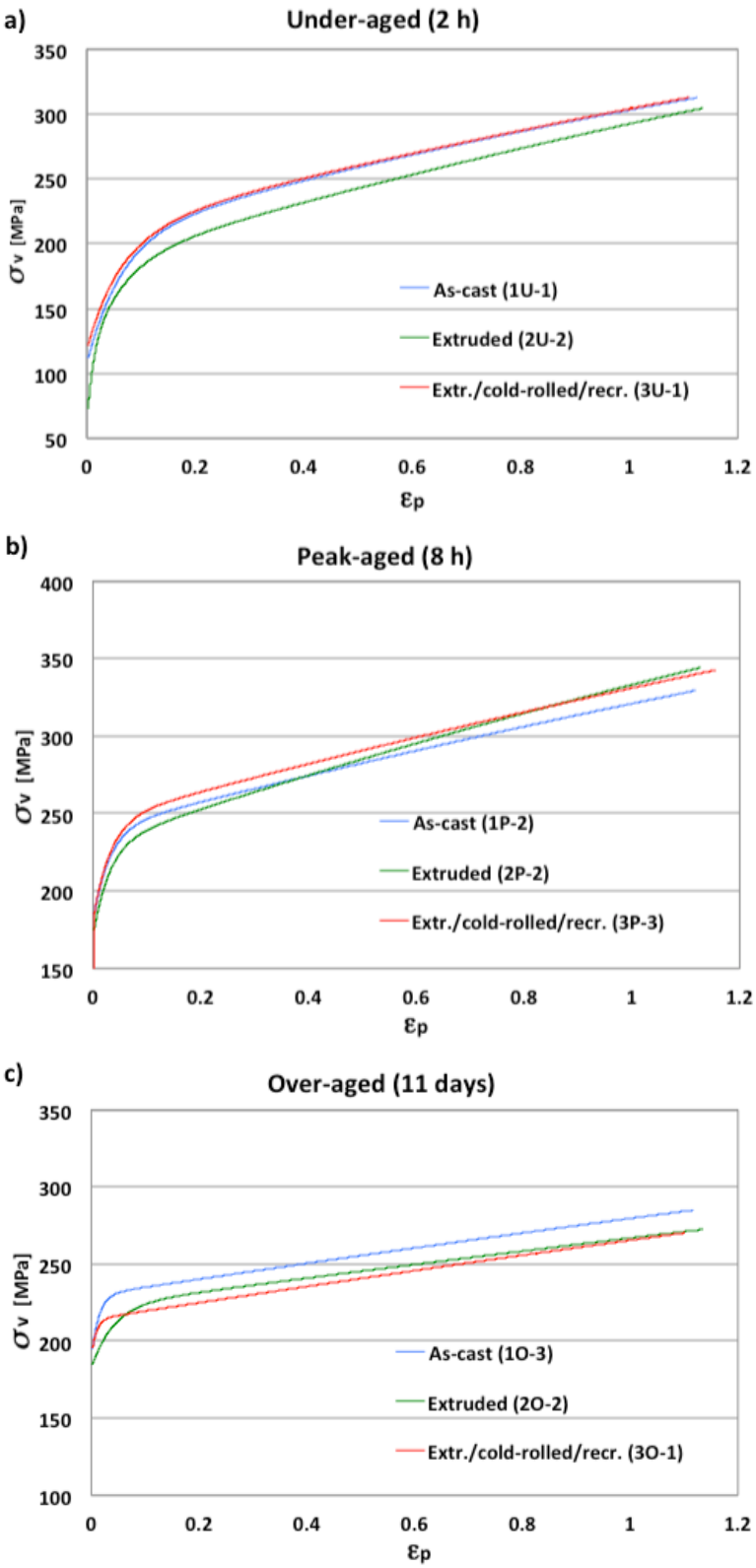

Fig. 5-3: Stress-strain curves (fitted with three terms generalized Voce equiation) of AlMgSi in three different tempers: a) under-aged, b) peak-aged, c) over-aged. The curves of the three conditions; the as-cast condition, the extruded condition, and the extruded, cold-rolled, and recrystallized condition, are plotted together

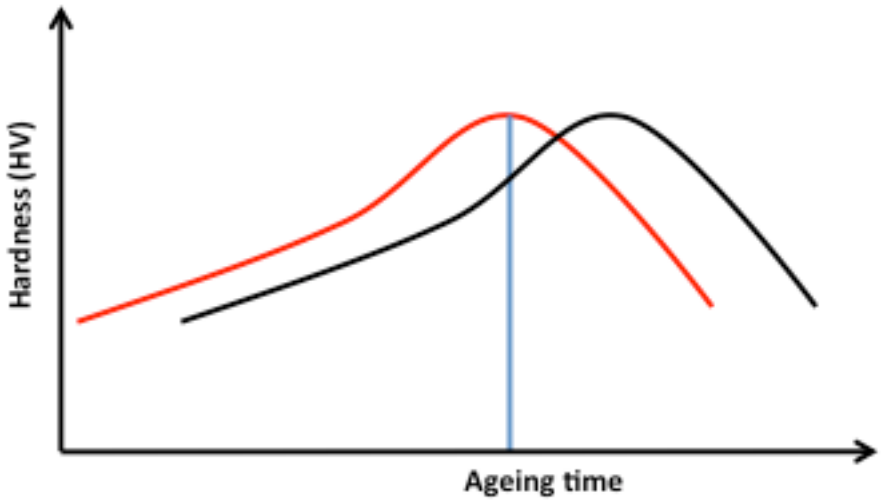

Fig. 5-4: A general illustration of two different ageing curves and how the same ageing time may give a different ageing temper

5.3 Microstructural changes after compression

The conditions that have been heat-treated for 11 days to over-aged temper have been selected for the characterization of the compressed microstructure. In order to understand the microstructural changes that happen during compression it is also important to look at the macroscopic changes. From Fig. 4-11, which shows selected images of the conditions in over–aged temper taken during the upsetting test, it can be seen that all the over-aged conditions experience some barreling during the compression. It can also be seen that the as-cast condition and the extruded, cold-rolled and recrystallized condition both are skewed halfway through the upsetting test, Fig. 4-11 a) and c), respectively. The asymmetric deformation during compression can also be seen in the macrographs of the compressed samples shown in Fig. 4-12. The conditions that were skewed during the compression (the as-cast condition and the extruded, cold-rolled, and recrystallized condition) have an ellipsoidal shape after the upsetting test, this can be seen in Fig. 4-12. The over-aged extruded condition on the other hand, exhibit a much more symmetric deformation (Fig. 4-11 b) resulting in a circular test piece after the compression (Fig. 4-11 b). The reason why the over-aged extruded condition show a much more symmetric deformation compared to the other two conditions in the same temper may be explained by the Cube texture, which gives a higher ductility and formability [27].

The deformation introduced during the compression has also made some changes on the microstructures. From Fig. 5-5, which shows the compressed grain structure of the different conditions, it can be seen that the compression

deformation has caused formation of shear bands. These shear bands have been formed in regions of high strain, and they cut through the existing grain structure. The grains in the shear bands are elongated and oriented in a preferred direction, which creates a particular flow pattern in the grain structure. Red lines are drawn in the images to indicate this flow pattern. The grain structures of the as-cast condition and the extruded, cold-rolled and recrystallized condition (Fig. 5-5 a and Fig. 5-5 c, respectively) are quite similar. They both have about the same grain size and similar flow pattern. The grain structure and the flow pattern in the extruded condition however, looks different, this can be seen in Fig. 5-5 b). The shear bands in this condition is more pronounced, and the deformations seem to be mainly located in these shear bands, and this has lead to a very irregular grain structure as some areas in the cross-section seem to be almost unaffected by deformation. One of these areas is marked as area (1) in the image, while another area, that is much closer to the shear bands and thus more affected by the deformation is marked as area (2). Fig. 5-6 shows magnified images of area (1) and area (2). It can clearly be seen from the images that the grains in area (1) are large and fairly equiaxed, and that they seem to be unaffected by the deformation. The grains in area (2) on the other hand, have been deformed and elongated. As already noted, this non-uniform deformation shown in the over-aged extruded condition may be one of the reasons why the corresponding stress-strain curve shown in Fig. 5-3 differ from the curves of the other two conditions in the same temper. This non-uniform deformation can also be seen in the other two conditions but not as pronounced as for the extruded condition. The reason why the microstructural deformation is much more non-uniform in the over-aged extruded condition compared to the other two conditions in the same temper, may be because of its texture, which is dominated by Cube texture. The Cube texture normally gives a good resistance to shear band formation. However, once shear bands have been formed it would be easier for the deformations to be localized in these shear bands because of the Cube texture. A little Goss texture can also be seen in the texture of the extruded condition, which can help initiate the formation of shear bands [27].

a) As-cast (over-aged)

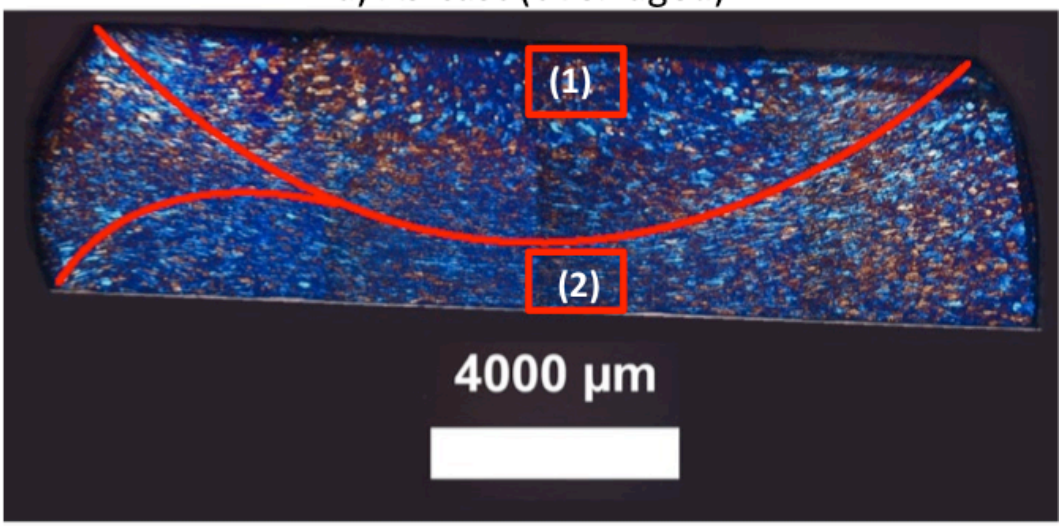

b) Extruded (over-aged)

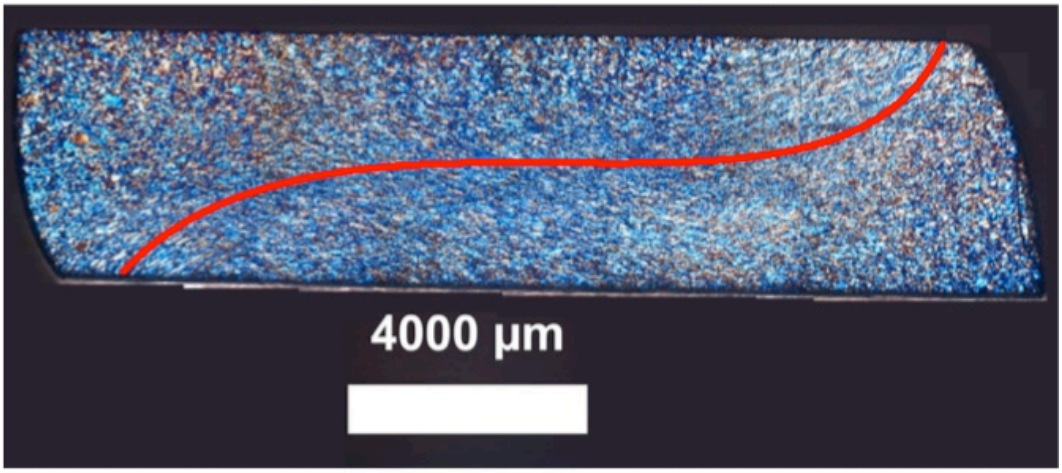

c) Extruded, cold-rolled and recrystallized (over-aged)

Fig. 5-5: Cross-section (normal to the compression axis) of the different conditions in over-aged temper; a) As cast condition, b) Extruded condition, c) Extruded, cold-rolled and recrystallized condition.

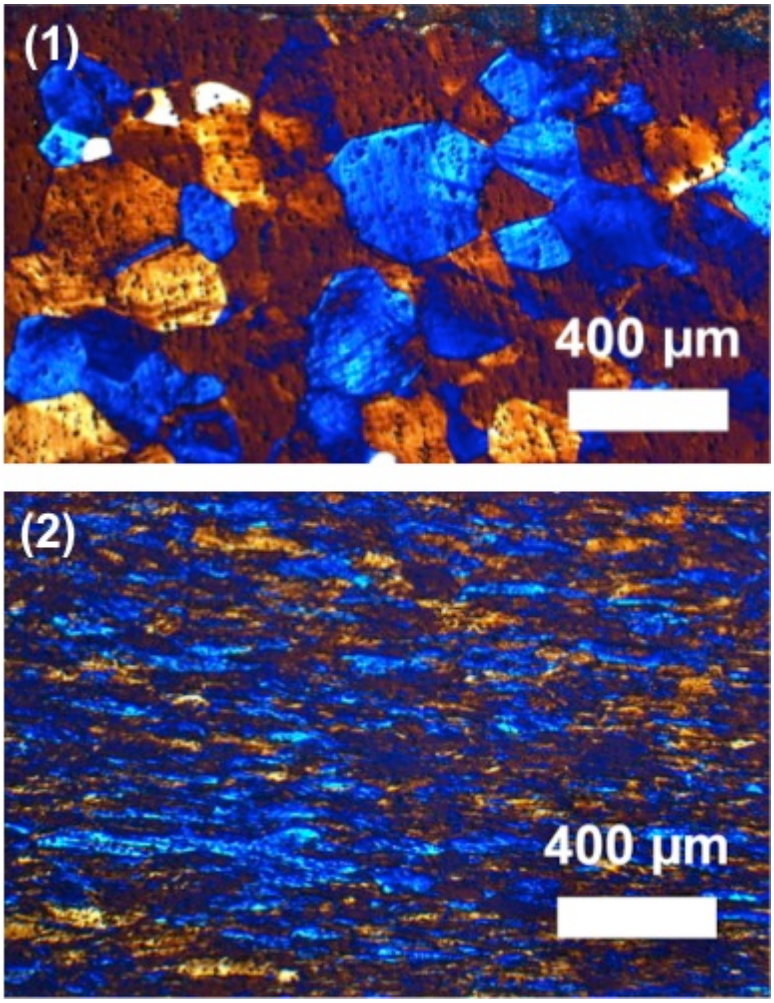

Fig. 5-6: The grains in area (1) and (2) for the over-aged extruded condition shown in Fig. 5-5 b).

The compressive forces applied during the upsetting test have also made some changes to the particle structure of the different conditions. The particles in the as-cast condition no longer seem to be mainly located at the grain boundaries. This can be seen Fig. 5-5 which shows BSE images of the as-cast condition prior to compression (a), and after compression (b). The image of the compressed particle structure is taken from around the center of the cross-section normal to the compression axis. The size and shape of the particles have not changed noticeably after the compression.

The compressed particle structure of the extruded, cold-rolled and recrystallized condition is somewhat similar to the one of the as-cast condition, and in both conditions dark spots can be observed in the BSE images in Fig. 5-6, and are indicated with red arrows. These dark spots may be Mg_2Si precipitates like the ones Couto et al. [28] found in their research, cf. Fig. 2-20, since the alloys used in this work have been air cooled after homogenization, which can lead formation of Mg_2Si precipitates. However, even though a few Mg_2Si precipitates can be observed in the initial particle structure of these two conditions as well (cf. Fig.

4-3), the spots in the compressed particle structure is of a different character. Because of their small size and the fact that they are tightly connected to the bright AlFeSi particles it is reasonable to believe that these spots are pores and not Mg_2Si. Pore formation may have been initiated by fracture of the AlFeSi particles or decohesion between the particles and the matrix caused by the compressive load introduced during the upsetting test. Poor particle cohesion is expected in the as-cast condition since the particles are mainly located at the grain boundaries, and the particles in the extruded, cold-rolled, and recrystallized condition will also have a poor cohesion to the matrix due to the cold deformation during the cold-rolling. Upon further compressive load more pores might be formed or the existing ones might grow and coalesce, which could eventually lead to initiation of a ductile fracture.

No pore formation can be observed in the BSE images of the over-aged extruded condition (Fig. 5-7). This may indicate that the extruded condition is less prone to pore formation and ductile fracture initiation than the other two conditions, where pore formations are observed. As already noted, the reason why pores have started to nucleate in the other two conditions may be explained with poor particle cohesion. Because of the high temperature introduced during extrusion (500-550°C) it is reasonable to believe that the particles in the extruded condition have a much better cohesion to the surrounding aluminium matrix than the particles in the other two conditions, and may be the reason why no pore formation can be observed in this condition. Another reason why pores have not nucleated in the extruded condition may be because of the much more symmetric macroscopic deformation, cf. Fig. 4-11. As already noted, this may be because of the Cube texture present in the extruded condition, which gives a higher ductility and formability [27].

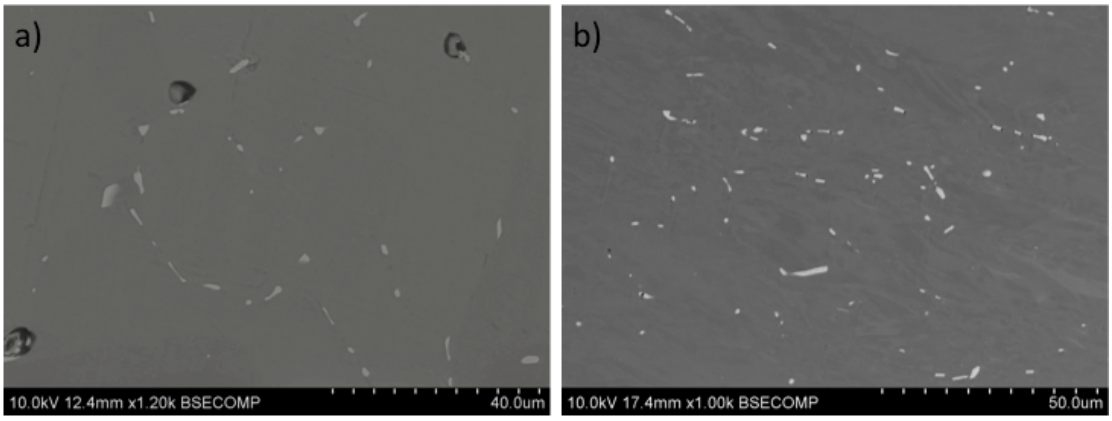

Fig. 5-5: SEM BSE images of AlMgSi in as-cast condition (over-aged temper): (a) initial particle structure, (b) compressed particle structure (around the center of the cross-section normal to the compression axis).

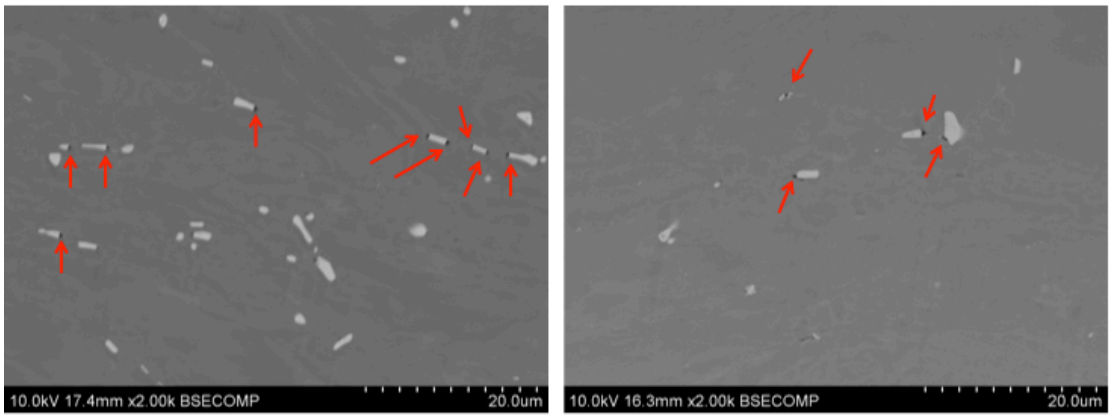

Fig. 5-6: SEM BSE images of (a) as-cast condition and (b) extruded/cold-rolled/recrystallized condition. The pores are indicated with red arrows.

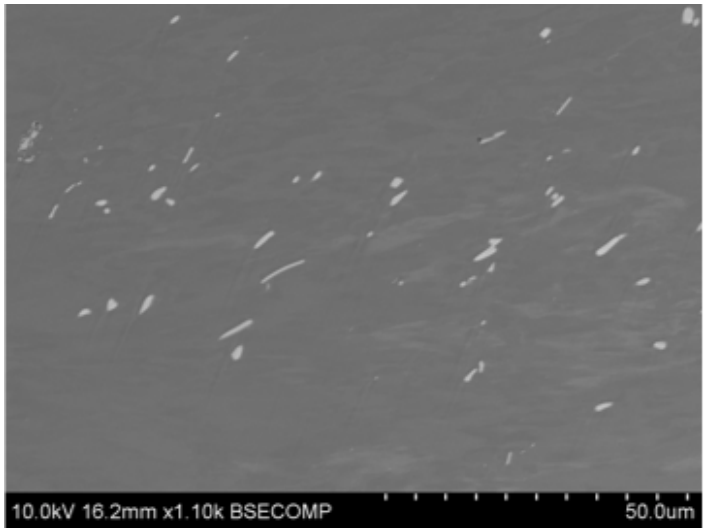

Fig. 5-7: SEM BSE image of the extruded condition. The image is taken around the center of the cross-section normal to the compression axis.

6. Conclusion

Based on the results obtained from the characterization of the initial microstructures, the stress-strain behavior during the upsetting test, and the characterization of the compressed samples of an AlMgSi alloy in different conditions and tempers, the following conclusions can be drawn:

- The initial microstructure of the AlMgSi alloy is very dependent on the thermomechanical history of the material. The grain structure of the as-cast condition consists of equiaxed grains of medium size (70-80 μm), and the particles are inhomogeneously distributed and mainly located at the grain boundaries. The grain structure and the particle structure, as well as the texture change during thermomechanical processing. The alloy gets spontaneously recrystallized during/after extrusion because of the deformation combined with the heat (500-550°C) that is introduced during extrusion. This leads to an equiaxed grain structure similar to that of the as-cast condition and a recrystallization texture dominated by Cube texture. The particles tend to get both oriented and aligned in the direction of the extrusion (ED). When the alloy is further processed by cold-rolling (cross-rolling) the grains obtain a deformed structure as they get flat and elongated along the rolling direction (RD). The cold-rolling results in a deformation texture, which is very weak because of the cross-rolling. The cross-rolling also results in a more randomized particle structure. Finally, annealing the material leads to a second recrystallized grain structure. However, this does not result in a recrystallization texture but a very weak close-to random texture, due to the cross-rolling. This emphasizes the importance of the alloys thermomechanical history, and how it affects the microstructure. The particle structure does not change noticeably after the recrystallization step.

- The stress-strain behavior of the AlMgSi alloy during compression depends on the condition it is in e.g. as-cast condition, extruded condition, or extruded, cold-rolled, and recrystallized condition and which temper it has been age hardened to (under-aged temper, peak-aged temper, or over-aged temper). The stress-strain behavior of the alloy is different depending on which temper it has been heat treated to. The highest final strength of the alloy was obtained after artificially ageing it to the peak-aged temper (8 hours), while the lowest final strength was obtained after artificially ageing it to the over-aged temper (11 days). The alloy shows a very distinct stress-strain behavior in each of the different tempers. The difference in stress-strain behavior between the different tempers are

related to the ageing time and on the density of β'' precipitates formed and whether the precipitates are shearable or non-shearable. The stress-strain curve has a very typical behavior for under-aged, peak-aged, and over-aged material regardless of what condition the alloy is in, there are only relatively small differences in the work-hardening between the different conditions. However, these small differences can be explained by the fact that the ageing time that were selected for all three conditions was based on the ageing curve of only the extruded condition. The ageing curve may look different for the as-cast condition and the extruded, cold-rolled, and recrystallized condition, and the precipitation kinetics may be different from one another. The texture of the different conditions, as well as possible differences in the precipitate structure (type, density, and size) may also be factors influencing the stress-strain behavior of the different conditions.

- The compressed grain structure after the upsetting test clearly shows that the material has been affected by the compression deformation introduced during the upsetting test. Shear bands have been formed in all three conditions, but they are much more pronounced in the over-aged extruded condition, compared to the other conditions in the same temper. The grain structure of the over-aged extruded condition also exhibit a much more non-uniform deformation than the other two conditions in the same temper as the deformations are mainly located in the shear bands resulting in areas in the cross-section that is almost unaffected by the compression deformation. This may also explain the low work-hardening rate observed in the over-aged temper.

- The particle structure has also been affected by the compression deformation introduced during the upsetting test. For instance, the particles in the as-cast condition are no longer mainly located at the grain boundaries. Pore formation can also be observed in the as-cast condition and the extruded, cold-rolled, recrystallized condition. These pores are very small and mainly connected to the AlFeSi particles. However, a SEM/EDS analysis (energy dispersive X-ray spectroscopy) or an XRD analysis (X-ray diffraction) should be performed in future work in order to ensure that the pores are not in fact just Mg_2Si precipitates. The reason why no such pore formation has occurred in the extruded condition may be because of better particle cohesion due to extrusion at elevated temperatures (500-550°C). It may also be because the extruded condition (in the over-aged temper) shows a much more symmetric macroscopic deformation during the upsetting test. The other two conditions in the same temper got very skewed during the compression, which resulted in

ellipsoidal shaped test pieces. The much more symmetric deformation of the extruded condition may be explained by the Cube texture, which gives a higher ductility and formability.

- Based on the remarks about how the extruded condition did not get as asymmetrically deformed as the other conditions during compression, and that no pore formation have been observed in this condition, it may seem like the AlMgSi alloy exhibit the best compression properties and is less prone to pore formation and hence ductile fracture initiation when it is in extruded condition. The alloy should be heated to peak-aged temper if a high hardness and strength is desirable.

7. References

[1] AluminiumLeader. *Transport*. Available: http://www.aluminiumleader.com/en/around/transport/

[2] I. Westermann, K. O. Pedersen, T. Børvik, and O. S. Hopperstad, "Effects of particles and solutes on the strength, work-hardening and ductile fracture of aluminium alloys," (In preparation).

[3] D. R. Askeland and P. P. Phulé, *The science and engineering of materials*. Toronto, Ont.: Thomson, 2006.

[4] J. K. Solberg, *Teknologiske metaller og legeringer*. Institutt for Materialteknologi, Norges Teknisk-Naturvitenskapelige Universitet, 2010.

[5] I. De Graeve and J. Hirsch. (2001-2010). *Wrought Aluminium Alloys*. Available: http://aluminium.matter.org.uk

[6] B. Rinderer, "The metallurgy of homogenisation," *Materials Science Forum,* vol. Vol. 693, 2011.

[7] G. Marshall, P. Evans, and A. Green. (1997). *Aluminium Alloys: Processing*. Available: http://www.matter.org.uk/matscicdrom/manual/ap.html

[8] D. Lassance, "Modeling of damage mechanisms in AlMgSi alloys, Understanding the role of homogenization on the extrudability," Universite Catholique De Louvain, Belgium, 2006.

[9] H.-W. Huang and B.-L. Ou, "Evolution of precipitation during different homogenization treatments in a 3003 aluminum alloy," *Materials & Design,* vol. 30, pp. 2685-2692, 2009.

[10] G. E. Dieter and D. Bacon, *Mechanical metallurgy*. London: McGraw-Hill, 1988.

[11] K. E. Snilsberg, "Anisotropi i bøyegenskaper hos utherdbare ekstruderte aluminiumslegeringer," Institutt for Materialteknologi Norges Teknisk-Naturvitenskapelige Universitet, Trondheim, 2008.

[12] OsbornMetals. *Steel & Titanium Extrusioin*. Available: http://www.osbornmetals.com/Extrusions.htm

[13] ProductionNavigator. *Rolling, The Process*. Available: http://www.productionnavigator.nl/ventura/engine.php?Cmd=see&P_site=790&P_self=353&PMax=1&PSkip=0

[14] NDT-ResourceCenter. *Thermal Treatments (Heat-Treating)*. Available: http://www.ndt-ed.org/EducationResources/CommunityCollege/Materials/Structure/thermal.htm

[15] KeyToMetals. (2010). *Precipitation Hardening of Aluminum Alloys* Available: http://www.keytometals.com/page.aspx?ID=CheckArticle&site=ktn&NM=235

[16] I. Polmear, *Light Alloys: From traditional alloys to nanocrystals*. Amsterdam: Elsevier, 2006.

[17] I. Westermann, O. S. Hopperstad, K. Marthinsen, and B. Holmedal, "Ageing and work-hardening behaviour of a commercial AA7108 aluminium alloy," *Materials Science and Engineering: A,* vol. 524, pp. 151-157, 2009.

[18] G. Gottstein, *Physical foundations of materials science*. Berlin: Springer, 2004.

[19] A. Munitz, C. Cotler, and M. Talianker, "Aging impact on mechanical properties and microstructure of Al-6063," *Journal of Materials Science,* vol. 35, pp. 2529-2538, 2000/05/01 2000.
[20] G. A. Edwards, K. Stiller, G. L. Dunlop, and M. J. Couper, "The precipitation sequence in Al–Mg–Si alloys," *Acta Materialia,* vol. 46, pp. 3893-3904, 1998.
[21] X. Fang, M. Song, K. Li, and Y. Du, "Precipitation Sequence of an Aged Al-Mg-Si Alloy," *Journal of Mining and Metallurgy,* 2010.
[22] O. R. Myhr, Ø. Grong, and K. O. Pedersen, "A Combined Precipitation, Yield strength, and Work Hardening Model for Al-Mg-Si Alloys," *Metallurgical and Materials Transactions A,* vol. 41A, pp. 2276-2287, 2010.
[23] F. J. Humphreys and M. Hatherly, *Recrystallization and related annealing phenomena*. Oxford: Pergamon, 1995.
[24] B. Verlinden, J. Driver, I. Samajdar, and R. D. Doherty, "Chapter 8 Textural developments during thermo-mechanical processing," in *Pergamon Materials Series*. vol. Volume 11, ed: Pergamon, 2007, pp. 151-183.
[25] G. Gottstein, M. Buescher, and J. Hirsch. (2001-2010). *Representing Texture*. Available: http://aluminium.matter.org.uk
[26] O. Engler and V. Randle, *Introduction to texture analysis: macrotexture, microtexture, and orientation mapping*. Boca Raton: CRC Press, 2010.
[27] M. Kuroda and V. Tvergaard, "Effects of texture on shear band formation in plane strain tension/compression and bending," *International Journal of Plasticity,* vol. 23, pp. 244-272, 2007.
[28] K. B. S. Couto, S. R. Claves, W. H. Van Geertruyden, W. Z. Misiolek, and M. Goncalves, "Effects of homogenisation treatment on microstructure and hot ductility of aluminium alloy 6063," *Materials Science and Technology,* vol. 21, pp. 263-268, 2005.
[29] D. Lassance, D. Fabrègue, F. Delannay, and T. Pardoen, "Micromechanics of room and high temperature fracture in 6xxx Al alloys," *Progress in Materials Science,* vol. 52, pp. 62-129, 2007.
[30] W. F. Hosford and R. M. Caddell, *Metal forming : mechanics and metallurgy*. Upper Saddle River, N.J.: PTR Prentice Hall, 1993.
[31] T. L. Anderson, *Fracture mechanics : fundamentals and applications*. Boca Raton, Fla.: Taylor & Francis, 2005.
[32] C. S. Barrett, *Structure of metals : crystallographic methods, principles and data*. New York: McGraw-Hill, 1943.
[33] T. Bergstad, O. S. Hopperstad, and M. Langseth, "Elasto-Viscoplastic Constitutive Models in the Explicit Finite Element Code LS-DYNA3D," presented at the Second International LS-DYNA3D Conference, San Francisco, 1994.
[34] Y. Leng, *Materials Characterization: Introduction to Microscopic and Spectroscopic Methods*. Hong Kong University of Science and Technology, 2008.
[35] J. Hjelen, "Field Emission SEM," presented at the Lecture on TMT4300 Light and Electron Microscopy, NTNU, 2013.
[36] J. Hjelen, *Scanning elektron-mikroskopi*. Metallurgisk institutt, NTH, 1989.
[37] UniversityOfGlasgow. *Scanning Electron Microscopy (SEM)*. Available: http://www.gla.ac.uk/schools/ges/research/researchfacilities/isaac/services/scanningelectronmicroscopy/

Appendix: Work-Hardening Parameters

Table A1: Work-hardening parameters used in the curve fitting with the generalized Voce equation with three terms.

Material	σ_0 (MPa)	Q_1 (MPa)	C_1	Q_2 (MPa)	C_2	Q_3 (MPa)	C_3
As cast (1U-1)	107.70	276.90	0.44	96.05	15.71	400	1.00
As cast (1U-2)	73.37	81.24	8.18	65.29	46.50	400	0.20
As cast (1U-3)	97.26	66.40	11.36	47.23	23.15	400	0.25
Extruded (2U-1)	97.04	33.34	14.48	52.65	29.16	400	0.33
Extruded (2U-2)	60.91	72.67	15.79	51.10	87.12	400	0.31
Extruded (2U-3)	75.32	50.89	12.02	60.36	46.13	400	0.30
Extr./cold r./recr. (3U-1)	117.87	50.75	10.91	42.15	22.10	400	0.27
Extr./cold r./recr. (3U-2)	91.90	3.90	9.99	106.36	13.68	400	0.31
Extr./cold r./recr. (3U-3)	113.35	56.67	10.28	43.03	22.60	400	0.27

Material	σ_0 (MPa)	Q_1 (MPa)	C_1	Q_2 (MPa)	C_2	Q_3 (MPa)	C_3
As cast (1P-1)	159.98	15.67	18.94	66.51	37.47	400	0.22
As cast (1P-2)	180.45	0	15.21	59.15	32.74	400	0.22
Extruded (2P-1)	177.00	0	13.60	53.84	30.13	400	0.28
Extruded (2P-2)	170.71	0	15.30	58.73	32.97	400	0.30
Extruded (2P-3)	171.40	0	15.65	60.41	33.92	400	0.29
Extr./cold r./recr. (3P-1)	162.56	16.53	19.09	67.19	40.90	400	0.24
Extr./cold r./recr. (3P-2)	179.56	0	15.16	58.27	31.80	400	0.27
Extr./cold r./recr. (3P-3)	180.55	0	16.32	64.60	31.32	400	0.24

Material	σ_0 (MPa)	Q_1 (MPa)	C_1	Q_2 (MPa)	C_2	Q_3 (MPa)	C_3
As cast (1O-1)	186.85	0	9.49	30.38	21.69	400	0.17
As cast (1O-2)	185.95	0	11.02	41.15	63.27	400	0.12
As cast (1O-3)	188.60	0	10.74	41.00	74.01	400	0.13
Extruded (2O-1)	162.46	4.71	20.82	59.54	19.44	400	0.10
Extruded (2O-2)	182.51	0	10.21	39.92	24.80	400	0.12
Extruded (2O-3)	179.84	0	10.28	37.30	67.86	400	0.15
Extr./cold r./recr. (3O-1)	190.48	0	9.25	23.51	105.25	400	0.14
Extr./cold r./recr. (3O-2)	147.34	0	16.62	63.93	90.56	400	0.12
Extr./cold r./recr. (3O-3)	184.38	258.52	0.21	32.54	81.83	400	1.00